©Copyright 2025

Yannan Liu

Antenna Systems for Emerging Applications

Yannan Liu

A dissertation
submitted in partial fulfillment of the
requirements for the degree of

Doctor of Philosophy

University of Washington

2025

Reading Committee:

Hossein Naghavi, Chair

Akshay Gadre

Lih Y. Lin

Zachary Sherman

Program Authorized to Offer Degree:
Electrical and Computer Engineering

University of Washington

Abstract

Antenna Systems for Emerging Applications

Yannan Liu

Chair of the Supervisory Committee:
Hossein Naghavi
Electrical and Computer Engineering

Antenna systems are fundamental to many modern technologies, enabling reliable communication and sensing in challenging environments. This thesis focuses on two emerging applications that require specialized antenna designs: deep-sea communications and terahertz (THz) science for sensing, communication, and spectroscopy. With increasing interest in climate research, understanding ocean dynamics has become critically important. To support this, we propose various antenna designs suitable for deep-sea and through-sea-ice communication scenarios. Furthermore, the demand for ultra-fast communication beyond 5G drives exploration into the THz frequency band. However, antenna systems operating at these high frequencies are still under development and less mature compared to millimeter-wave (mm-wave) and microwave technologies. As part of this work, we also develop a comprehensive database of dielectric material properties essential for designing dielectric antennas—promising candidates for low-cost THz antennas.

Deep-Sea Communication and AUV Docking Challenges: One significant challenge in ocean exploration is establishing reliable data transfer between autonomous underwater vehicles (AUVs) and docking stations. Although AUVs offer autonomous and flexible underwater operation, low docking success rates—stemming from alignment sensitivity and limited communication range—pose persistent barriers. To address this, we introduce two dedicated antenna systems:

- An Out-of-Line Series Feed Slot (OLSFS) antenna operating at 2.4 GHz, designed for omnidirectional, centimeter-range wireless data transfer. Its design reduces angular alignment constraints during docking procedures.

- A loaded waveguide antenna functioning in the lower UHF band, enabling decimeter-range communication. This antenna offers broad operational bandwidth, a wide radiation pattern, and circular polarization, resulting in a robust link that is less sensitive to misalignment.

Both antenna systems have been extensively validated through simulations and experimental testing, demonstrating strong agreement and reliable performance in underwater conditions.

Through-Sea-Ice Communication for Polar Exploration: In addition to AUV docking, this thesis presents a novel antenna solution for through-sea-ice communications, addressing vital needs in polar regions. Floating sea ice obstructs direct communication paths, hindering ocean exploration. To overcome this, we develop an integrated RF system comprising a loaded waveguide antenna, a matching layer, and a guiding tube. This configuration facilitates stable communication links between AUVs and satellites through sea ice—an essential capability for polar research and long-range underwater operations.

Advancing Terahertz (THz) Technology: Finally, this thesis explores the promising field of THz systems, motivated by their potential applications in next-generation 6G wireless communications, spectroscopy, and sensing. Due to their sub-millimeter wavelengths, THz signals exhibit unique electromagnetic behaviors distinct from mm-wave and infrared (IR) frequencies. Precise knowledge of materials' dielectric properties at these frequencies—above 100 GHz—is critical for effective antenna design. However, material characteristics at THz are often different from those at lower frequencies, necessitating a dedicated database. To this end, we perform comprehensive material characterization using a standard transmission-based method, employing a vector network analyzer. Additionally, we propose a novel, cost-effective approach using a compact frequency-modulated continuous-wave (FMCW) radar-on-chip platform, making high-frequency material testing more accessible. The resulting database provides a vital resource for developing and optimizing THz antennas.

Collectively, these studies demonstrate how tailored antenna system designs can overcome physical challenges, enhance operational performance, and unlock new capabilities in underwater communication and high-frequency applications. They pave the way for advancements across multiple frontier applications in ocean exploration and beyond.

TABLE OF CONTENTS

LIST OF FIGURES

ACKNOWLEDGMENTS

I would like to express my sincere appreciation to the University of Washington and the Electrical and Computer Engineering Department for providing me the opportunity to pursue my Ph.D. I am especially grateful to Dr. Hossein Naghavi for his unwavering support and clear guidance during the final two years of my Ph.D. program, which has been vital to my overall growth and success in achieving this degree. Dr. Naghavi and I worked closely on all of my publications during that time. I am thankful not only for his assistance with research but also for his patient instruction on how to write effective scientific papers. Furthermore, I appreciate his mentorship in guiding me to become a better teacher and offering wise advice regarding my career choices and life path. Without his guidance, I would not be where I am today. I would also like to extend my thanks to Dr. Yasuo Kuga, who initially introduced me to the Ph.D. program. He taught me the fundamental principles of electromagnetics and encouraged me to apply to become his Ph.D. student during my senior year of undergraduate studies. Dr. Kuga has always been patient when discussing research and explaining complex concepts. He allowed me the freedom to explore my interests and develop my skills. After his retirement, he kindly helped me find Dr. Hossein Naghavi as my co-advisor and offered invaluable suggestions and access to experimental equipment. I am grateful to Dr. Lih Lin for her instruction during my final undergraduate year and for serving on my committee for the qualifying, general, and final exams of my Ph.D. program. She consistently provided important insights and useful guidance. I would also like to thank my current and previous supervisory committee members: Dr. Akshay Gadre, Dr. Zachary Sherman, Dr. Arka Majumdar, and Dr. Eli Shlizerman, for their time and support. Additionally, I want to thank John Mower for his assistance with my underwater antenna projects, as well as my ECE graduate advisor, Jennifer Huberman, for her guidance throughout my Ph.D. journey. I want to express my gratitude to my colleagues, including Chuyang Peng, Denil Sabu, Shanti Garman, Shruti Chakraborty, Xiangyu Zhao, Zi Zhang, and Zhuoran Wu, for their assistance in my research.

I am deeply appreciative of my grandparents, parents, aunts, uncles, cousins, sisters, and all other family members for their unwavering support and encouragement throughout my Ph.D. program. I would like to thank my best friends—Peng Xiang, Qinlin Lei, Yiwei Li, Sian Jin, and Wenjie Yang—for their unchangeable support throughout my Ph.D. studies and their genuine help in my personal growth. A special thanks goes to my roommates during my studies in University of Washington: Jiang Huang, Qixuan Huang, Shihcheng Tsai, and Yina Wei. We had a very good time together as roomates and became very good friends afterwards, and they continuously give me valuable suggestions and help. I also want to give a special thanks to a couple: Huabin Wu, and Qiuyue Sun, who are my landlord in the last stage of my Ph.D. study. They created a comfortable living environment, helped with my daily life and gave me valueable suggestions and support. I also want to acknowledge all of my other friends and people who are not mentioned here for certain reasons; their contributions are equally important to my achievement of this degree and my life in University of Washington.

DEDICATION

To my family

Chapter 1

INTRODUCTION

1.1 *Background*

Antennas have long been a critical component in communication systems, enabling the transfer of information across vast and complex environments. As technological exploration reaches increasingly challenging domains — such as the deep oceans, polar regions, and terahertz (THz) frequency bands — antenna design must evolve to meet the rigorous demands of these emerging applications. This thesis explores novel antenna systems specifically designed for three such frontiers: deep-sea autonomous underwater vehicle (AUV) docking, satellite communication through polar sea ice, and high-frequency antenna design enabled by advanced THz dielectric characterization.

Oceans play critical roles in the Earth and human society. Three-quarters of the Earth's surface is covered by seas and oceans. They generously provide foods [2], fossil fuels [3, 4] and renewable energies [5, 6] to human civilization. Meanwhile, they also play a critical role in climate regulation such as adjusting the levels of greenhouse gases in the atmosphere and global temperatures through absorbing solar radiation, providing water vapor, exchanging radiatively important gases and so forth [7–9]. Furthermore, ocean and sea play a significant role in the human health residing in coastal areas [10] where over 40% of the global population and most of the world's megacities are located [11, 12], and more are migrating to [13, 14]. The study of sea has evolved over a period of 2,500 years since the curiosity of Greek philosophers and the development of measurement equipment allow people to explore in deeper sea environment [3].

With the help of technological advancement, people started to explore deeper oceans in the middle of the nineteenth century, but oceans are still largely unexplored due to their distinct underwater environment [3, 4, 15]. The first application of underwater communication happened in 1945 when an underwater telephone was developed to communicate with submerged submarines [16] and still the underwater networking is a rather unexplored area [17].

Over the years, people developed various methods to explore the oceans. In 1994, the Tropical

Atmosphere Ocean (TAO)/Triton mooring array was placed in the Pacific Ocean to collect climate data and successfully forecasted El Nino phenomena one year ahead of their peak [18]. In 1999, the Argo floats, a global ocean observation array, were first deployed to collect temperature, salinity, and biogeochemical data from 0 to 2,000 m below the sea surface [19]. Also, in the 1990s, the Global Ocean Observing System (GOOS) was developed to monitor ocean data through cooperation among countries [20].

Autonomous Underwater Vehicles (AUVs) have been developed to enhance underwater exploration and data collection capabilities [21]. Docking stations have also been designed to enable AUVs to exchange data, receive new instructions, and recharge their batteries while underwater. These stations represent one of the most practical solutions for extending the operational time of AUVs [21, 22]. Moreover, docking stations allow AUVs to undertake challenging tasks, such as operations under sea ice [23], which can greatly enhance the efficiency of various projects. Therefore, AUV with docking technology is significant for ocean exploration [24, 25].

For example, the Ocean Observatories Project of the Applied Physics Laboratory (APL) and the Oceanography Department at the University of Washington (UW) established a fast Wi-Fi link on the sea floor more than 2000 meters below the sea surface. As shown in Fig. 1.1, they developed an AUV called Deep Profiler (DP) [26] that collects information from 200-meter to 2,900-meter depth in sea [27] and transmits the collected data to the docking station at the ocean bottom.

Despite numerous efforts to develop Autonomous Underwater Vehicles (AUVs) equipped with docking capabilities, this technology has made little significant progress. An earlier article reported that researchers have developed eight types of docking systems; however, none are designed for prolonged operations, and the maximum success rate for docking is only 85% [21]. Even more recently, docking remains a challenging problem, and the number of successful solutions has been disappointing [28, 29].

Therefore, this thesis first proposes that innovative antenna designs can be utilized to give more freedom to the AUV docking process for future design, which helps solve the docking challenges. One of the main obstacles to underwater communication is the choice of physical layer in the communication network. It is difficult to utilize optical waves due to their characteristics, such as backscatter, absorption, and poor visibility [17]. Acoustic waves are often used in underwater communication due to their low attenuation in the water, and the reliable operation of acoustic

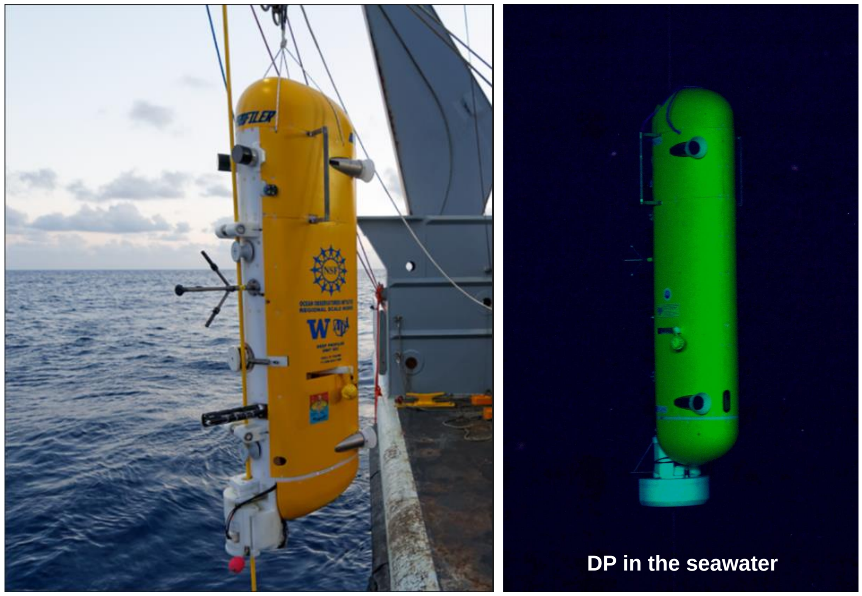

Figure 1.1: Pictures of UW Deep Profiler [1].

waves allows them to be utilized in various underwater applications. For example, in environment monitoring, acoustic waves applied in an underwater network are used to monitor aquatic biological communities and waste-stream effluents [30]; in 1974, an underwater acoustic navigation system was developed and in use at the Woods Hole Oceanographic Institution [31], and also used in underwater robotic vehicles [32]. While acoustic waves are also facing some major challenges in the underwater networks, such as limited available bandwidth, high bit error rates, temporary losses of connectivity (shadow zones), and propagational delay [30]. Recently, underwater communication through electromagnetic waves in the range of MHz to GHz is gaining popularity, and it has several advantages over acoustic waves despite its high attenuation. For example, electromagnetic waves have rapid transfer of signals and can be used for real-time interaction applications; electromagnetic waves are not adversely affected by the air-water boundary; amplitudes of electromagnetic waves are normally as high as a hundred volt range, compared with the amplitudes of acoustic waves, which can be higher than kV [33]. In the meantime, there has already been a renewed interest in underwater antenna design due to the availability of low-cost communication devices and artificial dielectric materials [34–36], which could be beneficial to the development of antennas for AUV docking system. Some examples are followed. A prototype of a magnetoelectric (ME) antenna pair was presented for an underwater communication system [37]. A single loop, multi-turn loop, dipole, and folded dipole were investigated in the seawater environment [35, 38]; A Bow tie antenna has been designed for Wi-Fi Underwater Communications [39].

This thesis details the design, simulation, fabrication, and testing of two antenna systems for data transmission. We first propose an out-of-line series feed slot (OLSFS) antenna operating at 2.4 GHz, which is a horizontal array of out-of-line slot antennas conformed to a cylinderical platform. It offers a distinct advantage for angle alignment during docking, having been successfully deployed in an underwater vehicle project. The second antenna is designed to provide an extended range for data transmission during docking, potentially easing the strict requirements for precision. Additionally, a high dielectric constant material is used to maintain a compact antenna size since small size and light weight are among the most important features of AUVs [40].

Polar oceans play a crucial role in the world. In addition to the marine resources, they influence global climate and affect the stability of ice sheets, which directly impact global temperature and sea level. However, a significant gap exists in the ocean observing system in the polar regions compared with other places in the world and the insufficient ocean observing system in the polar region can affect the quality of various important applications such as weather forecasting, seasonal predictions, aquaculture and environmental management [41]. The presence of sea ice is the key challenge for ocean observation in polar regions since it complicates the communication between the ocean and atmosphere/space [42]. For example, Argo profiling floats that constitute the first global array for observing the subsurface ocean cannot surface and transmit data to satellites when there is floating sea ice, which prevents them from providing real-time data [43]. Currently, in the communication link composed of seawater, sea ice, and air, the most popular approach is based on acoustic waves [44]. The magnetic field has also been utilized in some projects to achieve connection through sea ice floating on water [45]. Additionally, optical wireless communication systems and optical fiber tethers have been employed for similar sea ice communication scenarios [46].

This thesis also presents an RF/microwave antenna system designed to establish communication links beneath sea ice. Sea ice is highly dissipative at microwave frequencies, but electromagnetic (EM) signal penetration is adequate at frequencies below 500 MHz. While antenna size is typically proportional to wavelength, we can reduce the size of our antennas by utilizing materials with a high

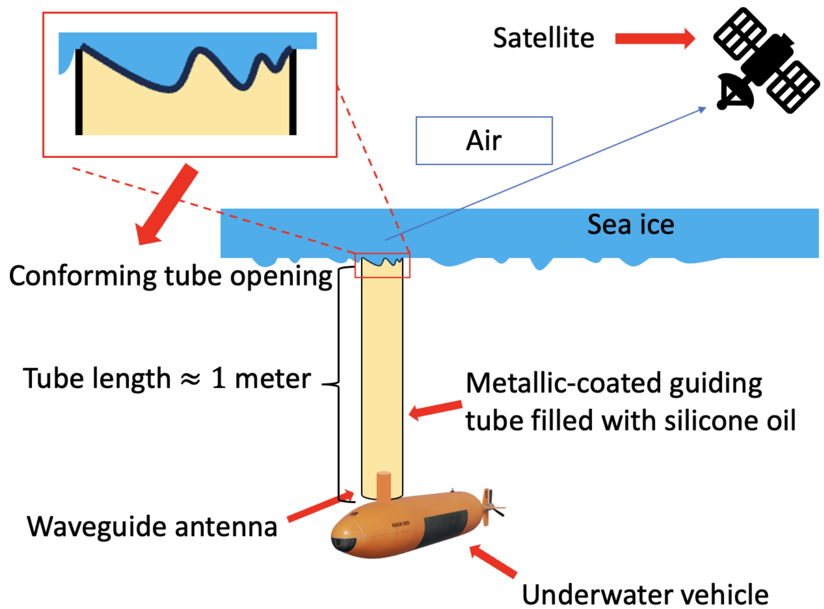

Figure 1.2: Satellite communication link through sea ice

dielectric constant [47]. Our proposed antennas utilize a circular waveguide filled with these high dielectric constant materials. Additionally, we have designed an impedance-matching layer and a flexible metallic-coated guiding structure filled with silicone oil to transmit EM signals through the sea ice efficiently. Figure 1.2 shows an example of deploying the proposed antenna system. It is important to note that the guiding tube features an opening designed to fit the irregular surface of the sea ice bottom. Additionally, the tube can be one meter long or longer, ensuring that AUVs do not collide with the sea ice. Our antenna systems offer several advantages: they transmit circularly polarized waves, are compact thanks to a high dielectric core, provide wide bandwidth, have a directional radiation pattern, withstand high pressure, and can be tailored for various frequencies.

Lastly, this thesis presents the measurement of material properties at THz frequencies, and focuses on building a database of material properties at THz frequencies. The database will be used to design innovative antennas at such high frequencies.

In recent years, THz and mm-wave systems [48–50] have attracted many researchers because of numerous promising applications that they provide. Various theoretical and experimental attempts have been made to establish THz-frequency sensing as a new characterizing tool for security screening [51], industrial quality control [52–57], high-speed communications [58, 59], high-resolution radars [60–64], and biological spectrometry applications [65]. With the growing demand for faster wireless data exchange, THz frequencies are essential for 6G communications, enabling terabit-per-second data rates and supporting techniques like massive Multiple-Input Multiple-Output (MIMO) to overcome high path losses [66–69]. They also provide short-range, high-throughput connectivity for urban and indoor environments [70, 71]. Additionally, THz imaging is used in the pharmaceutical industry to assess tablet coatings and integrity, offering non-destructive measurement methods [72, 73]. In the cosmetic and medical fields, THz imaging is employed for non-invasive skin analysis, including hydration assessment and the early detection of basal cell carcinoma (BCC) with high precision [72, 74]. THz imaging also provides advantages for general cancer detection by detecting tissue properties associated with cancer, such as increased water content [75, 76]. In oral health, THz frequencies are used to detect early-stage tooth decay, which is difficult to identify with traditional methods like X-rays [72, 77]. Furthermore, THz frequencies are increasingly utilized in security screening, offering advantages such as high-resolution 3D imaging and non-ionizing radiation for safe and detailed analysis [78, 79]. Due to the short wavelength of THz band at the order of micrometer, it has unique features that distinguish it from its neighbor bands, mm-Wave and Infra-Red (IR). In this project, we have targeted two of these unique features of the THz band for spectroscopy, which have apparent industrial future.

Antenna design for THz frequencies is an emerging field, with significant applications in 6G communication networks [80] and high-resolution imaging radar systems [81–85]. A promising approach for designing complex, cost-effective antennas involves the use of 3D printing technologies. To design antennas using 3D printing materials such as PLA [86], ABS [87], and resin [88], it is essential to characterize their properties at THz frequencies. However, there is a lack of comprehensive data in the literature regarding the permittivity and loss tangent of these materials. The objective of this research is to establish a database for 3D printing materials in the THz band, which will support the development of emerging applications.

In order to successfully establish the database, we need to extract the material properties from both the traditional approach, making use of a vector network analyzer with an extender, and the innovative approach relying on a compact radar chip. Obtaining material properties from a vector network analyzer has long been studied and examined. Traditional methods for extracting material properties, particularly the dielectric constant, rely on Vector Network Analyzers (VNA) and lenses that focus electromagnetic beams on samples. These methods mainly fall into two categories: Resonant and Transmission/Reflection (T/R) methods. The T/R methods have evolved over time with various algorithms developed to characterize material properties in different scenarios, offering wideband characterization compared to resonant methods [89, 90]. The Nicholson–Ross–Weir (NRW) method is a classic approach for extracting dielectric constants using measured scattering parameters, but it faces limitations with low-loss materials at certain frequencies, such as half-wavelength resonances [91–93]. Several enhanced T/R methods have been developed, such as iterative procedures and nonlinear least-squares regression techniques, which improve accuracy and stability for low-loss materials and high-permittivity samples [93–95]. Tailored approaches, such as those for measuring the impedance of thin films [96] and high-dielectric materials at THz frequencies [97], have been introduced for specific scenarios. Free-space techniques are gaining popularity for their non-destructive, contactless nature, avoiding higher-order mode excitation and the need for precise sample machining. These techniques allow flexible setups and minimize boundary effects, making them suitable for various testing conditions [90].

In our traditional approach, we used a vector network analyzer to develop a compact and accurate algorithm for extracting material properties based on the measured transmission coefficients of samples with varying thicknesses. The values obtained from this method provided a solid foundation for our database. Following this, we conducted experiments using an innovative method with a THz FMCW radar chip. This new method of material characterization using radar chips serves as an economical and convenient alternative to the traditional method, which is often bulky and expensive.

1.2 *Summary of Research Contributions*

This thesis presents the development of advanced antenna systems tailored to address the unique challenges of three emerging and complex environments: deep-sea docking of autonomous underwater vehicles (AUVs), communication through polar sea ice, and THz material characterization. These advancements aim to bridge critical gaps in communication and data transmission across extreme conditions, supporting new technological capabilities in these specialized fields.

In the first part, we introduce two groundbreaking antenna systems designed to enhance the reliability and efficiency of docking procedures for AUVs in deep-sea environments. The first system utilizes an out-of-line series feed slot (OLSFS) antenna operating at 2.4 GHz. This antenna provides omnidirectional data transfer over centimeter-scale ranges, effectively alleviating the need for precise angular alignment during docking. Such an improvement is critical for operational efficiency in deep-sea environments, where alignment precision can often be a limiting factor. The second antenna system involves a loaded waveguide antenna that operates in the lower side of the ultra-high frequency (UHF) band. This system offers decimeter-range communication, ensuring reliable data transfer even in the most challenging underwater conditions, where conventional communication methods often fail due to signal attenuation. Comprehensive simulation and experimental results are presented to demonstrate the effectiveness of both antenna designs in underwater communication scenarios. This work marks a significant step forward in the advancement of underwater robotics and ocean exploration, addressing key challenges related to AUV docking and communication, and facilitating more reliable and efficient operations in these demanding environments.

The second part of the thesis focuses on solving the critical communication gap in polar regions by developing a novel RF-based through-ice communication system. Traditional satellite communication systems, such as those used by AUVs, are severely hindered by sea ice, which prevents surfacing devices like Argo floats from maintaining reliable communication with surface stations. To overcome this significant challenge, a multi-stage antenna system has been designed. This system incorporates a Titanium dioxide TiO2 (ϵr, eff = 96) loaded waveguide antenna, a barium tetra-titanate BaO9Ti4 (ϵr, eff = 37) quarter-wave matching layer, and a flexible guiding tube filled with silicone oil (ϵr, eff = 37). The antenna generates circularly polarized waves by employing perpendicular coaxial feeds with a 90° phase difference, which greatly enhances the system's robustness against alignment errors. Additionally, the guiding tube extends from the AUV to the underside of the ice, ensuring efficient electromagnetic wave transmission through up to one meter of sea ice. Full-wave simulations using Ansys HFSS reveal low reflection losses ($\leq$ 0.28 dB), manageable propagation attenuation ($\sim$ 5.6 dB), and an overall signal loss of approximately 10.2 dB, thus validating the feasibility of high-fidelity RF communication through sea ice. This innovative system presents a compact, pressure-resistant, and frequency-flexible solution that enables real-time satellite communication for polar ocean observation missions, opening up new possibilities for scientific research in remote and extreme environments.

The third component of this thesis introduces a pioneering innovation in the field of THz material characterization: the first fully integrated THz frequency-modulated continuous-wave (FMCW) Fourier-transform spectrometer (FMCW-FTS) for wideband dielectric material characterization. Traditional THz spectrometers are typically large, expensive, and come with significant mechanical requirements that limit their practical resolution. This thesis presents a solution by embedding all components into a single FMCW radar chip, which records a two-dimensional intermediate frequency (IF) signal matrix across reflector positions with micrometer-scale precision. This integration significantly reduces the signal path requirement for 10 kHz resolution, from tens of kilometers in traditional systems to just a few centimeters. The system generates a spectrogram through Fourier transform of the IF data, enabling precise extraction of the complex permittivity of solid samples based on both amplitude and phase changes. Notably, this spectrometer is compact, low-cost, and suitable for clinical and on-site applications, such as volatile organic compound (VOC) gas detection for disease diagnosis. Initial measurements demonstrate the system's capability for high-resolution spectral analysis at THz frequencies, providing a promising tool for a variety of applications.

Furthermore, this work contributes significantly to the establishment of a comprehensive database for 3D printing materials at THz frequencies. Such a database will play a crucial role in supporting the development of next-generation technologies in several key areas, including 6G communications, ultra-sensitive gas sensing, and sub-THz antenna design. The establishment of this database can drive the development of novel materials and technologies, offering invaluable resources for researchers and engineers working on advanced materials characterization. With this database, future advancements in THz systems and their applications will be more accessible, further enhancing the potential of THz technologies in emerging applications such as communication, medical diagnostics, and environmental monitoring.

In summary, this thesis addresses some of the most pressing challenges in extreme environmental communication, material characterization, and emerging technologies. The developed antenna systems for AUV docking and polar communication, alongside the miniaturized, cost-effective THz spectrometer, represent significant contributions to the fields of underwater robotics, RF communication, and materials science. The establishment of a comprehensive THz material database further complements these efforts, ensuring that the capabilities of these innovative systems will continue to evolve and expand, paving the way for new applications and advancements in the coming years.

1.3 *Thesis Outline*

The remainder of this thesis is organized as follows. In Chapter 2, we present the implementation of two underwater antenna systems designed to enhance the docking process of autonomous underwater vehicles. These antenna systems support communication in the centimeter and decimeter ranges, respectively. We provide both simulation and experimental results to demonstrate the validity of the design. Chapter 3 focuses on the design and simulation of an antenna system that includes a loaded waveguide antenna, a matching layer, and a guided tube. This system aims to establish a communication link in a traditionally challenging scenario involving floating sea ice in polar regions. In Chapter 4, we explore THz frequency material characterization using two methods: a conventional approach utilizing a Vector Network Analyzer and an innovative approach that employs an FMCW radar. This thesis includes the material in the author's previous papers published on IEEE [26, 98], one paper accepted by IEEE [99], one paper under review by IEEE [100], and one paper to be submitted to IEEE [101].

Chapter 2

ANTENNA SYSTEMS FOR RELIABLE DOCKING OF AUTONOMOUS UNDERWATER VEHICLES

2.1 *Motivation*

The world's oceans cover over 70% of the Earth's surface and remain one of the least explored frontiers in science and engineering. Autonomous underwater vehicles (AUVs) offer the promise of sustained, long-range exploration and monitoring, but their effectiveness is limited by the need to dock with subsea stations for data offload, battery recharge, and mission updates. Reliable docking under extreme underwater conditions—high pressure, low temperatures, strong currents, and turbid water—is a formidable challenge. Most existing AUV docking systems report success rates below 90%, often hindered by the complexity of precise alignment, mechanical tolerances, and the unreliability of traditional underwater communication links.

Acoustic communication, the conventional choice for subsea data transfer, suffers from limited bandwidth, multipath reflections, and high latency. Optical methods can achieve very high data rates but require near-perfect line of sight and are quickly degraded by particulate matter in the water column. Radio-frequency (RF) links in the hundreds of megahertz to low-gigahertz range present an attractive alternative, combining moderate penetration, real-time performance, and high throughput. However, seawater exhibits significant dielectric loss at these frequencies, imposing severe attenuation that limits usable range and makes the data link highly sensitive to antenna design and alignment.

Standard dipole or patch antennas adapted from terrestrial systems typically demand vehicle-to-station clearances of only a few centimeters and strict angular tolerances—conditions that are difficult or impossible to maintain in dynamic docking scenarios. A slight pitch or roll of the AUV can shift the antenna alignment out of its narrow beam, breaking the link and compromising the docking procedure. Consequently, there is a critical need for antenna solutions that can maintain high data-rate RF connectivity over larger positional and angular tolerances, while also withstanding the harsh underwater environment.

This chapter develops two complementary antenna architectures aimed at overcoming these bottlenecks:

1. **An out-of-line series feed slot (OLSFS) antenna operating at 2.4 GHz.** A linear array of feed-coupled slots is patterned on a flexible PCB that conforms to the curved hull surfaces of both the AUV and docking station. The slot geometry produces a wide elevation fan beam and nearly omnidirectional azimuthal coverage, enabling reliable communication over a full 360° docking approach arc without requiring fine angular alignment. The conformal nature of the array preserves its electromagnetic performance even under bending and under deep-sea pressure, and the planar feed network simplifies fabrication and integration.

2. **High-dielectric loaded waveguide antenna in the UHF band.** To further extend link margin and relax positional constraints, a compact circular waveguide is filled with a high-permittivity dielectric. This reduces the overall size while supporting circular polarization for improved misalignment tolerance in both azimuth and elevation. Operating at a lower frequency than the slot array reduces seawater attenuation, permitting reliable decimeter-scale separations. The waveguide structure is inherently robust against pressure and water intrusion, ensuring repeatable performance in deep dives.

By combining a broad-beam, conformal slot array with a compact, dielectric-loaded waveguide, these designs target the two key failure modes of subsea docking links: narrow beamwidth (angular sensitivity) and limited link budget (attenuation losses). The conformal array guarantees stable RF connectivity throughout the AUV's docking approach, while the waveguide antenna extends the usable range and further relaxes alignment requirements. Together, they promise to raise docking success rates, reduce vehicle risk, and enable truly autonomous long-duration missions in demanding underwater environments.

This motivation sets the stage for the detailed design, simulation, and experimental validation presented in the remainder of this chapter.

2.2 *Introduction*

Approximately three-quarters of the Earth's surface is enveloped by seas and oceans, which are among the most vital resources and diverse ecosystems on the planet. These vast bodies of water generously provide various essential resources, including food sources, fossil fuels, such as minerals, oil, and natural gases, as well as renewable energy options that are increasingly important for sustainable development. According to recent studies, the oceans contribute significantly to human civilization by serving as a crucial reservoir for these resources [2–4]. The oceans also play a fundamental role in regulating the global climate. They help moderate temperatures and influence weather patterns by absorbing solar radiation, releasing water vapor, and exchanging other radiatively significant gases in the atmosphere. This ability to regulate climate is vital for maintaining a balanced ecosystem, and this interaction affects everything from local weather conditions to broader climate trends [7–9]. Moreover, oceans and seas are indispensable for human health, particularly for the populations residing in coastal areas. It is estimated that over 40% of the global population lives within 100 kilometers of coastlines, where many of the world's megacities are situated [10–12]. These coastal regions often provide not only economic opportunities through fisheries and tourism but also connect communities to vital resources for their sustenance and well-being. However, with the increasing migration of people towards these areas, pressures on these marine environments are intensifying, leading to challenges such as resource depletion and habitat destruction [13, 14]. Unfortunately, despite significant technological advancements enabling exploration, the vast majority of oceanic environments remain largely uncharted and poorly understood. Since the mid-19th century, when deeper ocean explorations began in earnest, scientists have made strides in uncovering some of the mysteries of the deep sea. However, the unique and challenging underwater environments, coupled with the sheer vastness of the oceans, present formidable obstacles to thorough exploration [3, 4, 15]. Therefore, enhancing our understanding of the oceans is not only beneficial but essential for the sustainable development of human society. As we face pressing global challenges such as climate change [102, 103], resource scarcity [104], and biodiversity loss [105, 106], a comprehensive approach to studying and protecting ocean ecosystems becomes increasingly critical. This understanding will, in turn, inform policies and practices that safeguard marine environments while harnessing their potential for the benefit of human health, economic prosperity, and the overall well-being of our planet. Through coordinated global efforts, we can work towards a future where the oceans continue to thrive and serve as a cornerstone for life on Earth.

Ocean observation systems are key projects developed through the cooperation of nations to monitor changes in physical, chemical, biological and geologic features of oceans [107]. In 1994, the Tropical Atmosphere Ocean (TAO)/Triton mooring array was placed in the Pacific Ocean to collect climate data and successfully forecasted El Nino phenomena one year ahead of their peak [18]. In 1999, the Argo floats, a global ocean observation array, were first deployed to collect temperature, salinity, and biogeochemical data from 0 to 2,000 m below the sea surface [19]. Also, in the 1990s, the Global Ocean Observing System (GOOS) was developed to monitor ocean data through cooperation among countries [20]. All of the above ocean observation systems show humans' strong desire to explore the largely untouched water body continuously.

There are various methods for ocean observation. Moored buoys have been utilized for decades and are a mature technology for collecting ocean data. The Tropical Ocean Global Atmosphere (TOGA) program that aims at observing the tropical Pacific Ocean benefits from this method [107]. Drifter, also called drifting buoys, is another technology used to monitor the ocean for a long time [107]. It has been deployed in the U.S. Costal Dynamics Experiment (CODE), which is a multi-institutional examination of coastal circulation [108]. Space-borne sensors are another essential tool to gain sea surface geophysical parameters such as sea surface temperature, wave height, salinity, and so forth [107]. Unmanned surface vehicles that may date back to World War II play an important role in oil spilling detection, bathymetric mapping, offshore pipeline survey, meteorological survey, and water ecological study [109–111]. Argo Floats is an international program to sample temperature, salinity, and current data of the oceans [112]. They can descend to a depth of as much as 2,000 meters and exchange data with satellites during their surfacing. The underwater glider is an autonomous float that can descend by shifting its buoyancy and battery mass and adjusting its wings. It can replace expensive moored buoys at designated sites for ocean observation [113, 114]. Cabled seafloor observatories provide significant electrical power and bandwidth to the monitoring instruments at the seafloor, and they are often operating at annual scales and are highly reliable [107]. Compared with underwater gliders and moored buoys, autonomous underwater vehicles (AUVs) have more maneuverability and are able to carry out more diverse missions, such as geological exploration [115] and oil spill detection [116]. The development of hadal landers helps monitor the deepest marine environment on Earth, with depths ranging from 6000 m to 11000 m [107].

Importantly, a combination of static and dynamic ocean observation is the technology of AUV docking. It plays a significant role in marine scientific research [21], marine resource development [24], and underwater operations [117]. Furthermore, AUV docking technology is considered as the future trend of ocean observation due to its expanded spatial and temporal coverage and enhanced endurance [107], and AUVs with docking stations have become particularly popular and are significant for ocean exploration [24, 25]. They improve underwater data collection capabilities and operational time [21, 22], enabling challenging tasks such as operations under sea ice [23]. Fig. 1.1 shows an example of an AUV called the Deep Profiler (DP) [26], developed under the Ocean Observatories Project by the Applied Physics Laboratory (APL) and the Oceanography Department at the University of Washington (UW). This AUV collects information from depths of 150 meters to 2,900 meters in the sea [27] and transmits the collected data to the docking station on the ocean bottom, effectively establishing a fast short-distance communication link on the sea floor.

However, the underwater environment presents a range of complex and significant challenges for docking technology, making it one of the most difficult problems in autonomous underwater vehicle (AUV) operations. The extreme conditions, such as high pressure, low temperatures, and turbulent currents, create an environment that is vastly different from more controlled terrestrial settings, complicating the task of reliable docking. One of the most critical issues to address is the precise control of positioning, which is vital for ensuring the AUV can align with the docking station in the challenging underwater terrain [118]. Additionally, the need for stable and accurate orientation adjustment becomes crucial, as even slight deviations in angle or positioning can lead to docking failures [22]. These technological challenges are further compounded by the difficulty in maintaining the stability of the vehicle in fluctuating underwater conditions, which can disrupt sensors, communication, and navigation systems. As a result of these environmental and technical challenges, the success rate for underwater docking remains notably low, with most systems achieving success rates that do not exceed 85%, and prolonged, consistent operations are rare [21]. The inherent complexity of underwater docking means that few solutions have been proposed, and even fewer have been successfully implemented in real-world scenarios. This is due in part to the difficulty in adapting traditional docking methodologies to the unique conditions found underwater, such as poor visibility and the absence of GPS signals. The limited number of successful cases highlights the ongoing challenge of designing a system that can reliably and autonomously perform docking under such extreme conditions [28, 29]. Consequently, while there have been several promising attempts, the development of a universally applicable and reliable underwater docking system remains an unsolved problem that demands further research and innovation.

Improving the data transferring procedure can be a solution to the docking challenge. Data transfer is a crucial component of docking procedures, along with localization and charging. For underwater communications, acoustic signals are the most commonly used carriers due to their long propagation distances. However, they face significant challenges in the underwater environment, including limited available bandwidth, high bit error rates, temporary connectivity losses, and propagation delays. These issues contribute to low data rates [119, 120]. Similarly, optical signals encounter problems with scattering and the requirement for a line-of-sight in underwater settings [121, 122]. As a result, radio waves are often employed for data transmission during docking procedures [123]. Wi-Fi devices operating at 2.4 GHz and 5 GHz are commonly used to facilitate this data transmission, which can provide a broadband communication link and high data transmission speed [36, 39, 124]. However, these devices require the distance between the antennas on the AUV and the docking station to be within several centimeters and at specific angles [22,28,124–126]. Such stringent requirements for the data transmission process complicate docking, particularly in terms of precision control. Therefore, we propose an out-of-line series feed slot (OLSFS) antenna operating at 2.4 GHz, which is a horizontal array of out-of-line slot antennas conformed to a cylinderical platform. The OLSFS antenna does not require any angle alignment between AUVs and docking stations, which greatly eases the requirements of the docking procedure. Additionally, this antenna was successfully deployed in the DP (see Fig. 1.1) and docking stations for the Ocean Observing Initiative [127], and it has worked reliably since then.

Although the OLSFS antenna helps simplify the rigorous docking requirements for some AUVs, similar to other Wi-Fi devices, it still requires a close distance of 2–3 cm between AUVs and docking stations. The attenuation of radio waves caused by the seawater increases with higher frequencies, making long-distance communication underwater challenging. In order to establish a longer communication link in seawater, researchers are designing underwater antennas that operate at lower frequencies to enhance the traveling distance [34,35,37,38,128–132]. However, using lower frequencies typically leads to an increase in antenna size. For instance, dipole antennas [128] and loop antennas [133] designed for underwater operation in the MHz range tend to be larger. These large antennas are unsuitable for installation on AUVs and docking stations, which often require compact design [134, 135]. To address this issue, we have designed a circular waveguide antenna loaded with high dielectric constant material, which transmits circularly polarized signals. This antenna maintains a compact size while offering an extended range for data transmission during docking. Additionally, its broad radiation pattern and circular polarization reduce the need for precise angle alignment when docking.

The remainder of this article is organized as follows: Sections II and III review the design procedure and simulation results of the OLSFS and loaded waveguide antennas for underwater communication, respectively. The antenna measurement results, along with establishing successful communication links, are explained for each antenna in the related sections. Finally, Section IV concludes the paper.

2.3 *OLSFS Antenna Background*

The basic OLSFS antenna design and its performance have been discussed in [26]. In this section, an expanded version of the OLSFS antenna design, including detailed design procedures, simulations, and experimental results, is presented. Underwater RF/microwave communication is severely constrained by the high dielectric loss of seawater at gigahertz frequencies, yet it remains attractive due to the ubiquity of low-cost 2.4 GHz transceivers and advances in conformal printed structures. The Applied Physics Laboratory's Deep Profiler (DP) uses a standard 2.4 GHz Wi-Fi chipset to upload sensor data when docked, requiring an RF link that can tolerate arbitrary vehicle orientation, a shallow (2–3 cm) separation gap, and the extreme hydrostatic pressures of the deep ocean . To meet these requirements, the antenna must provide near-omnidirectional coverage, maintain its resonant frequency under mechanical deformation, and be fully encapsulated against seawater ingress. The out-of-line series-fed slot (OLSFS) array was selected as the optimal topology: its slot-based radiating elements afford inherently wider impedance bandwidth and reduced sensitivity to substrate perturbations compared to microstrip patches, while its planar construction can be conformally wrapped onto cylindrical housings without cutting or splicing. Moreover, by using eight identical slots fed through a corporate network, the OLSFS array generates a fan-beam pattern in the

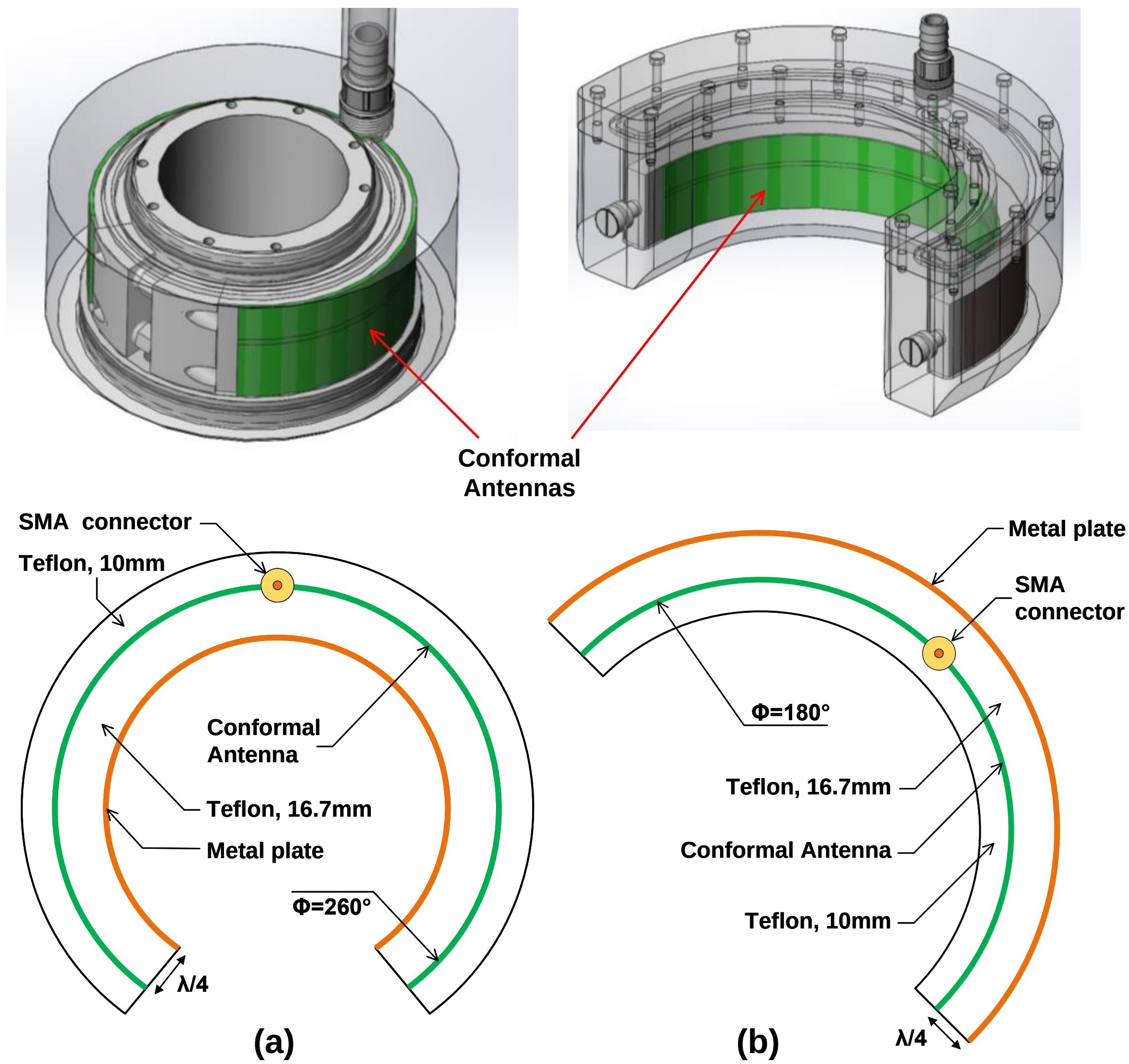

Figure 2.1: 3D and top view of (a) the docking station antenna and (b) the DP antenna.

elevation plane—ensuring coverage over the docking arc—while the horizontal alignment of slots preserves their electrical length under bending. Early prototypes of the OLSFS design demonstrated a reflection coefficient of approximately -15 dB at 2.4 GHz and a stable fan-beam radiation pattern when conformed to a 172 mm-diameter cylinder, achieving near-constant S_{21} transmission over 260° of rotation in air. Subsequent tests in a seawater tank confirmed that, despite an expected additional attenuation of roughly 22 dB over a 2 cm path, the curved assembly maintained both its resonance and beam shape, validating the slot orientation strategy for deformation immunity. Building on these foundational results, the following subsections describe (1) the analytical synthesis of individual slot elements and corporate feed, (2) the parametric optimization workflow in HFSS, and (3) the fabrication and seawater-tank measurements that together verify the OLSFS antenna's suitability for deep-sea docking communications.

2.4 *OLSFS Antenna Design Procedure*

When the DP reaches the docking station at the sea floor, the RF data transmission process is carried out using two conformal Out-of-Line Series Feed Slot (OLSFS) antennas, which are seamlessly integrated into both the DP and the docking station, as depicted in Fig. 2.1. This design is critical for maintaining reliable communication during the docking process, particularly because the orientation of the DP is often unpredictable when approaching the docking station underwater. In such an unpredictable environment, the antennas must be engineered to provide near omnidirectional radiation characteristics, ensuring robust communication regardless of the DP's orientation. This requirement is especially important for maintaining uninterrupted data transfer as the DP may not align in a fixed position relative to the docking station. The challenges posed by the deep-sea environment are considerable, especially when considering that the marine conditions are highly unforgiving for microwave-based devices. The antennas must be highly compact and efficient, with the separation between the two antennas constrained to no more than 2 to 3 centimeters. Such a compact design ensures the antennas can work efficiently in the confined space of the DP and the docking station, while still being capable of transmitting signals over the required distance. Furthermore, these antennas must be able to endure the extreme conditions of deep-sea pressure, which can reach staggering depths and put immense strain on any equipment placed at such depths. Additionally, protection from corrosive seawater is imperative, as prolonged exposure to saline conditions could degrade the performance of the antennas. To meet these demanding conditions, the OLSFS antenna is meticulously designed to conform to the cylindrical structure of the DP. This design allows the antenna to follow the natural contour of the DP, optimizing space and ensuring effective signal propagation. Moreover, the antenna is reinforced with multiple layers of protective dielectric materials, safeguarding the antenna from mechanical damage under the immense pressure exerted by the surrounding seawater. These protective layers not only provide structural integrity but also enhance the durability of the antenna, ensuring it remains functional throughout the entire docking process, even under the harshest underwater conditions. This combination of advanced antenna design and durable materials ensures that the communication link between the DP and the docking station is maintained with high reliability, contributing to the overall success of the docking procedure in deep-sea environments.

Researchers have long been investigating various antenna designs tailored for underwater environments to address the unique challenges posed by the DP docking procedure. While numerous designs have been proposed, none of them fully meet the specific design requirements for the DP, particularly given the extreme conditions of deep-sea operations. For instance, one such design developed by another team utilized a line antenna submerged in a tube filled with silicone oil. While this design initially appeared promising, it failed to deliver consistent and reliable performance under the conditions required for the docking procedure. The primary issue with this design lies in the instability of the antenna within the silicone oil. Since the line antenna is not securely fixed within the tube, it becomes prone to movement, leading to shifts in its positioning within the medium. This lack of a stable and fixed configuration directly impacts the accuracy of the signal propagation, as the antenna's position relative to the surrounding environment can change unpredictably. As a result, the signal propagation distance becomes unreliable, causing significant variations in the performance of the antenna. In an underwater environment where precise communication is essential for successful docking, this instability becomes a critical flaw. Furthermore, the unpredictability of the antenna's positioning within the silicone oil tube makes it difficult to maintain consistent signal strength and quality. The antenna's performance would fluctuate depending on its movement, making it unsuitable for a procedure that requires precise and uninterrupted communication. This unreliability in signal propagation compromises the overall efficiency of the docking process, highlighting the need for a more robust and stable antenna design capable of operating effectively in such demanding underwater conditions.

Duroid 5880 was chosen as the material for the antenna PCB because it has low loss ($\epsilon_{\mathrm{r,eff}} = 2.2$, $\tan\delta_{\mathrm{eff}} \ll 1$) and high flexibility—properties that are essential for maintaining efficient RF performance when the antenna must conform to curved surfaces in a harsh subsea environment. Its low dielectric loss ensures minimal signal attenuation across the operating band, while its mechanical compliance allows the PCB to bend without fracturing, though the exact effect of bending on the microstrip resonant characteristics remains to be fully characterized. Both microstrip antennas and printed slot antennas were investigated for this design. The microstrip version did not provide sufficient bandwidth for the required data-link reliability, and how its resonant frequency might shift when bent or subjected to external pressure was unclear. By contrast, the printed slot antenna exhibited a broader impedance bandwidth in planar prototypes and—by virtue of its slot-based radiating mechanism—was expected to maintain its resonant behavior more predictably when conformed to the cylindrical structure. Consequently, the slot antenna topology was selected for the final implementation. With the antenna length fixed at 390 mm and the slot routed directly onto the curved hull section, the docking-station side achieves an angular coverage of approximately 260° (see Fig.2.1). On the DP side, the same 390 mm slot produces a coverage of roughly 180°, owing to the tighter curvature and different mounting geometry. When the DP is fully docked, regardless of its orientation, there is always a clear signal path between the two conformal antennas—eliminating potential null zones and ensuring a continuous RF link throughout the docking procedure.

The OLSFS antenna is shown in Fig. 2.2a. In this design, the eight radiating slots are aligned to form a horizontal slot array, an arrangement that inherently resists deformation when wrapped around the DP's cylindrical surface and thus preserves the intended slot geometry. Because the slots remain effectively straight under bending, their resonant frequency remains fixed at 2.4 GHz. Feeding is implemented via a predominantly parallel corporate network: the single SMA feed at the center branches symmetrically into two equal-length feedlines, each of which splits again so that all eight slot elements receive power through identical microstrip stubs (see the red lines in the attached image). This equal-length, equal-impedance branching ensures uniform excitation—both in amplitude and phase—across every slot, maintaining a balanced current distribution without relying on series connections. The principal distinction between horizontal and vertical slot arrays lies in slot orientation relative to the curvature of the mounting surface. For a vertical slot array—where all eight slots are collinear in the vertical direction and occupy the same overall envelope—the inter-element spacing must decrease to fit within the fixed antenna dimensions. This reduced spacing can exacerbate mutual coupling and make the antenna more sensitive to small geometric distortions. Moreover, when a vertical array is conformed to the DP's hull (see Fig. 2.3b), the originally straight slots bend and warp, altering their effective length and shape and consequently shifting their resonance and

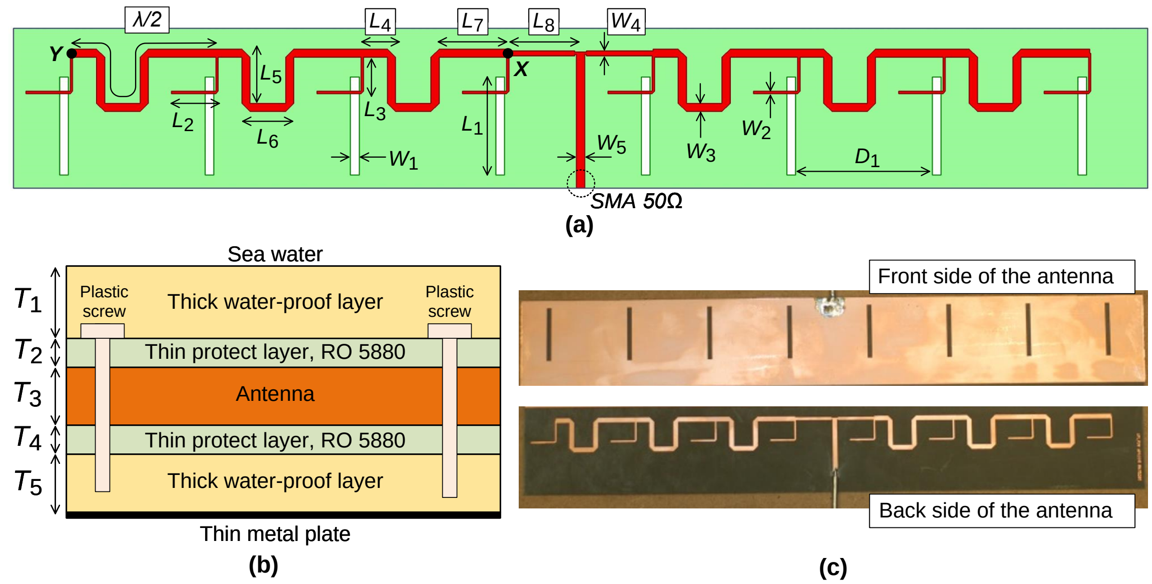

Parameters	Values
W_1	3 mm
W_2	0.8 mm
W_3	2.8 mm
W_4	1.7 mm
W_5	2.8 mm
L_1	33.6 mm
L_2	15.2 mm

Parameters	Values
L_3	12.25 mm
L_4	8.2 mm
L_5	15.8 mm
L_6	12.2 mm
L_7	23.6 mm
L_8	23 mm
D_1	50 mm

Parameters	Values
T_1	10 mm
T_2	0.508 mm
T_3	1.016 mm
T_4	0.508 mm
T_5	16.7 mm

(d)

Figure 2.2: (a) Overview of the antenna layout. (b) Layered structure. (c) Manufactured horizontal slot array antenna. (d) Optimized parameters of the designed antenna.

degrading bandwidth. By contrast, the horizontal array (Fig.2.3a) distributes the slots side by side along the axis of the hull, providing ample separation between elements and allowing each slot to maintain its straight profile under curvature. This geometry both preserves the designed slot lengths and minimizes the risk of performance variation due to bending. For these reasons, the horizontal slot-array topology was selected, eliminating the deformation-induced resonance shifts that could occur with a vertical orientation.

The design process is composed of the design of the slot antenna, feeding network, and layered structure. The manufactured antenna is shown in Fig. 2.2c, and the design parameters are

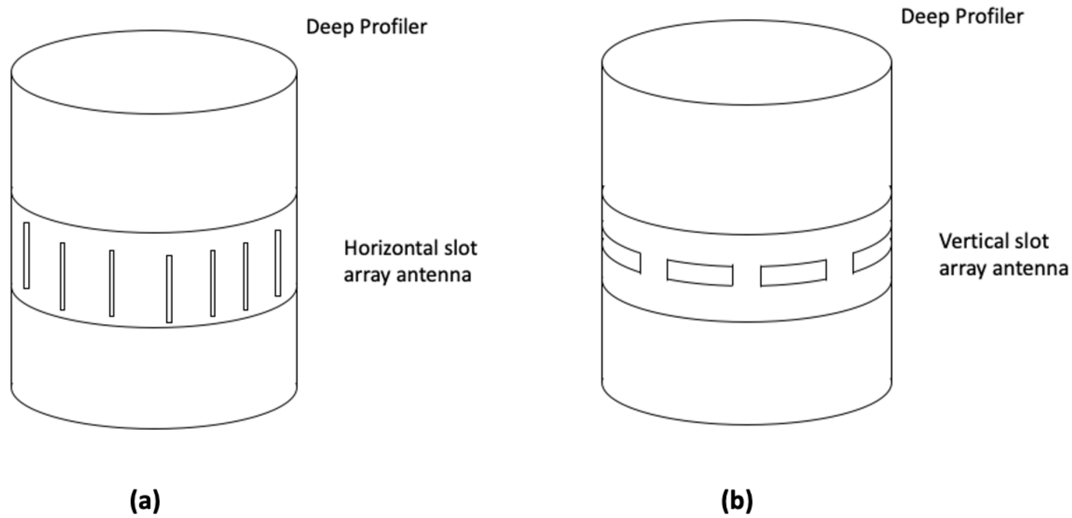

Figure 2.3: (a) Horizontal slot array antenna (b) Vertical slot array antenna

summarized in Fig. 2.2d.

The first step in the design of the OLSFS antenna is to start with some initial values for the single slot antenna and matching network, as shown in Fig. 2.2a and Fig. 2.4. Because extensive simulations are required to create a practical OLSFS antenna, we assume that the OLSFS is flat for the starting point, and the top covering layer is considered to be air. Later, we include the effects of curvature and seawater on the antenna performance and optimize the initial values. Fig. 2.4 illustrates the parameters used in the design procedure. The width of the slot $W = 3\,\mathrm{mm}$ was used in this design. The slot length L is given by (2.1):

$$L = \frac{c}{2f_r\sqrt{\epsilon_{\mathrm{r,eff}}}} \tag{2.1}$$

where f_r is the slot resonant frequency, c is the speed of light in free space, and $\epsilon_{\mathrm{r,eff}}$ is effective dielectric constant. The calculated value of L is 45.7 mm. The input impedance at the location where the feedline and the slot intersect varies along the slot edge and can be estimated by (2.2):

$$R_{in} = Z_{slot}[cos(\frac{\pi y_0}{L})]^2 \tag{2.2}$$

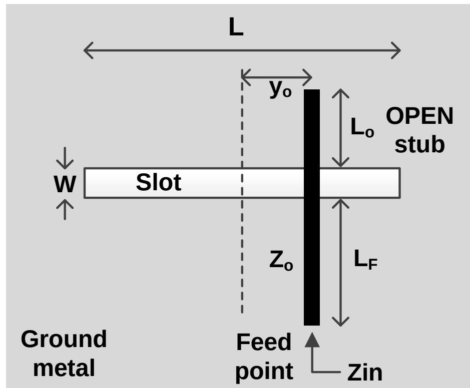

Figure 2.4: Single slot antenna design parameters.

where, Z_{slot} is the max impedance at the center and y_0 is the distance from the center [136]. The estimation of Z_{slot} for a thin slot antenna is described by [136]. R_{in} is chosen to be 100 Ω in our design. The open stub length L_0 must be close to a quarter wavelength. The microstrip line characteristic impedance (Z_0) is $100\,\Omega$, and the length of L_F is adjusted to obtain $Z_{\text{in}} = 200\,\Omega$ that is the input impedance at the starting position of the feedline. Based on the analytical method, the slot antenna usually has S_{11} around -5 dB, but an optimization process of L_0 can usually improve the S_{11} to -15 dB. After including the effect from the layered structure discussed later, L = 33.6 mm, L_0 = 11.4 mm, L_F = 13.5 mm, and $y_0 = 12.3$ mm will make the antenna resonate at 2.4 GHz with S_{11} of less than -15 dB.

Once the design of the single-slot antenna element is completed, the feeding network is designed as follows. The electrical antenna separation between two slots is half a wavelength to create a uniform excitation of 8 elements. However, the physical separation of each slot is 50 mm to create a dense field distribution. As explained before, each slot antenna delivers an input impedance of $Z_{\text{in}} = 200\ \Omega$ at the beginning of the feeding line, indicated by point Y in Fig. 2.2a. A 50 Ω half-wavelength transmission line is used to connect all elements except for the two center elements. After connecting four slot antennas in parallel, an effective input impedance at point X in Fig. 2.2a is 50 Ω. The impedance of a single feeding line is 200 Ω. When two of these lines are connected in parallel, the effective impedance becomes 100 Ω. Adding a third line in parallel results in an effective impedance of $66.67\,\Omega$. Finally, connecting four lines in parallel—representing the complete structure on one side of the feeding network—yields an effective impedance of $50\ \Omega$, as previously mentioned. A quarter wave transformer (L_8 in Fig. 2.2a) of $70.7\ \Omega$ converts the impedance to $100\ \Omega$ on each side at the center section. Since the two ends with input impedance of $100\ \Omega$ are connected in parallel, the effective impedance at the center is $50\ \Omega$. Therefore, a final T-junction is used to connect to the $50\ \Omega$ main feed point. Since the slots of the OLSFS antenna will radiate toward both top and bottom directions, a metal plate is attached on the bottom side to create an effective open circuit using a "quarter wave section with SHORT" to increase the antenna gain as shown in Fig. 2.2b. The layout is carefully designed to create a uniform element excitation. The free space antenna gain is 10.3 dB. The electric field orientation is perpendicular to the slot orientation.

The antenna cannot be directly exposed to seawater, so a multi-layer protective stack is introduced around the PCB. Fig.2.2b depicts the cross-sectional layered structure. Two thick, waterproof Teflon layers encapsulate the antenna and inner dielectric stack, providing a robust barrier against corrosive seawater ingress. The upper Teflon layer is 10 mm thick—a thickness determined through an optimization routine that balanced mechanical robustness with minimal detuning of the slot resonance due to the proximity of lossy seawater. Beneath the antenna PCB sits a thin metal plate backed by an additional 6.7 mm of Teflon, bringing the combined lower waterproof thickness to 16.7 mm. This metal–dielectric–metal sandwich forms an effective open-circuit boundary condition at the back of the antenna, forcing radiation to the outward side and thereby establishing a unidirectional pattern. To cushion the PCB and further isolate the radiating slots from mechanical stress, thin slices of RO 5880 are interleaved immediately above and below the antenna layer. These RO 5880 inserts (each on the order of 0.5–1.0 mm thick) serve both as compliant spacers—absorbing bending strains—and as dielectric buffers that preserve the designed impedance match. Moreover, because the RO 5880 layers have a smooth, machined surface, they protect the antenna PCB from direct contact with the rougher Teflon layers, preventing abrasion and ensuring long-term structural integrity. The overall stacked assembly thus ensures seawater protection, mechanical support, and controlled electromagnetic boundary conditions, all while maintaining the antenna's resonant frequency at 2.4 GHz and its intended radiation characteristics.

2.5 *OLSFS Antenna Simulation and Experimental Results*

Figure 2.2a presents the top-view geometry of the OLSFS antenna as modeled in the full-wave simulator. All eight slot elements, the corporate feed network, and the surrounding ground plane are rendered to scale, allowing direct visualization of element placement, feedline routing, and substrate boundaries. The corresponding numerical values for every critical dimension—slot lengths L_i, slot widths W_i, element spacings D_1, feed-stub lengths, and layer thicknesses—are compiled in Fig.2.2d. These values reflect the outcome of a two-stage design methodology: first, an analytical synthesis based on transmission-line and resonator theory to establish initial estimates, and second, iterative tuning through HFSS parametric sweeps to refine the impedance match, bandwidth, and pattern conformity. Following the simulation procedures outlined previously, the reflection coefficient S_{11} of the OLSFS antenna reaches approximately -15 dB at the center frequency of 2.4 GHz, as plotted in Fig.2.5a. This level of return-loss indicates that over 96 % of the incident power is delivered into the radiating slots, satisfying the link-budget requirements for reliable data transfer. The far-field radiation characteristics, shown in Fig. 2.5b, exhibit the intended fan-beam pattern in the E-plane: a narrow elevation beamwidth of roughly $20°$ combined with a broad azimuthal spread exceeding $180°$. This pattern guarantees coverage across the docking interface while suppressing energy in unwanted directions. Finally, the full 3D radiation plot in Fig. 2.5c confirms the unidirectional nature of the antenna: energy is radiated predominantly into the forward hemisphere, with measured front-to-back ratio better than 10 dB in simulation. Collectively, these simulated results validate both the impedance performance and the beam-shaping objectives of the OLSFS antenna design.

The next simulation involves placing two flat OLSFS antennas in seawater to form a communication link. Both the reflection and the transmission coefficients between the two antennas are simulated. Fig. 2.6a shows the configuration of the two flat OLSFS antennas positioned next to each other. The distance between the antennas, including the protective layers, is set to 2 cm. In the DP project, the antenna needs to be bent around the docking station and the DP, as illustrated in Fig. 2.1a. Therefore, it is crucial to test the performance of the curved structure in simulations. In the real-world project, the antenna installed in the docking station covers an angle of $260°$, while the antenna on the DP covers $180°$. This configuration ensures that there is always a clear signal path between the docking station and the DP, regardless of the DP's orientation during docking.

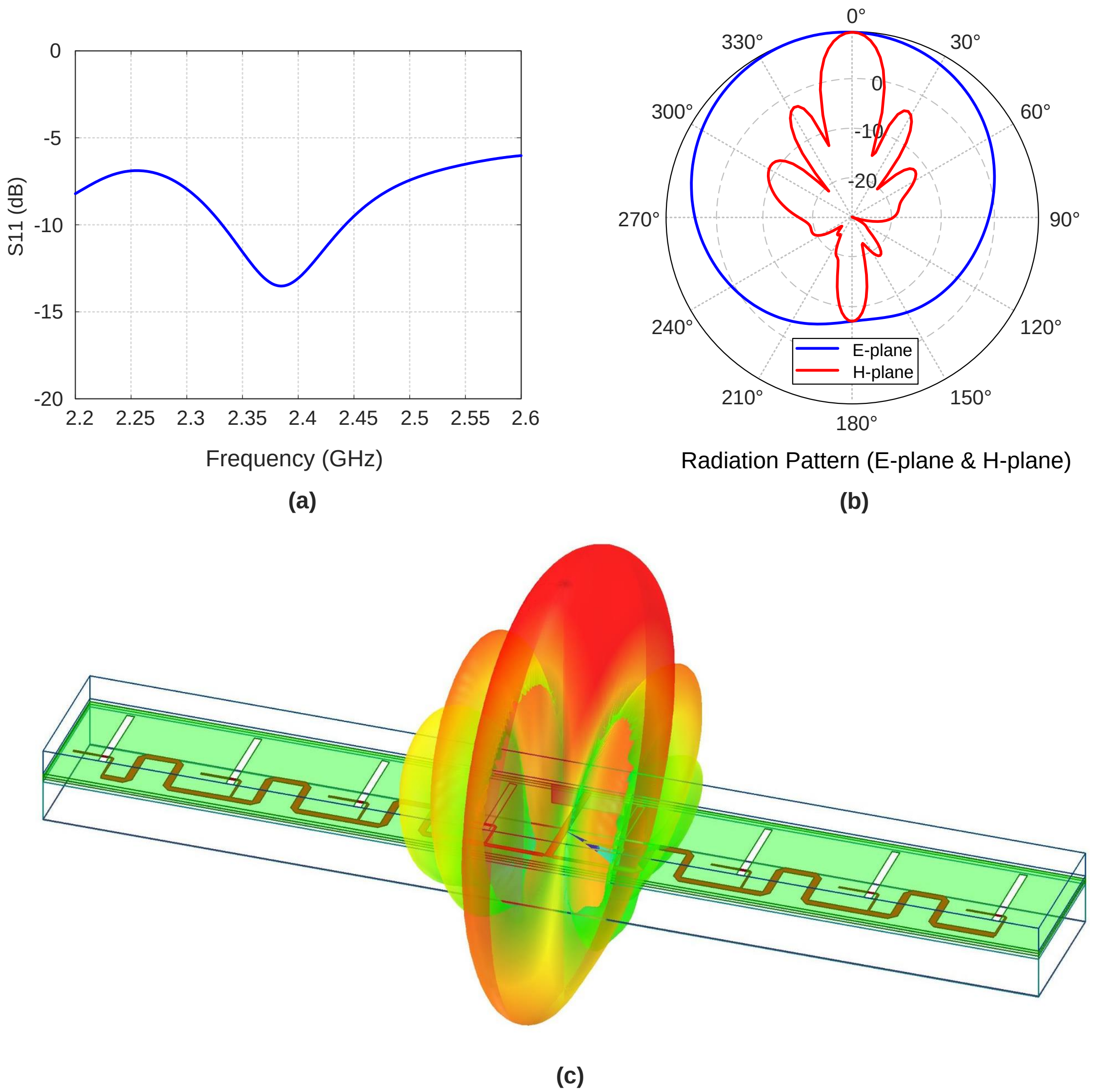

Figure 2.5: (a) Reflection coefficient S_{11}. (b) Normalized E- and H-plane radiation patterns. (c) 3D radiation pattern with the antenna.

The diameters of the cylindrical structures where the antenna is mounted on the docking station and the DP are designed to be $172\,\text{mm}$ and $248\,\text{mm}$, respectively. Consequently, the length of the antenna is set at $390\,\text{mm}$. These same dimensions are used in the simulation. Fig. 2.6b illustrates the simulation setup with the two bent antennas positioned on the DP (outer) and the docking station (inner). A layer of seawater, 2 cm thick, is placed in the gap between the DP and the docking station.

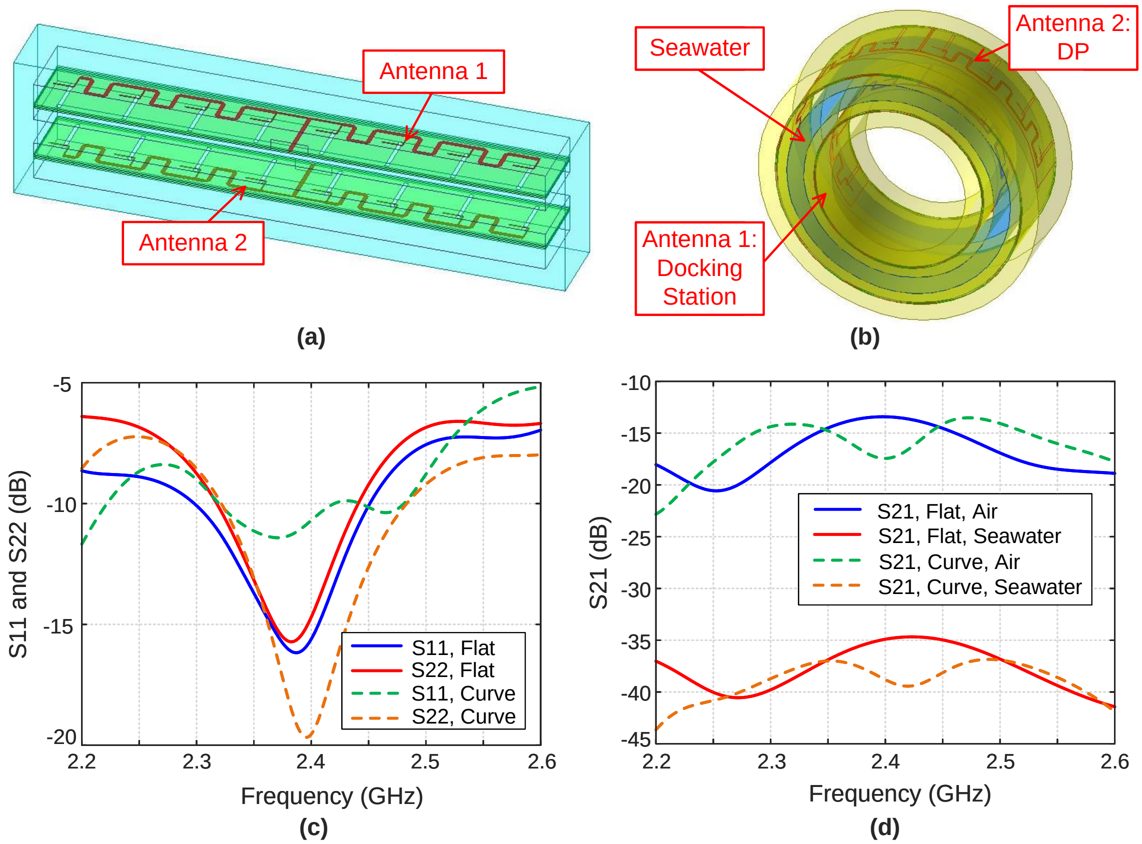

Figure 2.6: (a) Two flat OLSFS antennas communicate with each other. (b) Two conformal OLSFS antennas communicate with each other. (c) Reflection coefficients of flat and conformal designs. (d) Transmission coefficients of flat and conformal designs in air and seawater.

Fig. 2.6c shows the reflection coefficients of each antenna, and it is observed that the S_{11} and S_{22} values for the flat case are around -15 dB. Although bending the antennas changes the reflection coefficients, both S_{11} and S_{22} are still below -10 dB, and the slot resonance frequency does not shift. This stability benefits from the orientation of the slots, which are designed to ensure that bending the antenna does not alter the slot length. Fig. 2.6d presents the transmission coefficients between the two antennas in air and seawater for both flat and curved designs. It is shown that bending the antennas does not deteriorate the communication link between the two antennas. The presence of seawater introduces an additional 22 dB loss to the transmission coefficient for both cases.

The complex dielectric constant of seawater used in the simulation is calculated by Debye's formula [137] shown below.

$$\epsilon_{SW}^{'} = \epsilon_{SW\infty} + \frac{\epsilon_{SW0} - \epsilon_{SW\infty}}{1 + (2\pi f \tau_{SW})^2} \tag{2.3}$$

$$\epsilon_{SW}^{''} = \frac{2\pi f \tau_{SW}(\epsilon_{SW0} - \epsilon_{SW\infty})}{1 + (2\pi f \tau_{SW})^2} + \frac{\sigma_i}{2\pi f \epsilon_0} \tag{2.4}$$

In the equation above, ϵ_0 is the permittivity of free space, f is the frequency, $\tau_{SW} = 17.1$ ps is the relaxation time of seawater, $\epsilon_{SW\infty} = 4.9$ is the higher limit frequency dielectric constant, $\epsilon_{SW0} = 78.46$ is the lower limit frequency dielectric constant, and $\sigma_i = 2.719$ S/m is the ionic conductivity. The calculated relative permittivity of seawater at 0 °C is $\epsilon_r = 74 - 38j$ at 2.4 GHz. Zero degrees Celsius is selected as it is roughly the temperature of deep-sea [138]. Threrfore, the attenuation can also be found analytically by assuming plane waves propagate in seawater. The expression of signal propagation and decay in a lossy material can be expressed as $e^{-jk_0L\sqrt{\epsilon_r(1-jtan\delta)}}$, where k_0 is the free-space wavenumber, L is the propagation distance, and ϵ_r and $tan\delta$ are the relative dielectric constant and loss factor of the surrounding medium. Through calculation, for $2cm$ propagation, the attenuation is $-18dB$, which is close to the simulation results. The attenuation of electromagnetic waves in seawater has been studied by various groups. One study indicates that the attenuation is about $25dB$ when electromagnetic wave propagates in seawater about $2cm$ [139], which is close to the above-calculated result.

The final simulation investigates the communication between the two curved antennas displayed in Fig. 2.6b. One antenna is fixed while the other is rotated from $0°$ to $360°$. This rotation is essential to ensure that a signal path is maintained regardless of the antennas' orientation relative to each other. Fig. 2.7a and b illustrate the reflection and transmission coefficients of the communication link at 2.4 GHz in both air and seawater, respectively. It is evident that there is consistently good matching at both ports, S_{11} and S_{22}, with values lower than -10 dB. Regarding the transmission between the two antennas, S_{21} shows minimal variation as the antenna is rotated through $360°$. Thus, the simulation suggests that the orientation of the antenna on the DP does not significantly affect the communication link to the docking station. Furthermore, Fig. 2.7c presents the electric field distribution on the two antennas and across the seawater layer when the antenna in the docking station (inner antenna) transmits signals at $0°$, $90°$, and $180°$ rotations, as indicated by the red arrow. The results demonstrate

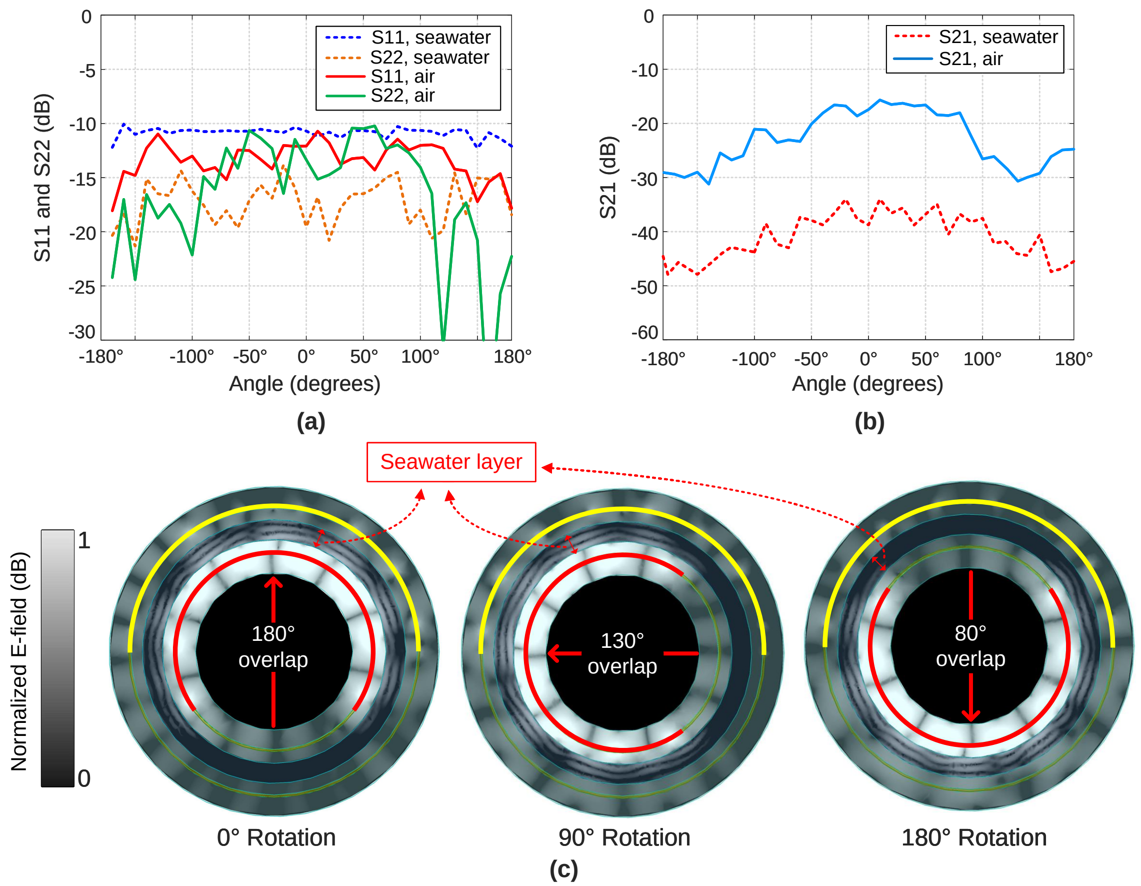

Figure 2.7: Antenna rotation test at 2.4 GHz: (a) S_{11} and S_{22} as a function of the rotated angle. (b) S_{21} as a function of the rotated angle. (c) Electric field distribution at different rotated angles.

that the electric field propagates effectively through the seawater layer at all three angles, allowing a portion of the electric field to successfully reach the antenna on the DP (outer antenna).

The first experimental verification, depicted in Fig. 2.8, is designed to confirm the angular coverage provided by the conformal OLSFS antenna when mounted on the docking-station cylinder. Recall that in our design, the docking-station side is intended to cover an arc of approximately 260°. To measure this coverage, the antenna under test is affixed to a precision rotary stage that replicates the $172,$mm-diameter curvature of the docking station. An S-band rectangular waveguide—connected to a calibrated vector network analyzer—is positioned at a fixed point outside the antenna's radial extent, as shown in Fig. 2.8a. By rotating the antenna in one-degree increments through the full

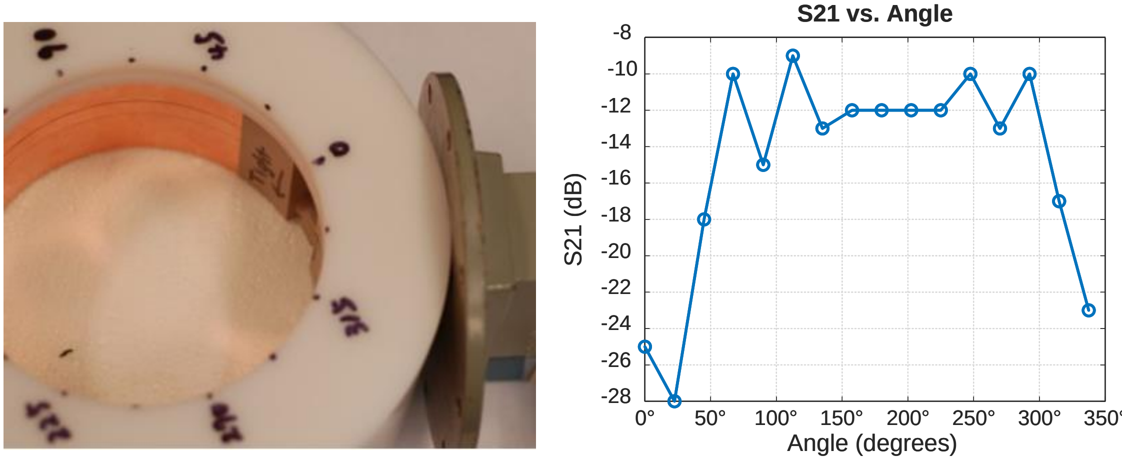

(a) **(b)**

Figure 2.8: (a) Test setup to measure S_{21} of docking antenna by angle. (b) Measurement results of S_{21} versus angle.

$360°$ range, we record the forward transmission coefficient S_{21} at each angular position. A threshold of -20,dB is chosen as the minimum acceptable coupling level for reliable data transfer, based on the link-budget requirements of the DP's Wi-Fi chipset. Figure 2.8b plots the measured S_{21} versus azimuth angle. Over a contiguous span of $260°$, the transmission coefficient remains above -20,dB, demonstrating that the antenna maintains sufficient coupling to the waveguide port. Outside this span, S_{21} falls below the threshold, marking the edges of the coverage arc. These results are in excellent agreement with our full-wave simulation predictions, confirming that the horizontal slot alignment and feed network deliver the designed omnidirectional behavior across the intended docking arc.

Moreover, Fig. 2.9a illustrates the full experimental arrangement used to characterize both the reflection and transmission coefficients of the conformal OLSFS antennas under realistic mounting conditions. In this configuration, two identical antennas are wrapped around precision-machined cylindrical fixtures that replicate the docking station (inner cylinder) and the DP vehicle (outer cylinder). Each antenna is connected via semirigid coaxial cables to a vector network analyzer (VNA), with calibrated 3,dB attenuators inserted immediately adjacent to each antenna port to protect the receivers and maintain a flat power response across the band. Fig. 2.9b provides a detailed view of the cabling layout and connector interfaces in the actual docking-station and DP

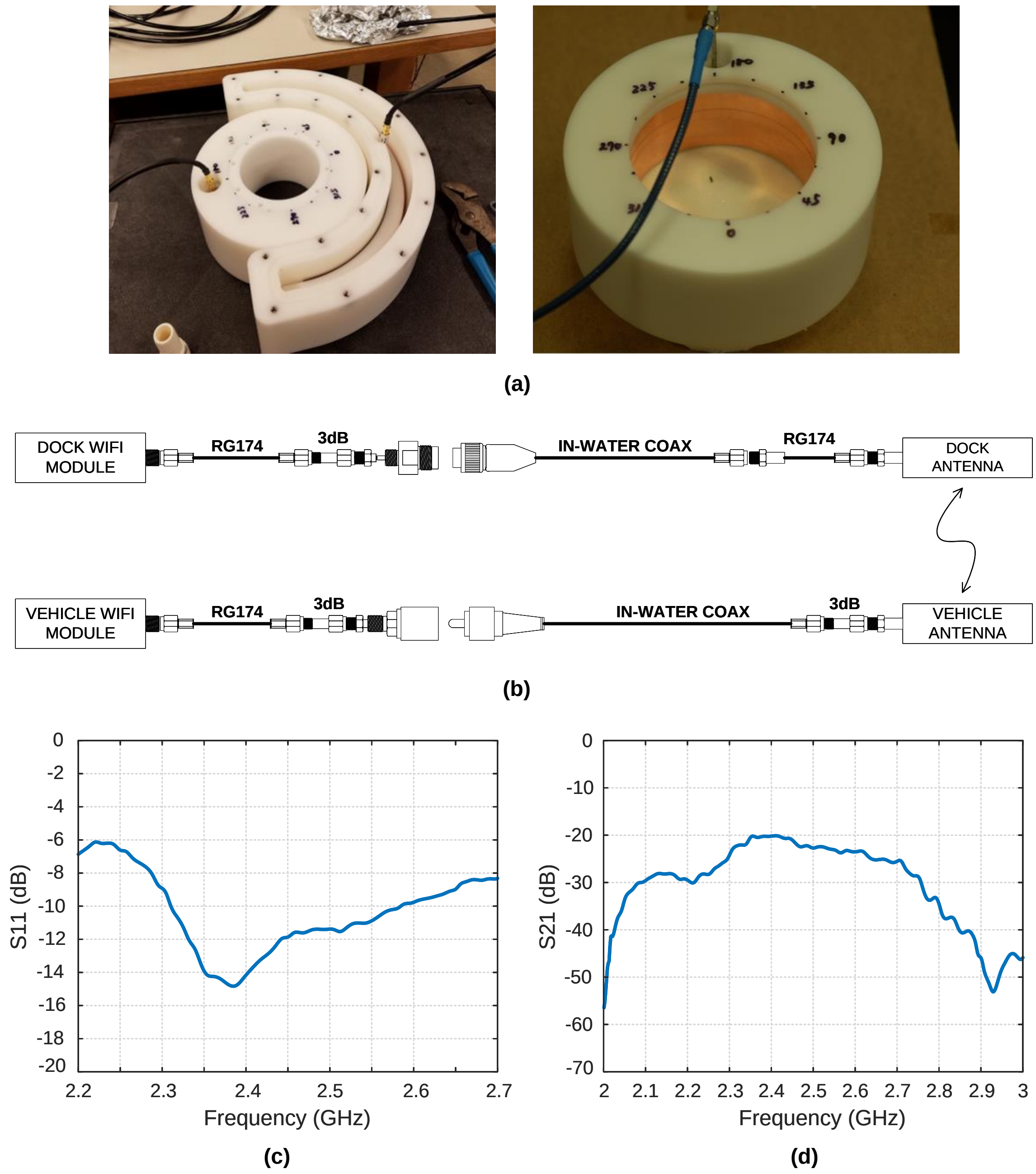

Figure 2.9: (a) Setup to measure S parameters in air. (b) Diagram of RF Network from Dock to Vehicle. (c) Measured S_{11} in the air. (d) Measured S_{21} in the air for two antennas separated by 2 cm.

assembly. The same cabling harness and connector types are used both in situ on the vehicles and in the VNA testbed to eliminate discrepancies arising from connector mismatch or cable flexure. All cables are phase-matched and routed to minimize bending losses and ensure that measured scattering parameters faithfully represent the antenna performance rather than the test fixture. The measured return loss of each antenna in free space is plotted in Fig.2.9c, showing $S_{11} \approx -15$,dB at 2.4 GHz for both the dock and DP units—consistent with simulation and flat-antenna measurements. Fig.2.9d then presents the measured insertion loss S_{21} when the two antennas are separated by approximately 2 cm in air. Owing to the inclusion of 3,dB attenuators at both ports and the relatively long cable runs required to wrap around the cylinders, the observed S_{21} is reduced to about -20,dB—slightly lower than the ideal simulated value. Introducing 2 cm of seawater between the antennas (as per Fig. 2.6d) adds an additional ~ 22,dB of attenuation, yielding a net S_{21} of approximately -42,dB. In this measurement setup, the system noise floor is around -70,dB, resulting in a signal-to-noise ratio of approximately 28 dB for the final, seawater-filled assembly—sufficient for reliable data demodulation in the DP's Wi-Fi chipset.

Finally, Fig. 2.10a illustrates an emulation of the underwater communication system presented in Fig.2.9b. This setup measures modem-to-modem transfer throughput by replacing the antenna system with an adjustable attenuator. As shown in Fig.2.10b, the system performs optimally within a narrow attenuation range of -60 dB to -80 dB. When the attenuation level falls below -40 dB, the modem becomes saturated, resulting in either slower data transfer or a complete halt. The calculated losses associated with the antenna system, combined with additional losses from seawater, yield a total loss within the -60 dB to -80 dB range. This ensures a satisfactory data transfer rate when the separation distance between the two antennas is approximately 2–3 cm.

2.6 *Loaded Waveguide Antenna Background*

The second antenna system focuses on establishing robust communication links over decimeter-scale distances in seawater by exploiting the lower attenuation at VHF and UHF frequencies. Loaded waveguide antennas, as detailed in [98], employ a dielectric-filled or water-filled waveguide section to lower the cutoff frequency and support guided modes that can propagate through conductive seawater with manageable losses. By operating in the VHF/UHF bands, this design overcomes the severe exponential decay faced at 2.4 GHz, enabling reliable links over tens of centimeters rather than just 2–3 cm [26]. The loaded waveguide's geometry and dielectric loading are optimized to balance

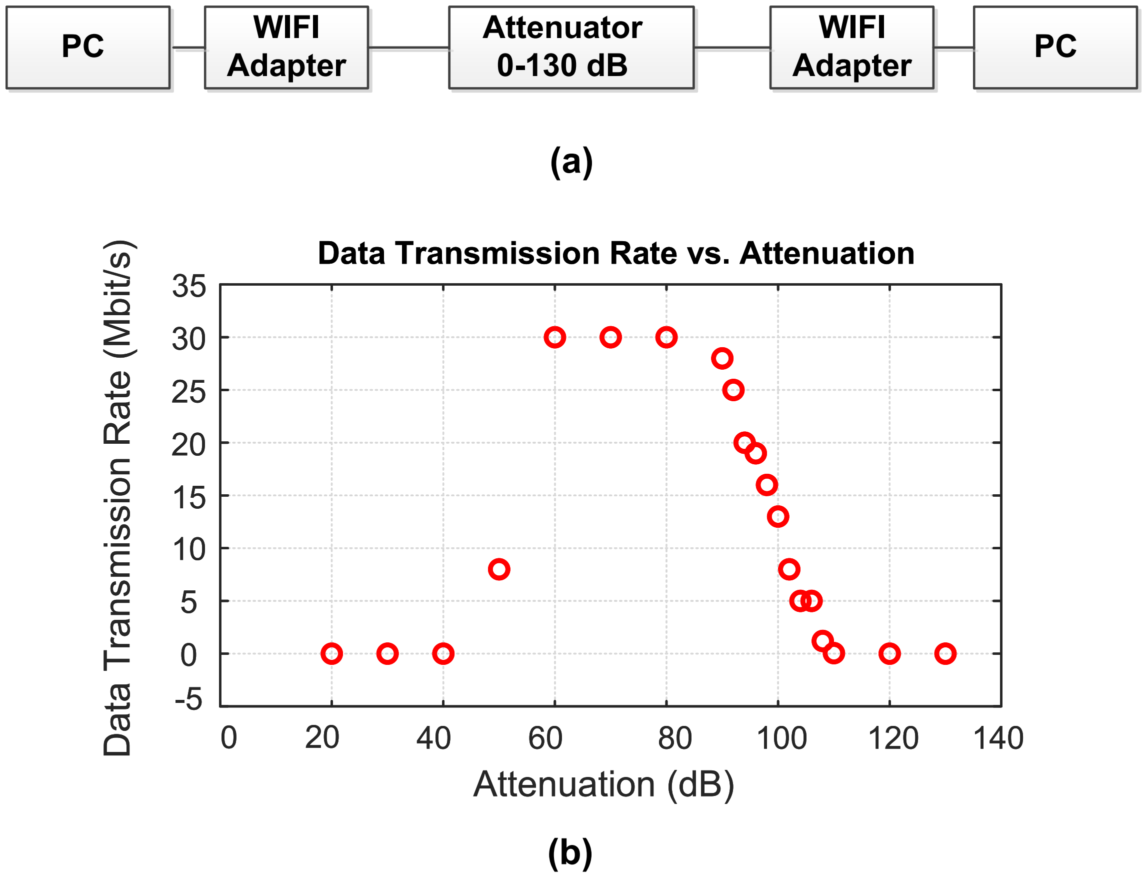

Figure 2.10: (a) Setup to measure data rate over attenuation level. (b) Data rate over attenuation level.

bandwidth, radiation efficiency, and mechanical ruggedness—critical factors when integrating with the DP's pressure-tolerant housing. Its broad, fan-shaped radiation pattern ensures that the field covers the entire docking aperture without creating deep nulls, while the use of circular polarization further mitigates orientation mismatches and multipath fading in the heterogeneous seawater environment. As illustrated in Fig. 2.11a, this combination of extended range, polarization diversity, and wide beamwidth not only simplifies the DP's approach trajectory but also reduces the need for active alignment systems, thereby enhancing the overall reliability and autonomy of deep-sea docking procedures. In later sections, the design's performance will be quantified through full-wave electromagnetic simulations and validated with controlled laboratory experiments.

2.7 *Loaded Waveguide Antenna Design Procedure*

In this part, we expand our previous study on loaded waveguide antennas with a high dielectric constant material [98] for designing a compact, broad-beamwidth, and circularly polarized antenna to operate at the lower side of UHF frequencies. This choice is motivated by the need to reduce propagation loss and increase communication distance in harsh environments such as underwater communication systems, where signal attenuation is a critical issue. By operating at lower frequencies, we aim to minimize the signal decay, but this comes with the challenge of larger antenna dimensions. To overcome this trade-off, we integrate high dielectric constant materials into the waveguide, modifying its characteristics for more efficient performance.

The most significant challenge in employing RF/microwave signals for undersea communication links is the substantial signal attenuation caused by seawater. The propagation and decay of signals in a lossy medium can be mathematically expressed as:

$$e^{-jk_0L\sqrt{\epsilon_r(1-j\tan\delta)}}$$

where k_0 represents the free-space wavenumber, L denotes the propagation distance, and ϵ_r and $\tan\delta$ are the relative dielectric constant and loss factor of the surrounding medium, respectively. For a given material and propagation distance, lower frequencies experience reduced signal decay, but this advantage is often counterbalanced by the increased size of devices that operate at these lower frequencies. This trade-off is particularly undesirable for undersea systems, where compactness and efficient energy usage are critical. To mitigate this, we incorporate high dielectric constant materials ($\epsilon_{\text{r,eff}} \gg 1$) into the waveguide, which effectively shortens the wavelength to $\lambda_0/\sqrt{\epsilon_{\text{r,eff}}}$, where λ_0 is the free-space wavelength, and $\epsilon_{\text{r,eff}}$ is the effective dielectric constant of the loaded material. This reduces the physical size of the waveguide, while still maintaining the benefits of lower frequencies in terms of signal attenuation.

For this design, a mixture of distilled water ($\epsilon_{\text{r,eff}} = 81$) and antifreeze ($\epsilon_{\text{r,eff}} = 64$) is selected as the loading material due to its unique advantages in underwater applications. Firstly, the volume of this mixture changes similarly to seawater as pressure increases with depth, making it suitable for deep-sea communication. Secondly, the antifreeze ensures that the mixture does not freeze even in

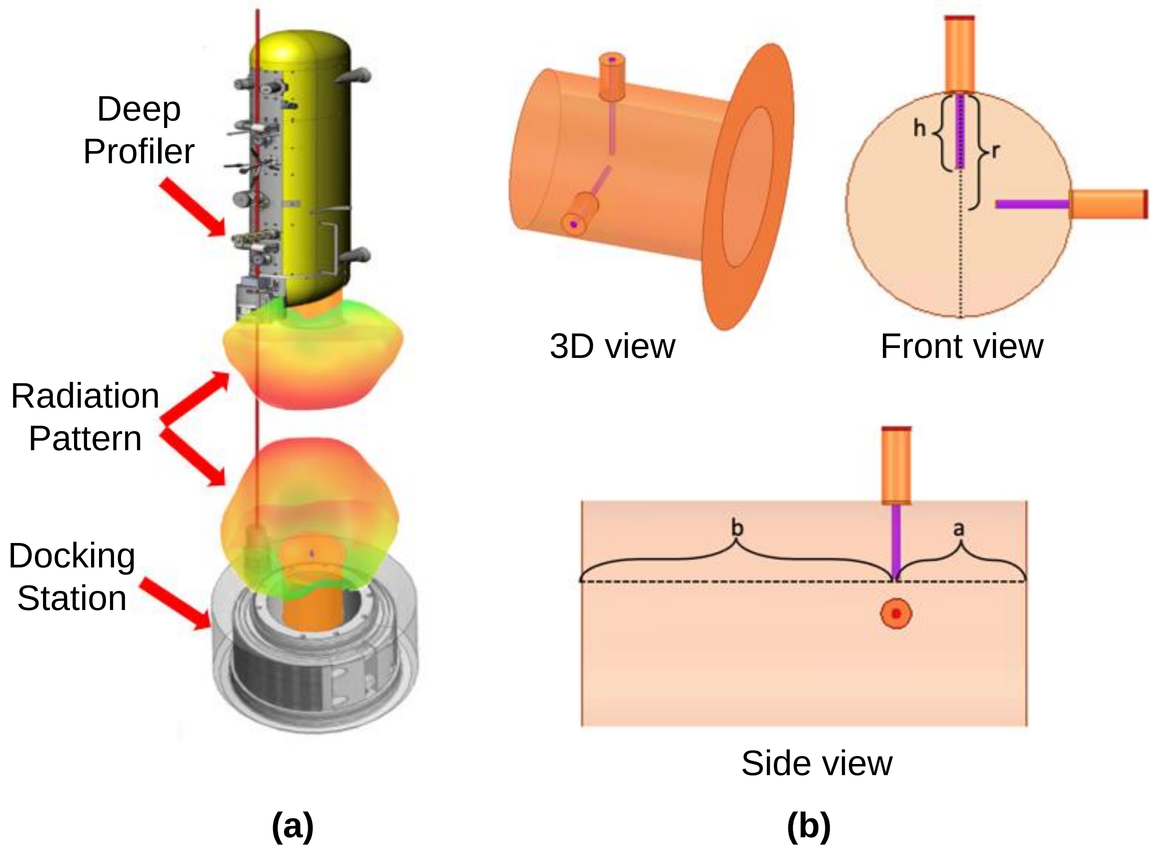

Parameters	a	b	h	r
Values	33 mm	117 mm	23.5 mm	36 mm

(c)

Figure 2.11: (a) The DP communicates with the docking station. (b) Different views of the loaded waveguide antenna. (c) Optimized parameters of the designed antenna.

very cold underwater environments, which is critical for reliable operation in polar regions. Thirdly, this mixture demonstrates a good dielectric constant match to seawater, which reduces reflection losses and improves the efficiency of signal transmission. Finally, the loading material is inexpensive compared to other high dielectric constant materials, such as titanium dioxide TiO_2 ($\epsilon_{\text{r,eff}} = 96$), and it has a small loss tangent ($\tan\delta_{\text{eff}} \ll 1$), further optimizing its performance.

As shown in Fig. 2.11b, two coaxial connectors are inserted perpendicularly to the circular waveguide. Circularly polarized waves are generated by introducing a 90° phase shift between the feed points, which reduces the sensitivity of the docking process to misalignment between the transmitting and receiving antennas. This design ensures that the communication link remains reliable even if there is slight misalignment between the antennas during the docking process. The design incorporates four critical parameters: the waveguide radius (r), the separation between the feed point and the copper back wall (a), the protrusion depth of the coaxial connector's inner conductor (h), and the waveguide extension (b).

The waveguide radius r is approximated using the cutoff frequency $f_{c_{11}}$ for the TE_{11} mode of a loaded circular waveguide, as described in [140]:

$$r = \frac{p_{11}^{'}}{2\pi f_{c_{11}} \sqrt{\mu_0 \epsilon_0 \epsilon_{\text{r,eff}}}} \tag{2.5}$$

where $p_{11}^{'}$ denotes the first root of the derivative of the Bessel function $J_1(x)$. The separation parameter a is set to approximately one-quarter of the guided wavelength $\lambda_g/\sqrt{\epsilon_{\text{r,eff}}}$, creating an open-circuit condition on one side of the feed location. This configuration directs electromagnetic waves toward the intended side of the waveguide, ensuring efficient transmission. The insertion depth h of the coaxial connector is critical for achieving optimal coupling between the coaxial connector's copper core and the waveguide. These parameters, along with the waveguide extension b, are fine-tuned using Ansys HFSS to achieve the desired radiation pattern and input matching conditions. The optimized values for all dimensions are presented in Fig. 2.11c.

In summary, the integration of high dielectric constant materials into the waveguide design, along with the use of circular polarization and the precise tuning of critical geometric parameters, allows us to develop an efficient, compact antenna capable of reliable undersea communication over longer distances, while mitigating the inherent signal losses due to seawater attenuation.

2.8 *Loaded Waveguide Antenna Simulation and Experimental Results*

Comprehensive simulations and experiments are conducted to verify the performance of the loaded waveguide antennas in seawater. Fig. 2.12 shows how the two waveguide antennas communicate with each other in the seawater in the simulation environment of Ansys HFSS. The loaded material

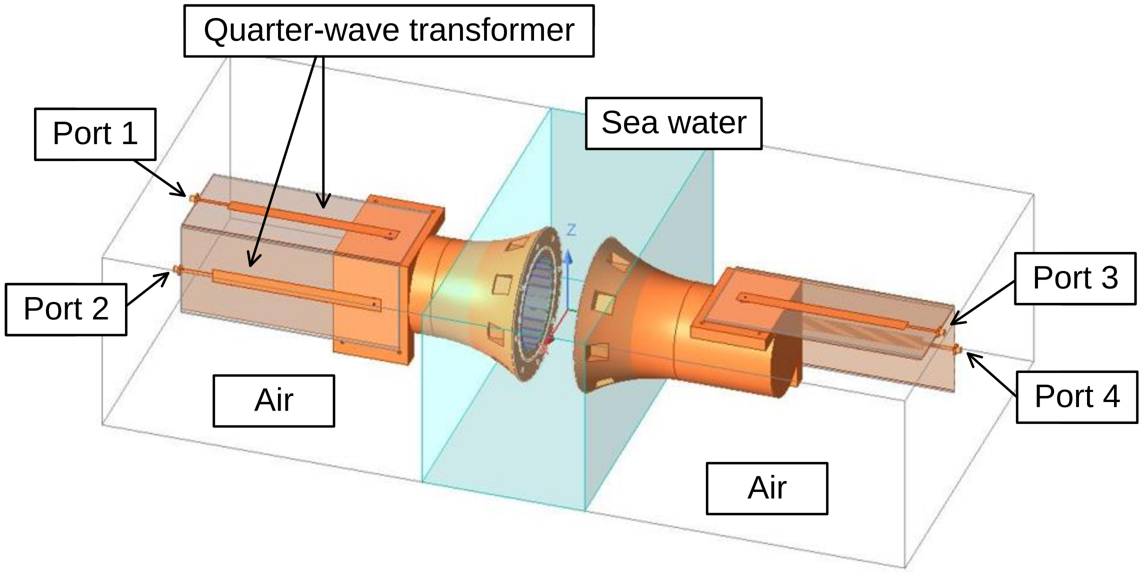

Figure 2.12: Simulation setup to test loaded waveguide antenna.

used in the simulation is self-defined to simulate the mixture of 75% distilled water and 25% antifreeze. Based on the measurement in the lab, this liquid has a relative permittivity of 80.37 and a loss tangent of 0.032 at 0 °C and around 300 MHz frequency. The material inside the waveguide will affect the input impedance at the feeding point. Based on the simulation in Ansys HFSS, the impedance is 9 Ω at the feeding location; therefore, a 21 Ω quarter-wave transmission line is needed to match the input impedance to a 50 Ω SMA connector. As will be shown shortly, a cover needs to be attached to the opening of the waveguide to prevent water leakage, and such a cover with both grooves for the O-ring and holes for nuts and bolts is added to include the potential effect in the simulation results. Sea water is placed in the middle of the two antennas to simulate the effect when the two antennas are communicating with each other in the deep sea. The relative permittivity of the seawater is also obtained by Debye's formula shown in (2.3) and (2.4). At temperatures close to 0 °C and around 300 MHz frequency, the calculated relative permittivity is $\epsilon_r = 78 - 165j$, which also corresponds to a conductivity of $2.75\ \mathrm{S/m}$. In the real world, only the front section of the antenna will be exposed to seawater, and the later feeding network should be installed into either the AUV or the docking station; therefore, in the simulation, the remaining part of the waveguide antenna,

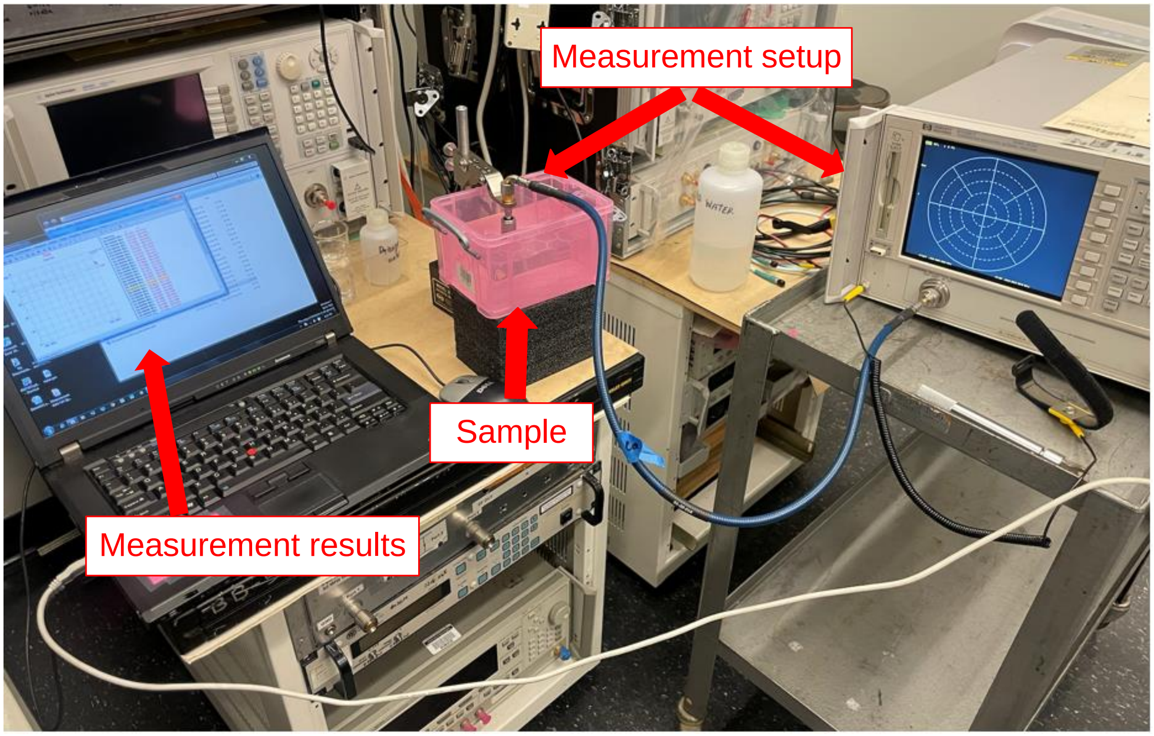

Figure 2.13: The setup to measure liquid permittivity.

including the feeding network, is exposed to air. Signals with 90° phase shift are fed into the two ports of each antenna to create a circularly polarized signal.

Permittivity measurement is a critical component of the simulations and experiments in this research. We need to measure the permittivity of seawater by adding sea salt to freshwater to achieve a permittivity of $\epsilon_r = 78 - 165j$ at around 300 MHz. Additionally, the permittivities of mixtures of distilled water and different percentages of antifreeze are important to determine the optimal percentage of antifreeze in the mixture and to provide the data necessary to build the loaded waveguide model in the simulation. The permittivity measurement setup (Keysight 85070E Dielectric Probe Kit) is shown in Fig. 2.13. The permittivities of distilled water and antifreeze mixture solutions containing 0%, 25%, 50%, and 75% antifreeze are measured at 0°C and 25°C. The results are recorded in Table 2.1. For this experiment, the 25% antifreeze mixture was selected, as this level of antifreeze is sufficient to prevent the water from freezing at 0°C and also has a low

Table 2.1: Averaged permittivity for different percentages of antifreeze in the mixture at 0 °C and 25 °C for 200-to-500 MHz range.

0 °C			
	Re(ϵ_r)	**Im(ϵ_r)**	$\tan\delta$
0 %	–	–	–
25 %	80.37 ± 0.23	2.55 ± 0.89	0.032 ± 0.011
50 %	77.00 ± 0.071	3.82 ± 0.86	0.050 ± 0.011
75 %	72.70 ± 0.089	4.29 ± 1.00	0.059 ± 0.014

25 °C			
	Re(ϵ_r)	**Im(ϵ_r)**	$\tan\delta$
0 %	79.88 ± 0.17	1.70 ± 0.71	0.021 ± 0.009
25 %	76.04 ± 0.18	1.49 ± 0.65	0.020 ± 0.009
50 %	73.25 ± 0.33	1.62 ± 0.81	0.022 ± 0.011
75 %	65.78 ± 0.32	1.94 ± 0.85	0.030 ± 0.013

enough loss tangent compared to higher concentrations of antifreeze. Since the permittivities do not vary much from 300 MHz to 500 MHz based on the measurements, average values are taken for the different antifreeze concentrations. Furthermore, for each concentration, measurements are repeated five times to obtain better average values. It is important to note that both the real and imaginary parts of the permittivities do not change significantly from 25°C to 0°C, indicating that all experimental results obtained at room temperature would not vary much when the antennas are in the deep sea, where the temperature can be close to 0°C.

The prototype antenna is shown in Fig. 2.14. The antenna body is manufactured using 3D printing technology based on a model from the simulation, with ABS filament as the printing material. To ensure the conductivity of the waveguide surface, both the outer and inner surfaces of the structure are coated with conductive paint spray (MG Chemicals 843AR-340G, Silver-Coated Copper). This section focuses solely on the electromagnetic behavior of the loaded waveguide antenna. For high pressure and harsh underwater environments, other mechanical considerations are also necessary. As shown in Fig. 2.14a, the input signal fed into the 90° hybrid component (Mini-Circuits ZX10Q-2-3-S+) produces two signals with a 90° phase shift that are sent to the waveguide through the matching circuit composed of the quarter-wave transformer. Fig. 2.14b shows the two feeding

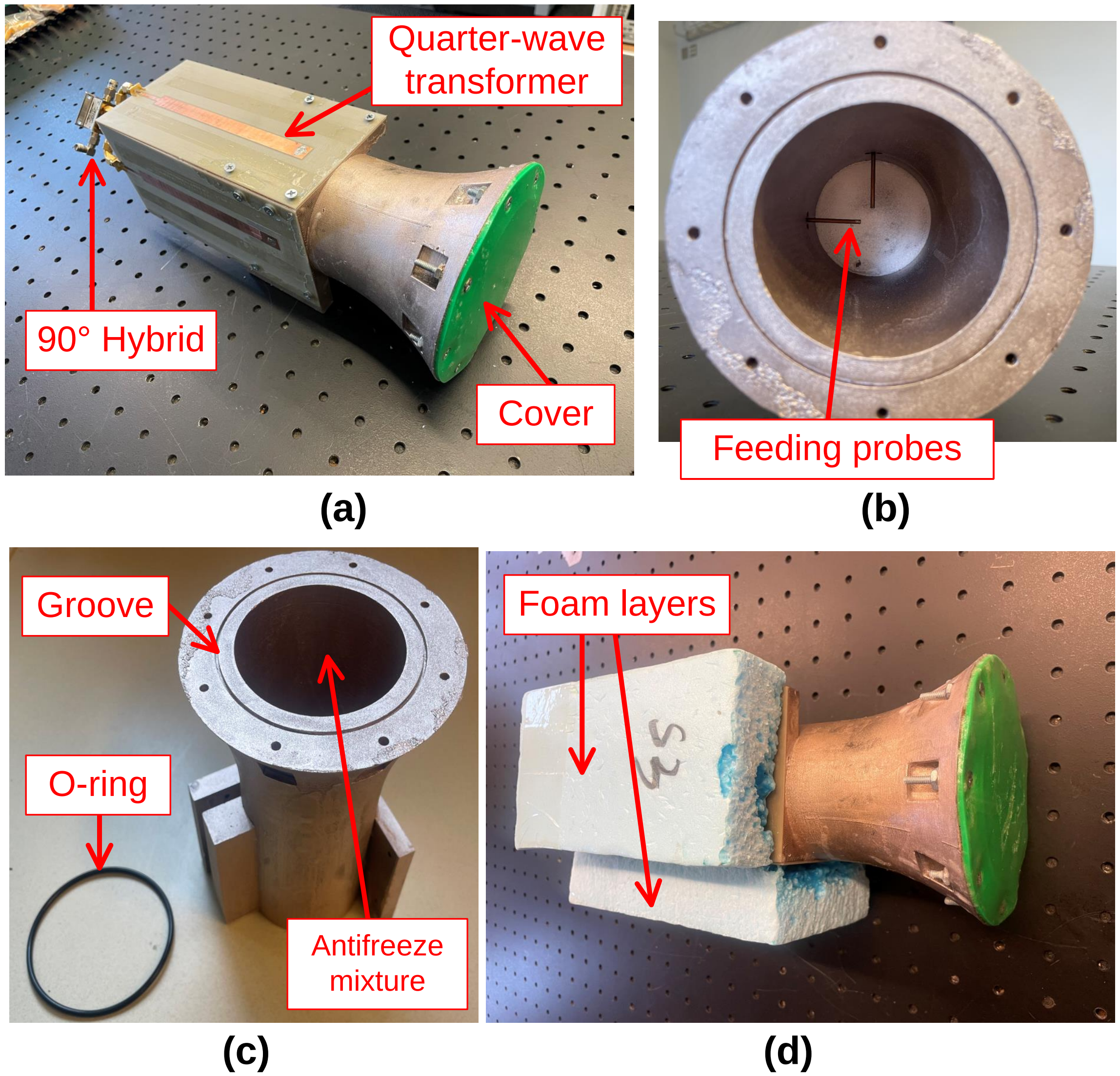

Figure 2.14: (a) The prototype antenna. (b) Perpendicular feeding probes inside the antenna. (c) The manufactured antenna with protective foam layers. (d) Groove on the antenna flange and O-ring to prevent liquid mixture leakage.

probes made of copper, which are perpendicular to each other. The signals from the two probes are linearly polarized and have a 90° phase shift between them, forming a circularly polarized signal at the output. To prevent the leakage of water/antifreeze mixture through the feeding points, waterproof glue is used to cover the feed point holes. After adding the liquid mixture to the waveguide, an

O-ring was positioned in the groove of the waveguide flange, as shown in Fig. 2.14c, and a cover was subsequently placed over it. Bolts and nuts were then used to secure the cover, ensuring it was pressed firmly against the waveguide opening to maintain a watertight seal. The antennas are tested in a pool filled with seawater (Fig. 2.15), and approximately 15.5 grams of sea salt per liter is added to the freshwater to achieve a permittivity of $\epsilon_r = 78 - 165j$ at around 300 MHz. Though this measurement has been done at room temperature, to mimic the deep-sea environment with roughly $0°$C temperature, we dissolved enough sea salt in the freshwater so that its permittivity becomes equivalent to that of deep-sea water. We also placed our antennas inside thin plastic bags to protect the RF cables used for this test from harmful saltwater. When the waveguide antenna is submerged in the water, the pressure pushes the plastic bag against it, effectively surrounding the antenna with seawater. To avoid the impact of the surrounding medium on the behavior of the matching PCBs, a layer of protective foam is attached to them, creating an air gap above it, as illustrated in Fig. 2.14d.

Figure 2.15 shows the scattering parameter measurement setup. The Agilent 8720ES Vector Network Analyzer (VNA), equipped with a power amplifier (PA) and a low-noise amplifier (LNA), is used for this measurement to enhance the transmission signal in the lossy seawater environment. Figure 2.16a shows the measured reflection coefficients of the four ports of the antenna system shown in Fig. 2.12. It is evident that all the antennas are well-matched at 300 MHz and follow a similar pattern, although they provide a narrow bandwidth. Adding a $90°$ hybrid (Mini-Circuits ZX10Q-2-3-S+) to the input ports of each antenna (see Fig. 2.14a) helps to provide a broadband matching over the $200 - 500$ MHz band. When the signal is fed from the input port of the hybrid, the reflected signals from the output ($0°$) and coupling ($90°$) ports of the hybrid experience a $180°$ phase difference when they return to the hybrid's input port, effectively canceling each other out and leading to broadband matching [141]. Figure 2.15b shows the antennas' simulated and experimental voltage standing wave ratios (VSWR) in the presence of the hybrid. All values are well below 2 over the shown frequency range ($200 - 500$ MHz), indicating good impedance matching at the antenna input ports with the presence of $90°$ hybrid.

The next step is measuring the transmission coefficient when two antennas are facing each other and are manually placed at different distances. Figure 2.16c and d show the simulated and measured transmission coefficients of the two antennas at 5 cm and 10 cm distances, respectively. In the measurement setup, the VNA, PA (Gain: 22 dB, P_{sat} : 23 dBm), and LNA (Gain: 46 dB,

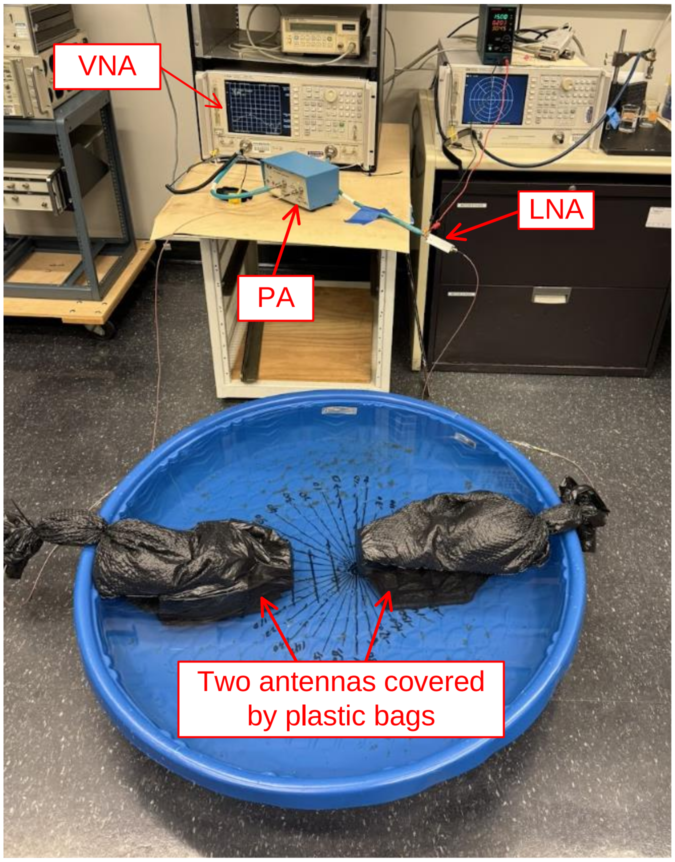

Figure 2.15: The setup to measure S-parameters.

NF: 8 dB) are each calibrated separately, and through a de-embedding process, the final measured transmission coefficient of the antenna system is obtained. Due to the use of the 90° hybrid [141], the antenna system experimentally demonstrates a broad 6−dB transmission bandwidth of 155 MHz (290 − 445 MHz) at 5 cm distance and 75 MHz (285 − 360 MHz) at 10 cm distance. Additionally, the lowest modes of the circular loaded waveguide and their cut-off frequencies are TE_{11} ($f_{\mathrm{cut}} = 273$ MHz), TM_{01} ($f_{\mathrm{cut}} = 357$ MHz), and TE_{21} ($f_{\mathrm{cut}} = 453$ MHz). Even though mode TM_{01} exists in the operational frequency range, it cannot be excited due to the form of the electric field distribution of this mode inside the loaded waveguide. The two internal boundary conditions imposed by the perpendicular feeding probes (shown in Fig. 2.14b) always provide the condition that this mode cannot exist in the short length of the loaded waveguide. Therefore, the antenna

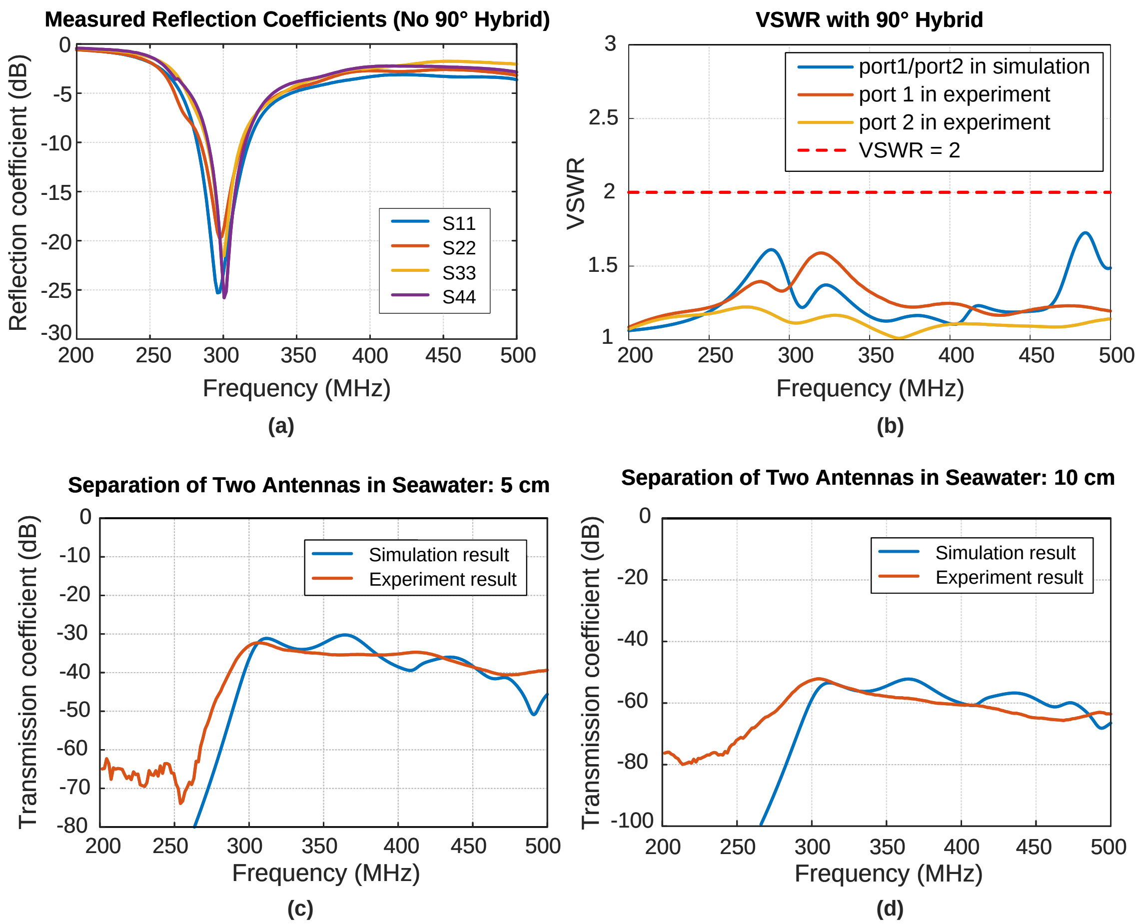

Figure 2.16: (a) Measured reflection coefficient of each port without $90°$ hybrid. (b) Simulated and measured VSWR using $90°$ hybrid. (c) Simulated and experimental transmission coefficient when two antennas are separated by (c) 5 cm and (d) 10 cm placed in seawater.

transmission bandwidth will only contain TE_{11}, which ensures the data quality of the communication link. Furthermore, the antenna's broad bandwidth provides excellent data transmission rates between the AUV and the docking station. The dominant mode of the circular waveguide is TE_{11}, and the next mode is TE_{21}. Based on (2.5), the frequency range of the two lowest modes of the circular waveguide is from 300 MHz to 624 MHz. Therefore, the 150 MHz transmission bandwidth will only contain TE_{11}, which ensures the data quality of the communication link. Furthermore, the 150 MHz bandwidth provides excellent data transmission rates between the AUV and the docking

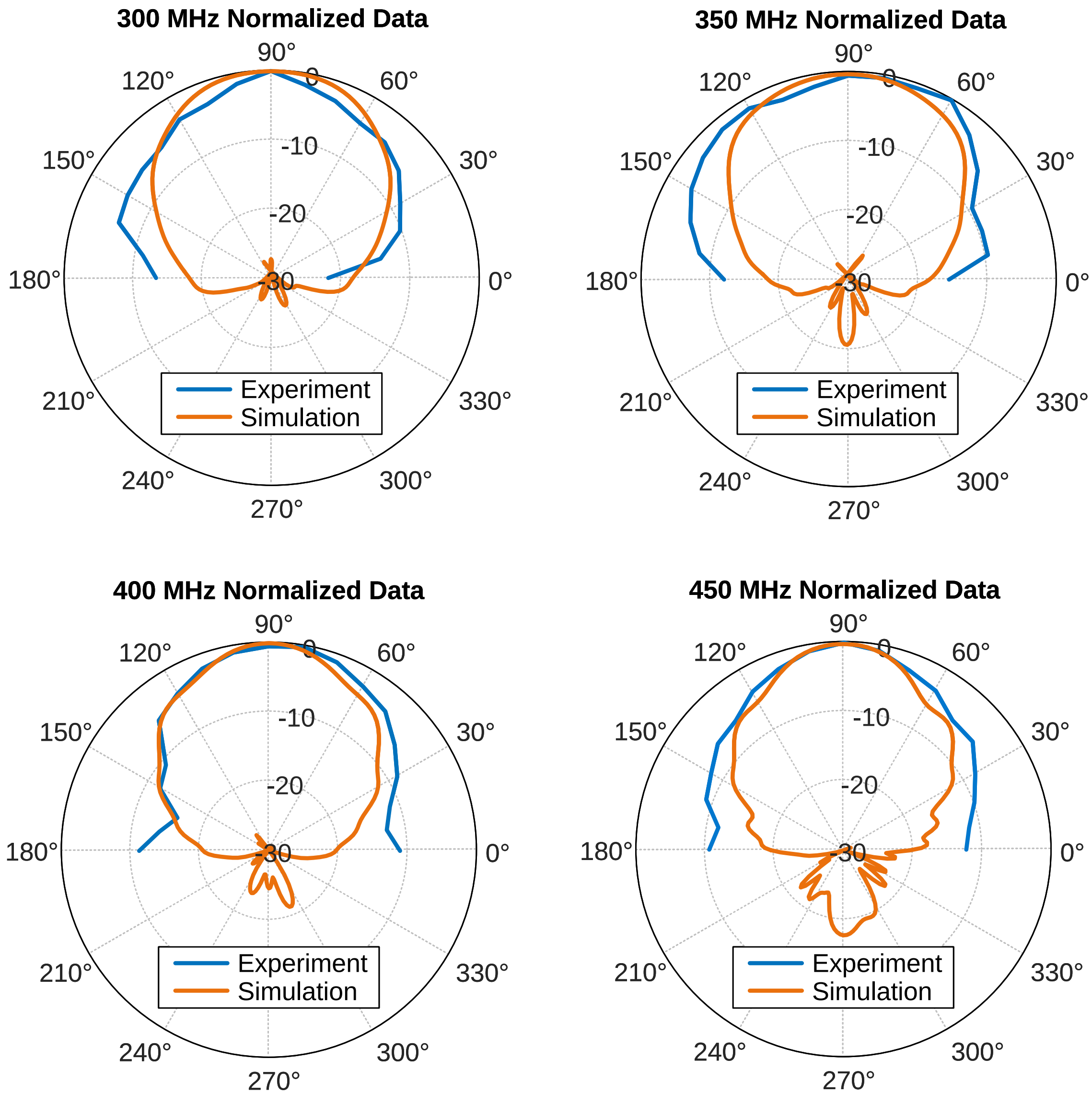

Figure 2.17: Simulated and experimental radiation patterns.

station. Additionally, using a better PA and LNA allows for longer data links.

The radiation and polarization patterns of antennas play a crucial role in data transmission between AUVs and docking stations. In the deep sea, factors such as darkness, floating debris, and current flow make it difficult to precisely control the rotation and alignment of AUVs as they approach docking stations. As a result, using antennas with broad radiation patterns and circular

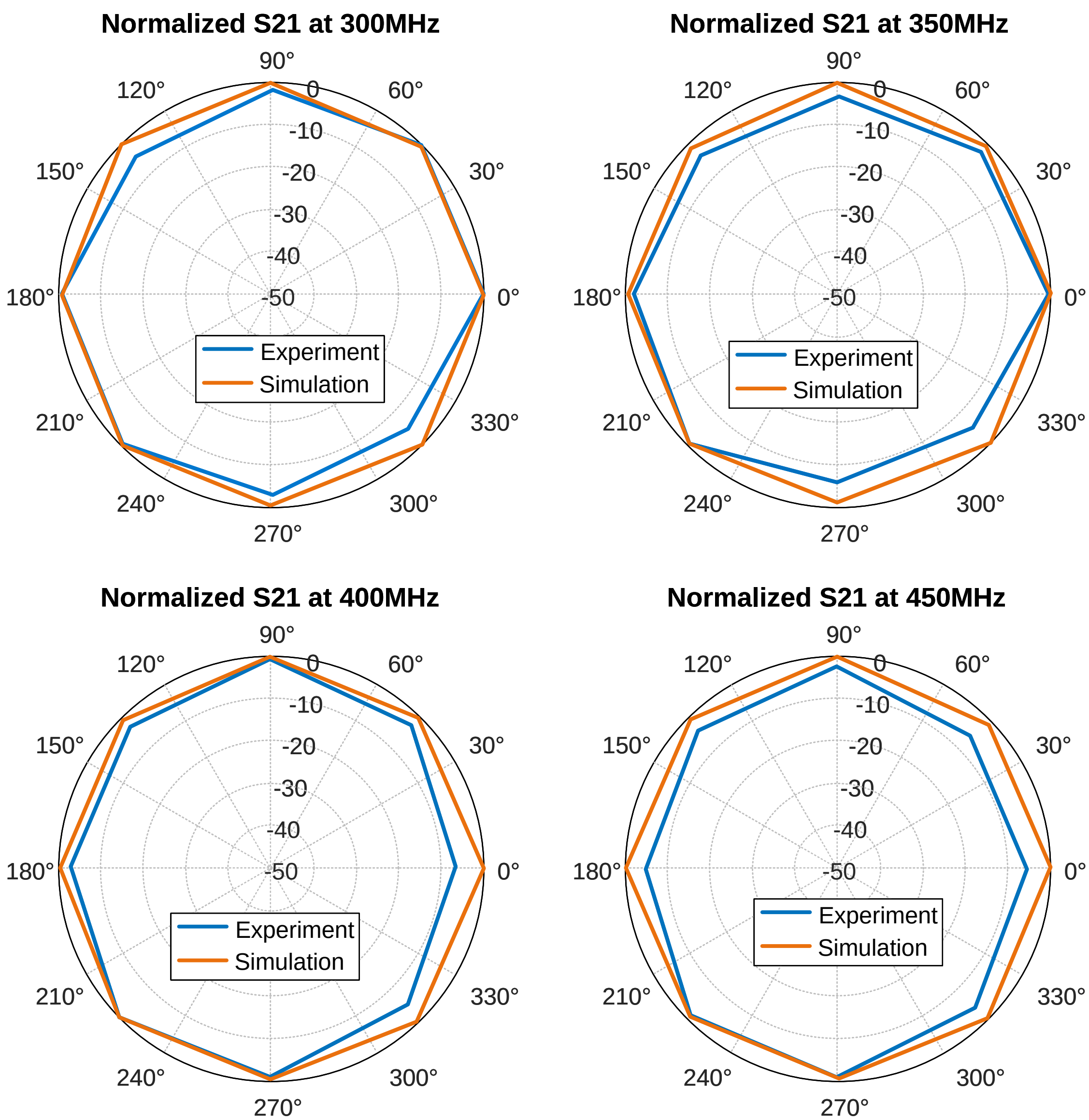

Figure 2.18: Simulated and experimental polarization patterns.

polarization can enhance AUV operations and improve the reliability of establishing a successful communication link between AUVs and docking stations. For example, as shown in Fig. 2.11a, when the DP enters the docking station from above, the transmitter antenna can effectively exchange data with the docking station even if it oscillates slightly along the cable due to current flow. Figure 2.17

Table 2.2: Comparison Table

Reference	Antenna	Frequency	Coverage	Distance	Data rate	Polarization	Dimension
This work	OLSFS	2.3–2.6 GHz	360°	2–3 cm(a)	30 Mbps(a)	Linear	1800 cm^3
This work	Loaded waveguide	290–445 MHz(b)	>60°	>10 cm(a)	10 Mbps(c)	Circular	610 cm^3
[124]	N/A	2.4 GHz	360°	5 cm	3.1 Mbps	N/A	N/A
[39]	Bow-Tie	2.4 & 5.1 GHz	N/A	15.2 cm(d)	N/A	Linear	4200 cm^3
[37]	Magnetoelectric	22.2 kHz	360°	2.2 m	2 Kbps	Linear	69 cm^3
[128]	Dipole	10–80 MHz	360°	7 m(e)	N/A	Linear	47.5 cm(g)
[129]	Loop	50 MHz	>60°	N/A	N/A	Linear	1600 cm^2(g)
[130]	Helical	433 MHz	30°	N/A	N/A	Circular	662 cm^3
[131]	Bow-Tie	433 MHz	360°	5 m(f)	25 Kbps	Linear	193.2 cm^2(g)
[132]	Patch	500 MHz	360°	N/A	N/A	Linear	2400 cm^3

(a) Verified experimentally for seawater medium.
(b) At 5 cm distance in seawater.
(c) Limited by PLUTO SDR, not the antenna system.
(d) An unstable signal was reported for this distance in seawater.
(e) Analytical achievement in freshwater at 25 MHz.
(f) Experimental achievement in freshwater.
(g) Linear or planar antenna without a supporting structure.

illustrates the simulated and measured radiation patterns of the loaded waveguide antenna systems at frequencies of 300 MHz, 350 MHz, 400 MHz, and 450 MHz, when the antennas are located in freshwater. For this test, freshwater is used instead of seawater. This exchange does not affect the measured pattern shapes and only provides a larger dynamic range for plotting better patterns. The antenna has a broad radiation pattern, which enables the transmitter on the AUV to operate without requiring perfect alignment with the receiver antenna at the docking station. The signal can be effectively received within at least $60°$ angular range ($60°$–$120°$), providing flexibility in the alignment between the two antennas. Moreover, Fig. 2.18 shows the polarization pattern of the antenna, indicating that the signal transmission does not vary significantly when one antenna rotates while the other remains fixed. Since both the antennas on the AUV and the docking station transmit and receive circularly polarized signals, the AUV can rotate freely while approaching the docking station. This ensures continuous data exchange between the antennas, regardless of their orientation. These characteristics of the loaded waveguide antennas provide greater freedom during the docking procedure, which helps improve the docking success rate.

In addition to the transmission coefficient and bandwidth analysis, group delays and eye diagrams are also generated to show that the two antennas can effectively transmit signals through seawater with minimal distortion. The group delays shown in Fig. 2.19a are derived from the phase of the measured transmission coefficient and indicate that the group delays do not change much in the antenna system operation range, which minimizes signal distortion due to dispersion. Figure 2.19b illustrates the measurement setup used to generate the eye diagrams. The transmitter and receiver antennas are placed in seawater with varying separations. A PLUTO software-defined radio (SDR) is used to transmit a data sequence through the transmitter antenna, while the receiver antenna receives the data and records it on an oscilloscope. The same PA and LNA are used on the transmitter and receiver sides, respectively, to enhance signal strength. The received data can be further processed to produce the diagrams shown in Fig. 2.19c and d, where "the clear eyes" indicate minimal distortion and good signal quality. In this case, the 10 Mbps data limit is imposed by the SDR modules; however, using more advanced SDRs can deliver faster data links.

2.9 *Summary*

This paper presents two innovative antenna systems specifically designed to improve the reliability and efficiency of autonomous underwater vehicle (AUV) docking operations through enhanced radio frequency communication capabilities. The first system, a 2.4 GHz out-of-line series feed slot (OLSFS) antenna, was developed to address the challenge of short-range data transfer. By conforming the antenna to the cylindrical surfaces of both the docking station and the AUV and employing a horizontal slot array with omnidirectional radiation patterns, the design eliminates the need for precise angular alignment. Simulations and experimental validations demonstrate consistent performance and robust signal transfer within a 2–3 cm range, even under extreme underwater pressure and temperature conditions. This system has been successfully deployed in the Deep Profiler (DP) and docking infrastructure as part of the Ocean Observatories Initiative, contributing to reliable real-world operation.

To further alleviate docking constraints and extend the communication range, a second system was introduced: a compact, circularly polarized loaded waveguide antenna operating in the lower UHF band. By loading the waveguide with a high-permittivity dielectric mixture that mimics the pressure and temperature behavior of seawater, the antenna achieves decimeter-range communication with improved tolerance to rotational misalignment. Simulations and measurements confirm the antenna's broad beamwidth, circular polarization, and bandwidth from 290 MHz to 445 MHz, making it suitable for dynamic underwater conditions. Group delay and eye diagram analyses further validate the antenna's ability to transmit data reliably with minimal signal distortion, and the system achieved up to 10 Mbps data rates—limited only by the SDR hardware used in testing.

These proposed antenna systems significantly improve data transmission reliability by addressing key challenges such as limited communication range, orientation sensitivity, and harsh underwater environments. As summarized in Table 2.2, both antennas outperform many existing designs in terms of size, polarization, coverage, and data rate. Their compact and mechanically resilient constructions demonstrate the feasibility of embedding high-performance antennas into AUVs and docking stations without compromising structural integrity. Importantly, the combination of circular polarization, broad radiation patterns, and high data throughput provides AUVs with more flexibility during docking, ultimately increasing the success rate of underwater missions.

Beyond their immediate utility, these works serve as a call to action for antenna designers to focus on the unique constraints and opportunities presented by underwater environments. By introducing novel structural and material strategies for antenna miniaturization, protection, and performance optimization, this research opens new pathways for solving one of the most persistent and technically challenging problems in underwater robotics. Advancements such as these not only improve AUV operation but also contribute to the broader goal of accelerating autonomous ocean exploration and data collection.

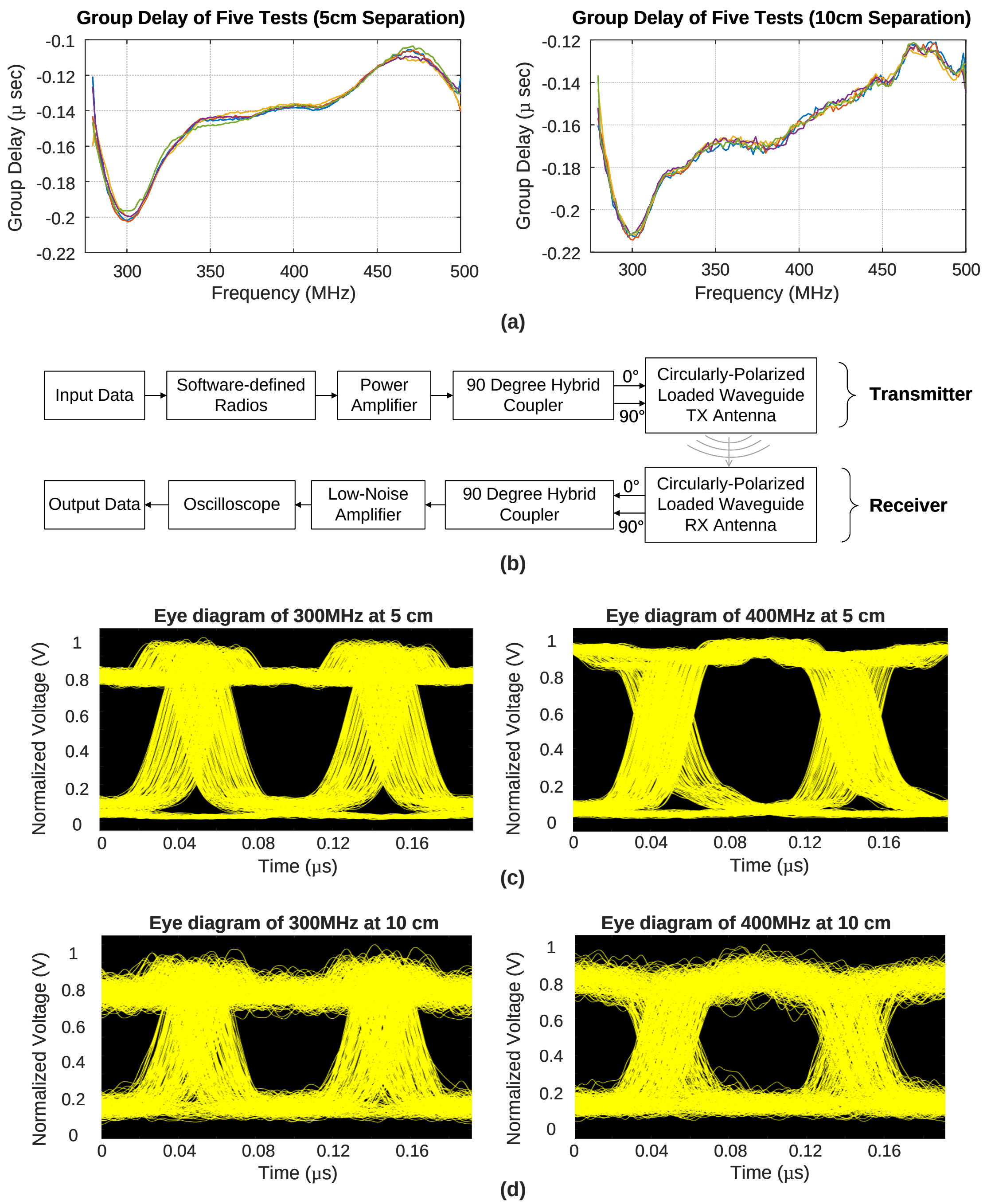

Figure 2.19: (a) Measured group delay of the antenna system in seawater with 5 cm and 10 cm separations. (b) Block diagram of the experimental setup to measure eye diagram. Eye diagram for (c) 5 cm separation and (d) 10 cm separation.

Chapter 3

RF SYSTEMS FOR THROUGH-ICE COMMUNICATION IN POLAR REGIONS

3.1 *Motivation*

Polar regions exert an outsized influence on global climate, ocean circulation, and ecosystem health, yet they remain some of the most under-instrumented environments on Earth. Thick, seasonal sea ice and the harsh conditions below—sub-zero temperatures, strong salinity gradients, and irregular ice morphology—severely impede continuous data collection. Critical variables such as under-ice currents, temperature stratification, and biological activity are essential for improving climate models and informing resource management, but today's sensing platforms must typically surface to transmit data, precluding real-time monitoring and adaptive mission control.

Conventional underwater communications—acoustic and optical—fall short in this context. Acoustic links suffer multipath scattering and absorption in heterogeneous ice layers, resulting in low bandwidth and unpredictable latency. Optical systems achieve high throughput but demand clear line-of-sight and are rapidly degraded by particulate and air-bubble inclusions in the ice. Tethered cables provide reliable connectivity but at the cost of mobility, deployment complexity, and risk of entanglement.

Radio-frequency (RF) propagation through ice offers a promising middle path: at frequencies below a few hundred megahertz, electromagnetic waves can penetrate saline ice with manageable attenuation, enabling modest but sufficient data rates for telemetry, command uplink, and real-time status updates. An RF-based link can support bidirectional communication between under-ice platforms (e.g., gliders, ice-tethered profilers) and surface or subsurface relay nodes, unlocking persistent networks that operate continuously beneath the ice cover.

To realize this potential, Chapter 3 is devoted to the design and optimization of a low-frequency, dielectric-matched antenna system specifically tailored for through-ice communication. We develop a compact radiator optimized for propagation through saline ice by integrating a multilayer dielectric matching network with an impedance-tuned radiating element. Operating near $400\ MHz$ balances penetration depth and antenna size, while the matching layers minimize reflections at the ice interface. Detailed electromagnetic simulations inform the geometry and material selection, ensuring consistent performance across temperature and salinity variations typical of polar environments.

This focused antenna solution addresses the dual challenges of ice attenuation and interface mismatch, laying the groundwork for reliable, real-time RF links beneath polar ice covers. The following sections present the design methodology, simulation results, and prototype measurements that demonstrate the feasibility of through-ice RF communication.

3.2 *Introduction*

Polar oceans and their surrounding regions play an essential and multifaceted role in the Earth system, influencing global climate, ecosystems, sea levels, weather patterns, and sustainability efforts [142, 143]. First and foremost, the polar regions are critical drivers of global climate dynamics [144]. Through the albedo effect, snow and ice reflect solar radiation back into space, helping to stabilize the planet's energy balance. However, as these surfaces melt, darker ocean water and land are exposed, absorbing more heat and triggering a positive feedback known as the ice-albedo effect. This phenomenon accelerates regional warming and contributes to Arctic Amplification—where the Arctic has warmed nearly four times faster than the global average in recent decades [143].

Second, the polar ice sheets, particularly those in Greenland and Antarctica, act as massive freshwater reservoirs. Their ongoing melt is a major contributor to global sea-level rise. Recent research estimates that the Greenland Ice Sheet alone is committed to at least $274 \pm 68, \mathrm{mm}$ of sea-level rise due to its current climatic disequilibrium, with projected contributions ranging from 5 to 33 cm by 2100 depending on emissions scenarios [145, 146].

Third, despite extreme environmental conditions, polar regions host rich and unique ecosystems. For instance, Antarctic krill are a keystone species in the Southern Ocean. Not only are they a fundamental food source for a wide range of marine animals, but they also play a significant role in carbon sequestration. By producing fast-sinking fecal pellets, krill help transport carbon to the deep ocean, effectively sequestering amounts of carbon comparable to those captured by blue carbon ecosystems like mangroves and seagrasses [147].

Fourth, the rapid environmental changes occurring in the Arctic have far-reaching impacts on atmospheric circulation and weather patterns in lower latitudes [148]. As the Arctic warms, the temperature contrast between the equator and the pole weakens, resulting in a less stable and more meandering jet stream. This disruption can lead to persistent and extreme weather events—such as prolonged cold spells, heatwaves, and heavy rainfall—particularly across North America, Europe, and Asia. These effects are most pronounced during winter but can extend into summer via mechanisms like quasi-resonant amplification of planetary waves. Additionally, the stratosphere and a weakened polar vortex may further amplify these mid-latitude anomalies. Nonetheless, the precise nature of these linkages remains an area of active research, as they are modulated by various factors including tropical influences, internal variability, and broader climate oscillations such as the Pacific Decadal Oscillation and Atlantic Multidecadal Oscillation.

Fifth, polar regions also serve as invaluable natural laboratories for advancing climate science. The Multidisciplinary Drifting Observatory for the Study of Arctic Climate (MOSAiC) expedition—a major international collaboration involving over 600 scientists from 20 countries—has generated an unprecedented volume of data on Arctic climate dynamics. This comprehensive dataset is already enhancing global climate models and improving our ability to predict future climate behavior [149].

Finally, environmental transformations in the polar regions have profound implications for global sustainability [150]. Polar regions are closely linked to the success of Sustainable Development Goals (SDGs), especially those concerning climate action, water security, biodiversity conservation, and international partnerships. Yet, despite their significance, these regions are often marginalized in current sustainability frameworks. Their rapidly changing cryosphere—marked by melting ice sheets, thawing permafrost, and shifting hydrological cycles—poses cascading risks that threaten the stability of ecosystems, global coastlines, and the climate system at large. Recent scholarship emphasizes the urgent need to integrate polar considerations into SDG planning through dedicated targets and indicators, while also promoting transnational cooperation and incorporating Indigenous knowledge to support inclusive and resilient sustainability strategies. However, a significant and persistent gap exists in the ocean observing system within polar regions compared to other parts of the world, and this insufficiency has far-reaching implications for a variety of essential applications. The limited availability of high-quality, continuous oceanographic data in these regions undermines the accuracy and effectiveness of critical systems, including numerical weather prediction, seasonal and climate forecasts, aquaculture planning, marine resource management, and broader environmental monitoring and policy-making [41]. Given the accelerating pace of climate change in the Arctic and Antarctic, the need for improved observational capabilities in these regions is becoming increasingly urgent. One of the principal challenges that hinders ocean observation in the polar regions is the pervasive presence of sea ice. Sea ice acts as a dynamic and complex barrier that disrupts the direct exchange of energy, heat, moisture, and gases between the ocean and the atmosphere or space [42]. This interference complicates both surface-based and satellite remote sensing efforts, particularly during the polar night or during melt seasons when the surface conditions become highly variable. Moreover, the physical structure of sea ice—with its rough undersurface, variable thickness, and widespread coverage—makes it difficult to maintain long-term, stable deployments of observational platforms, leading to severe gaps in spatial and temporal data coverage. As a consequence, the quality and completeness of ocean data from the polar regions are significantly lower than those from mid- and low-latitude oceans. This data sparsity directly affects the initialization and performance of coupled atmosphere-ocean models, ultimately degrading the reliability of forecasts and hindering our ability to understand and predict ongoing changes in the Earth system. Bridging this critical observational gap requires targeted investment in specialized polar-capable instrumentation, enhanced satellite retrieval algorithms, and sustained international collaboration to ensure robust, year-round monitoring of these sensitive and globally influential environments.

For example, Argo profiling floats that constitute the first global array for observing the subsurface ocean cannot surface and transmit data to satellites when there is floating sea ice, which prevents them from providing real-time data [43]. Currently, in the communication link composed of seawater, sea ice, and air, the most popular approach is based on acoustic waves and there are plenty of examples [44, 115, 151, 152]. For instance, in [44], one device called "Under-Water Identification (UWID) Tag" is placed on the bottom surface of floating sea ice and another device called "Lamb Wave Detector Georeferencing Identification Satellite (LDGRIDSAT) Tag" is placed on the top surface of sea ice. UWID tag sends acoustic waves to the LDGRIDSAT tag that then sends the signal to Iridium Satellite System. In [115], acoustic communication is employed between autonomous underwater vehicles (AUVs) and the control ship using WHOI MicroModems; these modems support low-bandwidth, frequency-shift keying signals in the 8–12 kHz range, enabling AUVs to transmit navigation data and mission status back to the ship while also receiving updated commands. The

AUVs additionally interact with a long-baseline (LBL) acoustic network by sending interrogation pings to seafloor-mounted beacons, which respond with distinct frequency-coded signals, allowing real-time position estimation even under drifting Arctic ice.

In addition, the magnetic field has also been utilized in some projects to achieve connection through sea ice floating on water [45]. Two autonomous underwater vehicles, named ENDURANCE and ARTEMIS and developed by Stone Aerospace, operated beneath the ice and transmitted a 3500 Hz vertical magnetic field signal to enable tracking [153, 154]. In [153], the ENDURANCE autonomous underwater vehicle (AUV) was deployed beneath the 4-meter-thick ice cover of West Lake Bonney in Antarctica to autonomously perform 3D water chemistry profiling, bathymetric mapping, and glacier wall imaging. To ensure precise navigation and reliable recovery without GPS or external acoustic arrays, ENDURANCE relied on a combination of a ring-laser gyroscope inertial measurement unit, Doppler velocity log, pressure sensors, and an inverted ultra-short baseline (iUSBL) acoustic beacon system. The iUSBL system allowed ENDURANCE to determine range and bearing relative to a beacon suspended beneath the access hole, enabling it to apply corrections to its dead-reckoned position using a Kalman filter and accurately return to the deployment hole at mission completion.

Additionally, optical wireless communication systems and optical fiber tethers have also been employed for similar sea ice communication scenarios. In [46], a system called Sea Ice Diffusing Optical Communications (SDOC) was proposed to enable high-speed, short-range broadcast communication between swarming autonomous underwater vehicles (AUVs) operating beneath sea ice. In this system, an AUV transmitter (AUV-Tx) directs a narrow laser beam upward toward the sea ice sheet, which—due to internal impurities and snow coverage—acts as a diffusing surface. A portion of the scattered light is reflected back into the water and is received by multiple AUV receivers (AUV-Rxs) positioned nearby. To model this complex scattering process, the authors developed a Seawater–Sea Ice Cascaded Layers (SSCL) model that simulates the optical characteristics of layered seawater, sea ice, and snow. The proposed system achieves broadcast communication rates of up to 100 Mbps over distances of 3 to 3.5 meters, depending on ice thickness and seawater clarity, with bit error rates below 10^{-3} at a transmit power of 100 mW. In another under-ice exploration project [155], an autonomous underwater vehicle (AUV) called Icefin was deployed through a narrow, hot-water-drilled hole in the Antarctic ice shelf as part of NASA's SIMPLE project. To enable real-time control, communication, and safe recovery, Icefin was connected to the surface via a 3.3 mm-diameter Kevlar-reinforced optical fiber tether, which provided both mechanical strength and high-bandwidth data transmission. This lightweight tether minimized disturbance to the vehicle's dynamics while ensuring robust operation in the harsh polar environment. It was critical not only for telemetry and sensor data streaming but also for maintaining a physical link for vehicle retrieval during and after under-ice missions.

Another class of subglacial communication systems, although different from our seawater-based scenario, utilizes radio frequency (RF) signals in the high-frequency (HF) and ultra-high-frequency (UHF) bands to establish wireless links through deep glacial ice. These systems are designed primarily for environments that are not submerged in seawater, and are instead deployed in ice sheets to monitor subglacial processes. In such systems, researchers typically drill boreholes and place wireless transmitters deep within the ice, which then communicate with surface receivers through hundreds to thousands of meters of ice. For example, in the Stone Aerospace VALKYRIE project [156], a radar-equipped cryobot is developed to explore deep ice using SAR imaging and RF communication. The WiSe project [157] demonstrated successful transmission of sensor data through up to 2500 meters of ice, using low-frequency (30 MHz) radio signals and a custom-built data logger. The Glacsweb program [158] embedded wireless sensor nodes within fast-moving glaciers in Norway, using 433 MHz radios to track temperature, pressure, and motion. Similarly, the Cryoegg project [159] used a 169 MHz wireless link to transmit pressure, temperature, and conductivity data through up to 1.3 kilometers of cold ice, with future designs targeting depths of 2.5 km. These systems represent a complementary approach to underwater communication, with a focus on long-range RF transmission in ice rather than acoustic signaling in seawater.

This section presents the development of an RF/microwave antenna system specifically designed to establish reliable communication links beneath sea ice, a notoriously challenging environment for electromagnetic (EM) signal transmission. Sea ice is known to be highly dissipative at microwave frequencies, significantly attenuating signals. However, electromagnetic wave penetration through sea ice remains sufficiently viable at lower frequencies, particularly those below 500 MHz, making them suitable for communication applications in polar environments. One major challenge in designing antennas for such low frequencies is the large physical size required, as antenna dimensions are generally proportional to the wavelength. To address this issue, we leverage materials with a high dielectric constant to reduce the electrical size of the antenna without compromising its performance [47]. Specifically, our proposed antenna system employs a circular waveguide structure filled with these high-permittivity materials, enabling a more compact design that is practical for deployment on autonomous underwater vehicles (AUVs) and other sub-ice platforms. To enhance the efficiency of EM signal transmission through the sea ice, we also incorporate an impedance-matching layer at the interface, which minimizes reflection and maximizes power transfer. Furthermore, the antenna is connected to a flexible, metallic-coated guiding structure filled with silicone oil. This structure serves as a low-loss EM conduit, allowing signals to propagate through the complex ice-water interface with minimal distortion and attenuation. Fig. 1.2 illustrates a conceptual example of how the proposed antenna system can be deployed beneath the ice. The guiding tube is engineered with an adaptable opening designed to conform to the irregular and uneven surface morphology of the sea ice bottom. This ensures a tight fit and stable signal transmission path. Additionally, the guiding structure can be fabricated with lengths of one meter or more, which provides a safe clearance buffer to prevent collisions between AUVs and the undersurface of the sea ice during docking or communication maneuvers. The proposed antenna systems offer several significant advantages that make them well-suited for challenging environments such as underwater or through-ice communication. First, they are capable of transmitting circularly polarized waves, which enhance signal robustness by reducing the effects of multipath fading and polarization mismatch. Second, the use of a high dielectric constant core allows for a more compact antenna design, minimizing the overall footprint without compromising performance. Third, the antennas exhibit a wide operational bandwidth—approximately 10% relative to the center frequency—enabling them to support high data rate transmissions and adapt to varying signal requirements. Fourth, they feature a directional radiation pattern, which improves signal strength and reduces interference by focusing energy in the desired direction. Fifth, the structural design and choice of materials allow the antennas to withstand extreme high-pressure environments, making them suitable for deep-sea applications. Finally, the antenna design is flexible and can be tailored to operate at different frequencies depending on specific mission or environmental requirements.

3.3 *Polar Region Antenna Design Procedure*

The current satellite communication infrastructure encompasses a variety of systems that operate across a broad frequency spectrum. Notably, the Argos system functions at a carrier frequency of 401 MHz, offering a bandwidth of 1.77 MHz and a modest data rate of 400 bps, which is particularly suited for low-data-rate, long-duration environmental monitoring applications. In contrast, the Global Positioning System (GPS) operates at a much higher frequency of 1575.42 MHz and supports a wider bandwidth of 24 MHz, enabling high-precision positioning and navigation capabilities. The Iridium satellite network, widely recognized for its global communication services, operates at 1618 MHz with a bandwidth of 16.5 MHz, facilitating voice and data transmissions over a constellation of low Earth orbit (LEO) satellites. Furthermore, SpaceX's satellite communication link spans from 1610 to 1617.775 MHz for earth-to-space (uplink) communication, and from 2483.5 to 2500 MHz for space-to-earth (downlink) transmissions, showcasing the growing adoption of high-frequency bands for advanced broadband services. Despite the high data throughput offered by systems operating in the L and S bands, such as GPS, Iridium, and SpaceX, they suffer from significant signal attenuation when electromagnetic (EM) waves propagate through lossy or conductive materials, such as sea water or biological tissues. This attenuation becomes more severe as the operating frequency increases, making high-frequency satellite links less suitable for communication through challenging environments like polar sea ice or deep-sea conditions. Consequently, for undersea and through-ice communication applications, the Argos system, which operates near 400 MHz in the VHF/UHF band, presents a favorable trade-off due to its superior signal penetration capabilities at lower frequencies. However, a fundamental challenge arises at these lower frequencies: the physical dimensions of antennas and associated components become large relative to the wavelength, often leading to bulky and impractical device implementations in compact or embedded systems. To address this issue, we propose the use of waveguide antennas loaded with materials exhibiting a high relative permittivity (dielectric constant), denoted as $\epsilon_{\text{r,eff}}$. This loading effectively reduces the guided wavelength to $\lambda_0/\sqrt{\epsilon_{\text{r,eff}}}$, where λ_0 is the free-space wavelength. As a result, the overall size of the antenna structure can be substantially minimized without compromising its performance at the desired operational frequency. For our design, titanium dioxide (TiO_2) is selected as the dielectric loading material due to its exceptionally high effective permittivity, $\epsilon\text{r,eff} = 96$, and its low dielectric loss, characterized by a loss tangent $tan\delta_{\text{eff}} \ll 1$. These properties make TiO_2 an ideal candidate for enhancing the electromagnetic confinement within the waveguide, reducing radiation losses, and achieving compact antenna geometries compatible with underwater deployment. By leveraging such material loading strategies, it becomes feasible to deploy low-frequency antennas with reduced size, improved impedance matching, and enhanced robustness in lossy, high-pressure environments such as deep-sea or polar regions.

As shown in Fig.3.1a, the fundamental radiating element in the proposed communication system is a circular waveguide antenna, which forms the core of the transmission and reception architecture. This type of antenna structure is especially suitable for high-performance RF communication in constrained environments, due to its ability to support well-defined propagation modes and its compatibility with material loading strategies. In the present design, two coaxial connectors are symmetrically inserted perpendicularly into the side walls of the circular waveguide. These connectors serve as the feeding points for exciting the guided modes within the waveguide. To achieve circular polarization—a critical feature for reducing polarization mismatch losses and orientation sensitivity in dynamic environments—the two feed ports are excited with a 90° phase difference. This deliberate phase offset leads to the formation of right-hand or left-hand circularly polarized waves inside the waveguide cavity, which significantly enhances the robustness of the communication link. Circular polarization is particularly beneficial in satellite communication systems, where perfect alignment between the transmitting (TX) and receiving (RX) antennas cannot always be guaranteed due to orbital motion, sea wave disturbances, or mechanical misalignments. By adopting circular polarization, the antenna system becomes less sensitive to the angular misorientation between TX and RX antennas, thereby improving link stability and overall performance. The antenna structure features four key geometric parameters that critically influence its impedance matching and radiation characteristics: the waveguide radius *r*”, the distance from the feed point to the copper back wall *a*”, the insertion depth of the coaxial probe core *h*”, and the extension length of the waveguide cavity beyond the feed points *b*”. Each of these parameters plays a unique role in defining the electromagnetic behavior within the waveguide and must be carefully engineered to achieve optimal antenna performance. The radius “*r*” of the waveguide is fundamentally linked to the cutoff frequency of the dominant TE_{11} mode in a dielectric-loaded circular waveguide. It can be estimated using the expression $r = p'_{11} / \left(2\pi f_{c11}\sqrt{\mu_0\epsilon_0\epsilon_{\text{r,eff}}}\right)$, where p'_{11} is the first root of the derivative of the Bessel function of the first kind (approximately 1.84118), $f_{c_{11}}$ is the cutoff frequency of the TE_{11} mode, and $\epsilon_{\text{r,eff}}$ represents the effective relative permittivity of the dielectric material filling the waveguide. This relationship ensures that the selected dimensions support the desired mode at the operating frequency, while suppressing higher-order modes. The dimension "*a*"—the axial distance from the feed point to the back copper wall—is typically chosen to be approximately one-quarter of the guided wavelength in the loaded medium, i.e., $\lambda_g/\sqrt{\epsilon_{\text{r,eff}}}$, to create an open-circuit (high-impedance) condition at the rear end of the waveguide. This design choice causes the reflected wave at the back wall to constructively interfere at the feed point, thereby directing more power towards the front of the waveguide and enhancing forward radiation. The depth "*h*" of the coaxial probe's inner conductor is another critical tuning parameter. It determines the strength of coupling between the coaxial transmission line and the resonant modes within the waveguide. If the probe is inserted too shallow or too deep, impedance mismatch and poor power transfer can occur. Thus, "*h*" must be optimized to ensure efficient excitation of the desired mode while minimizing return loss. Finally, the waveguide extension "*b*" serves to support and shape the radiated field distribution. It may also assist in impedance matching and radiation pattern control, depending on whether the structure is open-ended, flanged, or connected to additional matching elements. To achieve optimal performance, including desired radiation patterns, high radiation efficiency, and excellent impedance matching across the operating band, all four structural parameters—"*r*", "*a*", "*h*", and "*b*"—are systematically optimized using full-wave electromagnetic simulation tools, specifically Ansys HFSS. The optimization process involves parameter sweeps, modal analysis, and port-based S-parameter evaluations to fine-tune the antenna geometry.

Since the underside of sea ice often exhibits an irregular and rugged topography, it poses a significant risk of physical damage to autonomous underwater vehicles (AUVs) attempting to surface for satellite communication. These jagged and uneven formations can tear or obstruct the sensitive structural components of AUVs, particularly their communication modules and sensors [160, 161]. As a result, current AUV systems, including widely deployed oceanographic platforms such as Argo profiling floats [43], are programmed to avoid surfacing when they detect the presence of overhead sea ice. This limitation introduces a major bottleneck in acquiring real-time oceanographic data from polar regions and restricts the spatial and temporal resolution of satellite-linked observations. To address this critical challenge, a novel communication architecture has been developed that allows

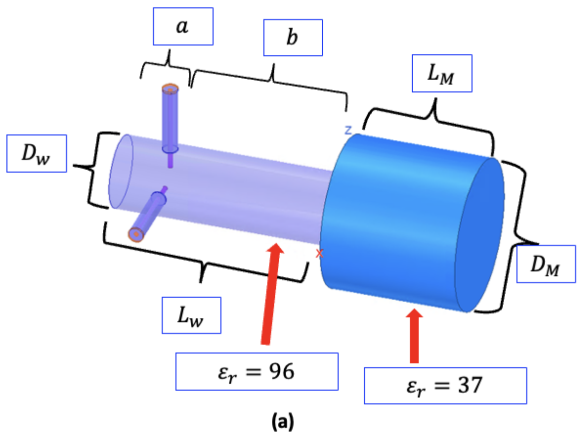

Parameters	Values (mm)
a	33
b	117
D_w	48
L_w	150
L_M	90
D_M	100
L_G	810
D_G	286

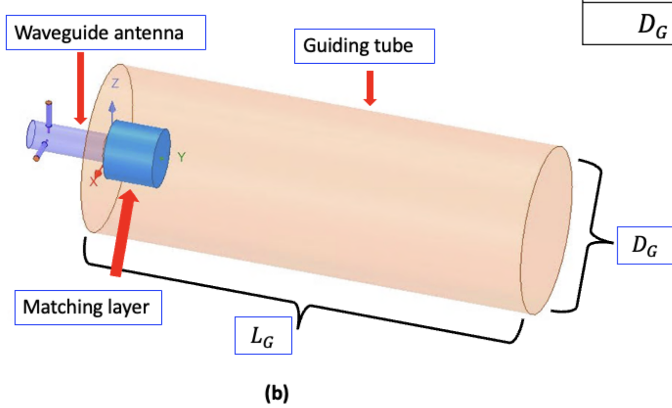

Figure 3.1: (a) Waveguide antenna with matching layer. (b) Waveguide antenna with matching layer and guiding tube.

AUVs to establish a satellite uplink without directly surfacing. As illustrated in Fig.3.1b, a flexible guiding tube is engineered to extend vertically from the AUV toward the bottom of the sea ice. This tube acts as a low-loss conduit for radio frequency (RF) signals, enabling transmission from the submerged AUV to the underside of the ice where satellite communication becomes feasible. The guiding structure essentially functions as a circular waveguide, designed with specific materials and geometries to operate effectively under polar marine conditions. The core of the guiding tube is filled with silicone oil, which serves as the dielectric loading medium. This material is chosen for multiple functional and environmental reasons. First, being a liquid, silicone oil provides exceptional mechanical flexibility, allowing the waveguide to deform or adjust without structural failure when encountering obstacles such as uneven ice surfaces or floating debris. This flexibility is particularly advantageous in dynamic marine environments where rigid structures would be prone to damage or misalignment. The adaptable nature of the silicone oil also allows the waveguide tip to form a conformal and compliant interface with the ice boundary, as depicted in Fig.1.2, facilitating smoother wave transmission. Secondly, the buoyancy characteristics of silicone oil make it well-suited for vertical deployment. Its density is slightly lower than that of seawater at approximately $0°C$, meaning the tube can naturally ascend and maintain its vertical orientation without the need for active propulsion or energy expenditure. This passive alignment not only conserves the AUV's onboard power but also simplifies the deployment mechanism. From an electromagnetic perspective, dielectric matching between the guiding tube and sea ice is a vital design consideration. At the operating frequency of 400 MHz—which was previously selected due to its superior propagation characteristics in lossy media—the effective dielectric constant of silicone oil is approximately $\epsilon_{\text{r,eff}} = 2.7$, and remains stable across temperature variations common in polar waters [162, 163]. According to [164], the effective dielectric constant of first-year and multi-year sea ice is typically around 3. This close permittivity match between silicone oil and sea ice substantially reduces reflection and impedance mismatch at the interface, ensuring more efficient power transfer and minimizing signal loss. The waveguide is further enclosed in a metal-coated layer, forming a proper boundary for supporting the guided mode propagation and preventing unwanted radiation leakage. In summary, the integration of a silicone-oil-filled, metal-coated flexible waveguide provides a robust and energy-efficient solution for enabling satellite communication in ice-covered environments. This innovation not only enhances the autonomy and operational window of AUV systems in polar regions but also offers a scalable approach to improving remote data retrieval in some of the most inaccessible parts of the global ocean.

The significant difference in the effective dielectric constants between the waveguide antenna's loading material and the guiding tube's loading material presents a substantial impedance mismatch that leads to high reflection losses at their interface. Specifically, the waveguide antenna is loaded with titanium dioxide (TiO2), which has an effective dielectric constant of ϵr,eff $= 96$, while the guiding tube is filled with silicone oil, which has a much lower dielectric constant of $\epsilon_{\text{r,eff}} = 2.7$. This large contrast in permittivity causes a discontinuity in the wave impedance at the transition point, resulting in a strong reflection of the propagating electromagnetic wave, thereby degrading the overall transmission efficiency and impairing communication reliability. To mitigate this issue, an intermediate matching layer is introduced between the waveguide antenna and the flexible guiding tube. The purpose of this layer is to gradually transition the wave impedance from the high-permittivity environment of the antenna to the lower-permittivity region of the guiding tube, thereby reducing reflection and maximizing power transfer across the interface. Theoretically, this matching layer operates based on the principle of a quarter-wave transformer, which is a well-established method in microwave engineering for impedance matching between two media. In this configuration, the matching layer is designed to be one-quarter of the guided wavelength in thickness and possess an effective dielectric constant equal to the geometric mean of the dielectric constants of the two adjacent materials. Mathematically, this is given by:

$$\epsilon_{\text{r,match}} = \sqrt{\epsilon_{\text{r,TiO}_2} \cdot \epsilon_{\text{r,silicone oil}}} = \sqrt{96 \times 2.7} \approx 16.07 \tag{3.1}$$

In practice, achieving a perfect dielectric constant of exactly 16.07 is constrained by the availability of materials and the need to ensure mechanical robustness, thermal stability, and low loss tangent across a range of operating conditions. Therefore, using the parametric optimization tools available in Ansys HFSS, a set of candidate materials was evaluated for their suitability as matching media based on both electromagnetic performance and manufacturability. After extensive simulation and material property analysis, barium tetra-titanate ($\text{BaO}_9\text{Ti}4$) was selected as the most viable solution. This ceramic material exhibits a stable effective dielectric constant of ϵr,eff $= 37$, which, although not the exact geometric mean, offers a significant reduction in reflection compared to a direct interface without a matching layer. Furthermore, BaO9Ti4 demonstrates favorable thermal and mechanical characteristics, making it well-suited for operation in harsh environments such as subzero marine conditions. As shown in Fig.3.1a, the matching layer is carefully integrated between the titanium-dioxide-loaded antenna structure and the silicone-oil-filled guiding waveguide. The geometric and material parameters of this configuration are optimized in HFSS to ensure minimal reflection coefficients ($S11$) and maximum transmission efficiency ($S21$) across the designated frequency band centered at 400 MHz. In summary, the introduction of a barium tetra-titanate matching layer is a critical design feature that bridges the large permittivity gap between the two functional components of the antenna system. This layer not only enhances electromagnetic compatibility but also ensures efficient energy transfer and robust system performance under the demanding conditions typical of polar sea-ice operations.

It is important to note that the length of the guiding tube is a critical design parameter that significantly influences the impedance matching and overall radiation performance of the antenna system. The tube length cannot be chosen arbitrarily; improper selection can lead to undesirable impedance mismatches, which manifest as increased reflection coefficients (S_{11}) and reduced power transfer efficiency. This occurs because the guiding tube, being a dielectric-loaded waveguide, introduces a transmission path that behaves as a resonant structure. If the length does not align properly with the guided wavelength inside the tube, standing waves can form, leading to destructive interference and poor coupling between the waveguide antenna and the external medium. For instance, simulation results show that when the guiding tube length is extended to 1300 mm, the reflection coefficient at the operating frequency increases significantly, with S_{11} rising to -3.76 dB. This value indicates a high level of reflected power and poor impedance matching. Conversely, when the length is shortened to 300 mm, the S_{11} value is still suboptimal at -4.62 dB, suggesting that the tube is too short to properly guide the signal or suppress unwanted reflections. These observations emphasize the need to carefully optimize the tube length so that it supports constructive interference and maximizes forward power transmission while minimizing back reflections. In addition to tube length, several other geometric and material-related factors can impact the system's electromagnetic performance. One such factor is the relative alignment between the waveguide antenna and the entrance of the guiding tube. Misalignment can cause mode conversion or leakage at the junction, which may disrupt the field distribution and degrade matching performance. The radius of the guiding tube also plays a crucial role; it affects the cutoff frequency and the supported propagation modes within the waveguide. A radius that is too small may restrict the propagation of the desired TE_{11} mode, while an excessively large radius could allow higher-order modes or increase unwanted dispersion. Furthermore, coating the end of the guiding tube with a conductive layer such as aluminum can significantly influence the reflection characteristics. A metallic coating at the end can serve to reflect or redirect residual electromagnetic energy, potentially assisting in impedance matching or wave shaping, depending on the application. However, if not properly designed, it can also create resonances or abrupt discontinuities that increase losses. Therefore, the decision to apply such a coating must be guided by a detailed electromagnetic simulation and system-level consideration. Overall, the design of the guiding tube—its length, geometry, material properties, and connection strategy—must be holistically optimized using full-wave simulation tools like Ansys HFSS to ensure efficient integration with the waveguide antenna and robust performance in practical deployment scenarios, particularly in the complex and variable conditions beneath sea ice.

Lastly, to provide a comprehensive perspective on the antenna system development, we present several design candidates that were considered throughout the iterative optimization process. Given that the guiding tube is filled with silicone oil—a liquid with good electromagnetic properties but also mechanical constraints—the overall length of the tube must be carefully balanced. While longer tubes may offer better transmission characteristics under ideal electromagnetic conditions, shorter guiding tubes are generally preferable in practice, especially when considering the spatial limitations within the AUV hull and the need to minimize mechanical complexity [165, 166]. Therefore, strategies to enhance power delivery without increasing tube length are of particular interest in this design. One effective approach to improve wave radiation and reduce impedance mismatch is to implement a flaring structure at the end of the waveguide. A flaring—or horn-like expansion—serves to gradually transition the guided wave from the confined waveguide mode into free space or a semi-infinite medium such as sea ice. This transition reduces diffraction and reflection losses at the aperture, thereby enhancing the radiation efficiency and widening the beamwidth of the antenna. The optimal geometry of the flaring structure can be derived using well-established microwave engineering principles. Specifically, the dimension of the flare is determined using the following expression from Pozar's classical formulation [140], as shown in Equation 3.2:

$$B = \frac{1}{2}\left(b + \sqrt{b^2 + 8\lambda R_E}\right) \tag{3.2}$$

Here, b represents the diameter of the waveguide, λ is the operating wavelength within the medium, and R_E denotes the flare length or expansion radius. The resulting opening diameter B is designed to match the outgoing wavefront, thereby ensuring a smoother radiation pattern and minimal reflection at the boundary. This flare geometry not only enhances the directivity and gain of the antenna but also improves the coupling efficiency between the waveguide output and the surrounding medium, such as seawater or sea ice. The effectiveness of the flaring structure is validated through full-wave electromagnetic simulations. As illustrated in Fig.9, the radiated power is evaluated by integrating the Poynting vector over a designated observation surface, represented as the green sheet. The results demonstrate that the addition of a properly designed flare significantly increases the net power radiated into the target medium. A more detailed view of the simulation setup and alternative guiding configurations is provided in Fig.3.2, which showcases variations in guiding tube length, flare dimensions, and interface treatments. To accurately model the electromagnetic interaction with the environment, the complex dielectric constant of seawater—a key parameter affecting both radiation and propagation—is estimated using the Debye relaxation model, with the real and imaginary parts of the permittivity derived from Equations (2.3) and (2.4). These equations account for frequency-dependent dispersion and losses inherent in seawater, enabling precise simulation of wave behavior at 400 MHz. In conclusion, the inclusion of a flaring structure and the evaluation of multiple design candidates demonstrate a systematic approach to antenna design under realistic environmental and mechanical constraints. These enhancements not only ensure robust signal delivery through sea ice but also enable compact integration with AUV platforms operating in extreme polar conditions.

A dielectric waveguide, as illustrated in Fig.3.3, is a promising candidate for guiding electromagnetic signals from the circular waveguide antenna to the sea ice interface. This type of structure typically consists of two concentric cylindrical layers: an inner dielectric core with a relatively high permittivity, and an outer cladding layer with a significantly lower relative dielectric constant. The fundamental operating principle relies on total internal reflection at the boundary between these two layers, which enables efficient confinement of the electromagnetic waves within the high-permittivity core, effectively guiding the signal over a distance with minimal radiation leakage. When the radii

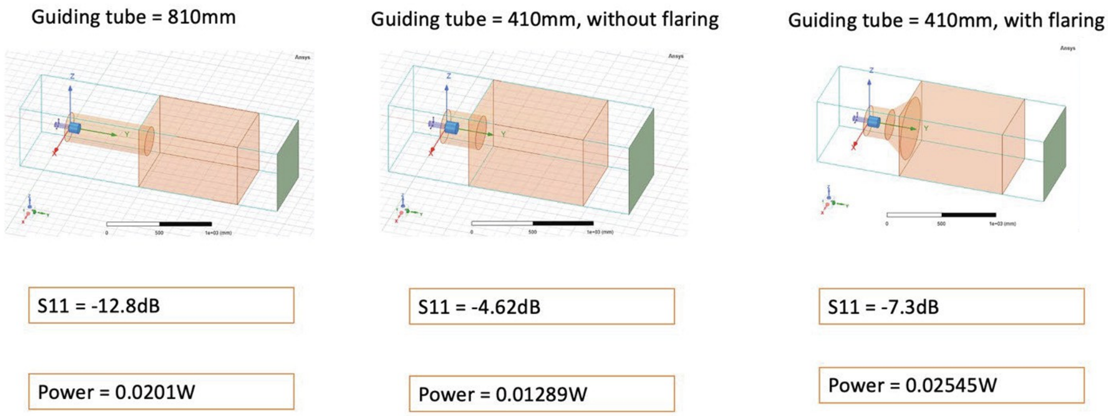

Figure 3.2: Comparison among different guiding structures

of the inner and outer layers are properly optimized, the dielectric waveguide can support modes that maintain a high level of power confinement. Although evanescent fields exist in the low-permittivity cladding region, the majority of the electromagnetic energy remains concentrated within the inner tube, allowing the wave to propagate forward with reduced attenuation. This configuration is conceptually similar to optical fibers used in telecommunications, but scaled and tuned for operation at RF and microwave frequencies. As demonstrated in the simulation results presented in the figure, this dielectric guiding concept was evaluated under both idealized and realistic environmental conditions. When the guiding structure is placed in an air-filled environment, the system performs well, yielding a reflection coefficient S_{11} of less than -10 dB, which indicates excellent impedance matching and minimal power reflection. However, when the same structure is immersed in seawater—a conductive and lossy medium—the system performance degrades significantly. In the seawater-filled case, S_{11} rises to approximately -3 dB, indicating that a considerable portion of the input power is being reflected back into the circular waveguide, primarily due to the strong dielectric contrast and high conductivity of the surrounding medium. To compensate for this, one strategy is to increase the thickness of the outer low-permittivity layer, effectively creating a larger air buffer that insulates the guided wave from the high-loss seawater environment. Simulation results show that increasing the radius of the outer air layer leads to modest improvements in performance: when the outer radius is increased to 250 mm, S_{11} improves slightly to around -3dB; and when further

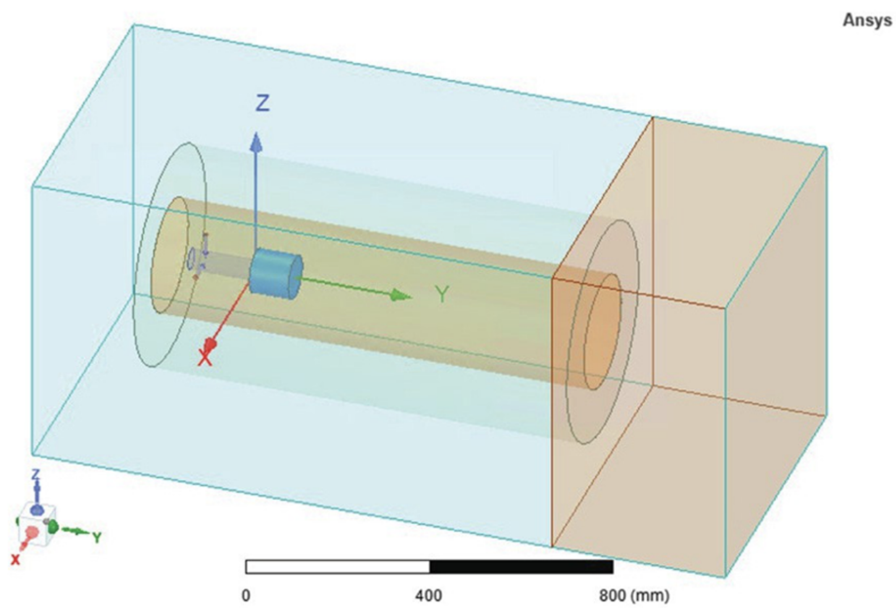

Figure 3.3: Illustration of dielectric guiding tube

increased to 320mm, S_{11} reaches approximately -4.3 dB. However, this approach results in a large and mechanically cumbersome structure, which is not ideal for integration into space-constrained AUV platforms operating in dynamic underwater conditions. In contrast, the proposed guiding tube design—constructed using silicone oil as the dielectric filling and enclosed with a metal-coated surface—achieves superior electromagnetic performance in a much more compact form factor. The total radius of this structure is only about 143 mm, significantly smaller than that required for the air-layer-based dielectric waveguide, while still achieving an S_{11} value below -10 dB under realistic seawater conditions. This performance highlights the advantages of using high-permittivity, low-loss liquid materials in combination with metallic confinement to achieve efficient waveguiding in lossy marine environments. Overall, while dielectric waveguides offer a theoretically attractive solution, their practical implementation in underwater scenarios is limited by size constraints and sensitivity to the surrounding medium. The silicone oil-based guiding tube, with its compact geometry, stable dielectric properties, and strong electromagnetic isolation, presents a more effective and practical solution for RF communication in ice-covered polar regions.

3.4 *Polar Region Antenna Simulation Results*

The simulation first aims to demonstrate the effectiveness of the matching layer through a simple, controlled scenario in which a circular waveguide equipped with a matching layer is immersed in silicone oil. This initial setup isolates the effect of the matching layer and allows us to observe its ability to reduce the reflection coefficient (S_{11}) at the interface between the high-permittivity waveguide material and the lower-permittivity silicone oil. The results confirm that the inclusion of the matching layer significantly improves impedance matching, thereby facilitating more efficient power transfer from the waveguide into the surrounding medium. In the second and third stages of the simulation, the model is expanded to include the complete antenna system, which consists of the circular waveguide, the dielectric matching layer, and the flexible guiding tube. This fully integrated system is then immersed in a more realistic environment filled with seawater, a conductive and lossy medium that introduces significant challenges for radio frequency (RF) signal propagation. The simulations focus on analyzing the system's performance in terms of electromagnetic wave transmission, impedance matching, and field distribution as the signal exits the guiding structure and penetrates the overlying sea ice. In particular, the third simulation scenario incorporates a layer of sea ice above the seawater, further mimicking real-world deployment conditions encountered in polar regions. The study evaluates the impact of the ice layer's thickness and dielectric properties on the transmission performance. By comparing the reflection and transmission characteristics across these three setups, the simulations provide insight into how the antenna system performs under increasingly complex and environmentally realistic conditions. Overall, these simulations validate the design choices—particularly the inclusion of the matching layer and the use of silicone oil as the guiding medium—by demonstrating stable and efficient signal propagation even in the presence of challenging material transitions such as seawater and sea ice.

As previously mentioned, the materials selected for the waveguide and the matching layer play a critical role in achieving optimal impedance matching and efficient signal transmission across interfaces. The circular waveguide is loaded with titanium dioxide (TiO2), which exhibits a high effective relative permittivity of ϵr,eff $= 96$, making it highly suitable for miniaturizing the antenna structure while maintaining strong electromagnetic confinement. The matching layer is composed of barium tetra-titanate (BaO_9Ti4), a ceramic material with an effective relative permittivity of

ϵr,eff $= 37$, chosen to function as a quarter-wave transformer between TiO_2 and the lower-permittivity guiding medium, typically silicone oil. This configuration is specifically engineered to reduce impedance mismatch and minimize reflection at the material interface. The primary physical parameters defining the geometry of the circular waveguide are denoted by a, b, h, and r, where r represents the waveguide radius, a is the distance between the feed point and the back wall, h is the insertion depth of the coaxial probe, and b is the waveguide extension. These parameters determine the resonant behavior and field distribution within the waveguide. The matching layer is characterized by its length (L_M) and diameter (D_M), which govern the effective transformation of impedance and the mode matching across dielectric boundaries. All of these dimensions are initially estimated through analytical calculations—such as cut-off frequency equations and quarter-wave matching conditions—and subsequently fine-tuned using a parameter sweep and optimization workflow in Ansys HFSS, a full-wave electromagnetic simulation software. Fig. 3.4 illustrates the first simulation scenario, where the circular waveguide with the embedded matching layer is immersed in silicone oil to evaluate baseline performance in a lossless and homogeneous dielectric medium. The simulation focuses on the reflection coefficient (S_{11}), which quantifies the amount of power reflected back into the source due to impedance mismatch. A low value of S_{11}, as observed in this setup, indicates strong impedance matching and efficient forward power transmission. The result confirms that the chosen materials and their geometrical configuration work synergistically to minimize the reflection between the high-permittivity waveguide (TiO_2) and the lower-permittivity environment (silicone oil), validating the fundamental premise of the matching layer design. This initial simulation thus serves as a foundational test case, providing confidence in the matching layer's design before deploying the antenna system in more complex and lossy environments such as seawater and sea ice. The favorable S_{11} outcome also establishes the reference performance level against which subsequent simulations involving environmental loading and guiding structures can be compared.

The second scenario is simulated as shown in Fig.3.5a, where the circular waveguide antenna is integrated with the guiding tube via the barium tetra-titanate (BaO_9Ti_4) matching layer. This configuration is intended to replicate the operational environment of an autonomous underwater vehicle (AUV) situated beneath sea ice, where the antenna must establish a communication link by transmitting radio frequency (RF) signals vertically through the ice layer. In this model, the

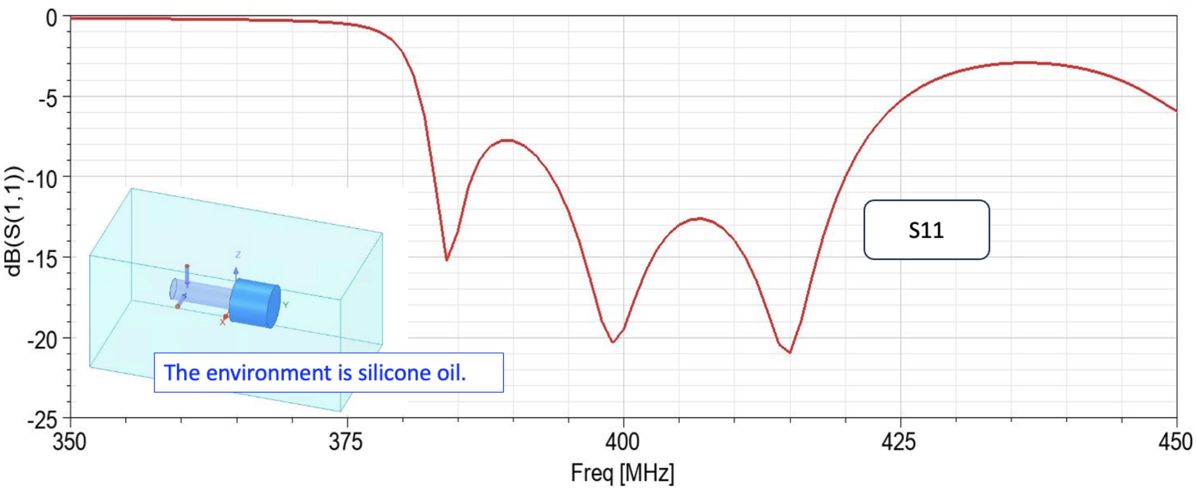

Figure 3.4: S_{11} of waveguide with a matching layer placed in silicone oil.

antenna and waveguide assembly are fully immersed in seawater, a highly conductive and lossy medium that presents considerable challenges for electromagnetic wave propagation. The guiding tube, which is filled with silicone oil and surrounded by a metallic coating, extends upward and makes direct contact with the underside of a 1-meter-thick sea ice layer. As indicated by the red arrows in the figure, the simulation depicts the intended propagation path of the RF signal: from the antenna, through the matching layer and guiding tube, and finally into and across the sea ice. To faithfully emulate real-world conditions, the background material above the sea ice is modeled as air, representing the open atmosphere encountered in polar regions. This multilayer structure—composed of seawater, guiding tube, sea ice, and air—closely approximates the physical and dielectric transitions encountered during actual deployment scenarios. The dielectric constant of seawater used in the simulation is frequency-dependent and computed using the Debye relaxation model, which accounts for both dispersive and conductive properties across the RF spectrum. This model is well-established for accurately characterizing polar liquids and electrolytes at microwave frequencies, and the corresponding values are taken from Ulaby et al. [164]. Similarly, the dielectric constant of sea ice—which varies depending on salinity, temperature, and age (first-year or multi-year)—is also referenced from [164] to ensure consistency and accuracy in the simulation inputs. Fig.

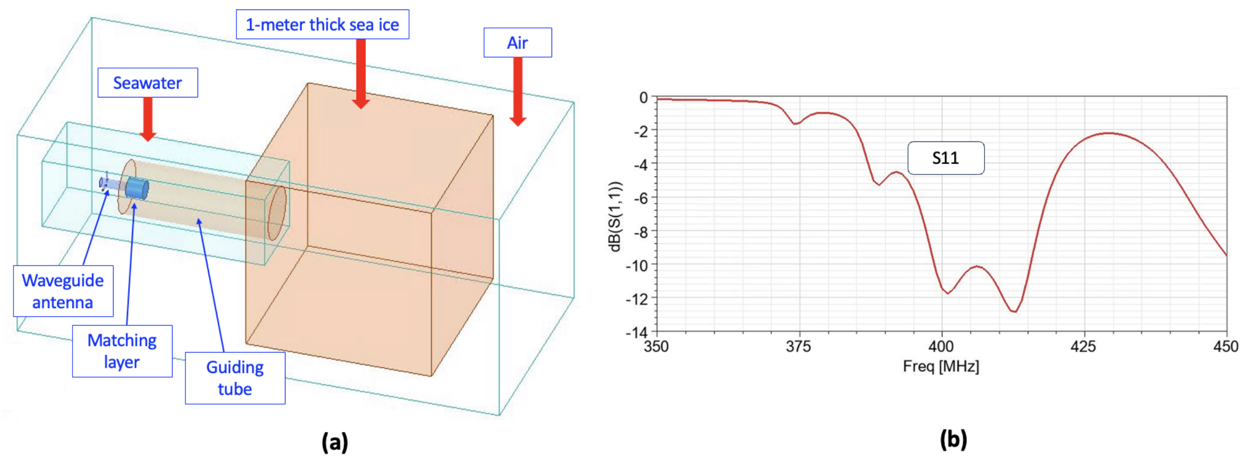

Figure 3.5: (a) Antenna transmit signal in seawater through 1m sea ice. (b) S_{11}.

3.5b shows the reflection coefficient (S_{11}) at 400, MHz for the fully integrated system. The observed value of S_{11} is notably low, which indicates a high degree of impedance matching across the entire signal path. This result confirms that the RF energy is effectively delivered from the antenna into the guiding tube and subsequently coupled into the sea ice with minimal reflection. The simulation thus validates the mechanical and electromagnetic integration of the waveguide, matching layer, and guiding tube, demonstrating their collective ability to support RF transmission through sea ice under realistic environmental conditions. These findings underscore the importance of carefully selecting dielectric materials and optimizing their interface transitions in complex, lossy environments. The second scenario serves as a crucial intermediate step between basic validation (as in Scenario 1) and full-system performance analysis, laying the groundwork for evaluating through-ice propagation and power loss in the subsequent simulation stage.

In the third and most comprehensive scenario of the simulation model, we incorporate a six-layer configuration to thoroughly examine how electromagnetic (EM) waves propagate through a complex sequence of materials representative of a realistic polar deployment. The layers include, in order: the antenna structure, silicone-oil-filled guiding tube, the barium titanate matching layer, seawater, sea ice, and air. This setup allows us to account for the cumulative effects of material boundaries, impedance mismatches, and dielectric losses as the signal transitions from the underwater vehicle environment, through the ice, and into the atmosphere for satellite communication. To quantify the power transmission and attenuation across these interfaces, we compute the power flow on defined surfaces using Ansys HFSS. The total input power is normalized to 1 W, which facilitates straightforward interpretation of power losses throughout the system. By comparing the calculated power across the different material boundaries, we can estimate how much signal attenuation occurs and whether the residual power after transmission is sufficient for reliable satellite uplink. As illustrated in Fig.3.6a, the total power loss measured at the output is approximately 10.2dB. This total loss can be decomposed into three primary components:

- **Reflection loss at the guiding tube–sea ice interface:** 0.28 dB
- **Reflection loss at the sea ice–air interface:** 0.22 dB
- **Propagation loss through 1-meter-thick sea ice:** 5.61 dB

The third term, propagation loss within the sea ice, is of particular importance and can also be estimated analytically by assuming plane wave propagation through a lossy dielectric medium. The decay of the electric field in such a material is governed by the expression:

$$E(z) = E_0 e^{-jk_0 L\sqrt{\epsilon_r(1-j\tan\delta)}} \tag{3.3}$$

where k_0 is the free-space wavenumber, L is the propagation distance, ϵ_r is the real part of the relative permittivity, and $\tan\delta$ is the loss tangent of sea ice. Using dielectric parameters derived from [164], the exponential attenuation term is calculated to be approximately 0.215, implying that over a distance of 1 m, the magnitude of the electric field decreases to about 80% of its original value, and the power decreases to roughly 64%. However, the simulation yields a lower transmitted power fraction of approximately 27.5%, suggesting the presence of additional loss mechanisms not captured by the plane wave model. One primary reason for this discrepancy is the difference in propagation geometry. While the analytical model assumes uniform plane wave behavior, the actual wave emitted from the antenna propagates as a spherical wave, which introduces geometric spreading loss. This loss becomes more pronounced with distance, especially in high-permittivity materials like sea ice, where the wavelength is further reduced. Moreover, Fig.3.6b provides a detailed view of the electric field distribution at the operating frequency of 400MHz. The field is seen to be effectively guided from the antenna through the silicone-oil-filled tube and matching layer, and transitions smoothly into the sea ice. Within the ice, the wave exhibits a spherical propagation pattern, with a visible drop in magnitude as it approaches the upper boundary at the air interface. Together, these results confirm that while there is inevitable signal attenuation due to material losses and spherical spreading, the system remains capable of delivering detectable RF power through 1-meter-thick sea ice. This scenario thus serves as a critical validation of the antenna system's feasibility for through-ice communication in polar regions and highlights the importance of combining simulation and analytical methods for performance evaluation.

Figure 3.7a illustrates the simulation setup designed to evaluate the far-field radiation characteristics of the proposed antenna system as it transmits a signal through a thick sea ice layer. This scenario models a realistic environment where the antenna operates underwater and radiates upward through ice and into the atmosphere, mimicking the physical conditions of satellite uplink in polar regions. The antenna system consists of the circular waveguide, matching layer, and guiding tube, all optimized to achieve efficient impedance matching and signal transmission through lossy dielectric materials. The simulation results are shown in Fig.3.7b and Fig.3.7c, which present the three-dimensional far-field gain pattern and the electric field distribution, respectively. These results offer insight into the angular spread, directionality, and effective radiated power of the system. As the physical dimensions of the sea ice block and the surrounding air box are increased in the simulation domain, the far-field radiation pattern begins to resemble that of an idealized point source, exhibiting symmetric upward radiation with reduced edge diffraction effects. This trend aligns with theoretical expectations, as enlarging the simulation domain reduces the artificial boundary effects imposed by the finite simulation geometry. It is worth noting that the ripples observed in the 3D radiation pattern are attributed to diffraction and scattering at the edges of the truncated sea ice domain used in Ansys HFSS. These artifacts are common in finite-sized simulation environments and can be mitigated by applying absorbing boundary conditions or by extending the domain further, though at the cost of increased computational resources. When considered in conjunction with the near-field electric field distribution, the low S_{11} values at 400 MHz, and the power flow analysis from previous scenarios, the far-field simulation further supports the validity of the antenna system design. These results collectively confirm that the antenna structure is capable of efficiently launching electromag-

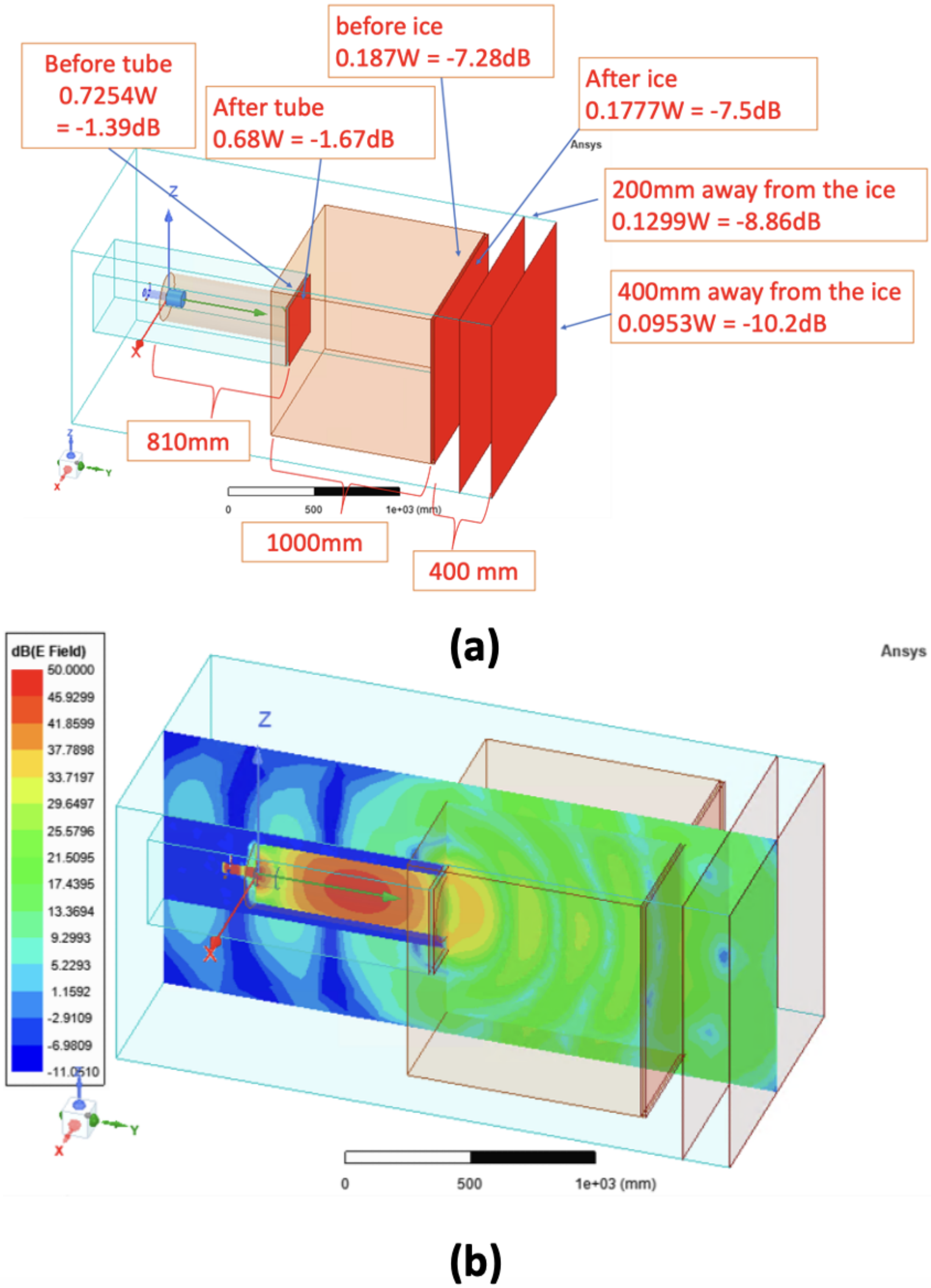

Figure 3.6: (a) power flow simulation of antenna transmitting signal through sea ice. (b) Field distribution of antenna transmitting signal through sea ice.

netic waves through sea ice and radiating into free space with adequate directivity and gain. This demonstrates the system's feasibility for establishing robust satellite communication links in harsh polar environments, where conventional antennas may fail due to ice-induced signal attenuation and alignment challenges.

Experimentally validating the performance of the proposed antenna system presents several engineering and logistical challenges. The complete implementation requires the manufacturing of a high-permittivity titanium dioxide (TiO_2) cylinder with $\epsilon_{\text{r,eff}} = 96$, the fabrication of a matching layer with precise dielectric properties, and the construction of a flexible silicone-oil-filled guiding tube. Furthermore, a large-scale sea ice sample must be produced to accurately emulate the dielectric and thermal characteristics of polar ice in a laboratory environment. Additionally, the entire antenna assembly must be submerged and tested under controlled seawater conditions, which introduces requirements for corrosion resistance, sealing integrity, and precise mechanical alignment. Due to time and resource constraints, we developed an alternative experimental prototype that captures the essential electromagnetic behavior of the full system while being more feasible to fabricate. In this simplified version, the waveguide is dielectrically loaded with pure water, which has an effective relative permittivity of approximately $\epsilon_{\text{r,eff}} = 80$—similar in scale to TiO_2 and suitable for studying high-dielectric loading effects. The prototype structure is fabricated using high-resolution 3D printing, allowing for rapid prototyping and dimensional control. To provide electromagnetic shielding and enable waveguiding, the entire external surface is coated with copper-based conductive spray (from MG Chemicals), effectively transforming the 3D-printed polymer into a functional metallic waveguide. To prevent water leakage and ensure structural stability, a Teflon plate is fixed at the open end of the waveguide. Teflon is chosen due to its chemical resistance and low loss tangent, making it an ideal sealing and dielectric window material. A quarter-wavelength impedance transformer is also integrated into the feed structure to match the antenna input impedance to $50\ \Omega$, improving coupling to standard RF measurement equipment such as vector network analyzers (VNAs). The measurement setup, including the assembled antenna, measured reflection coefficient (S_{11}), and far-field radiation pattern, is presented in Fig. 3.8. The results show that the antenna exhibits good impedance matching, with S_{11} dipping below -10dB near 290MHz. The radiation pattern demonstrates the expected directional behavior, validating the effectiveness of the high-dielectric waveguide design even under simplified conditions. These initial results provide strong

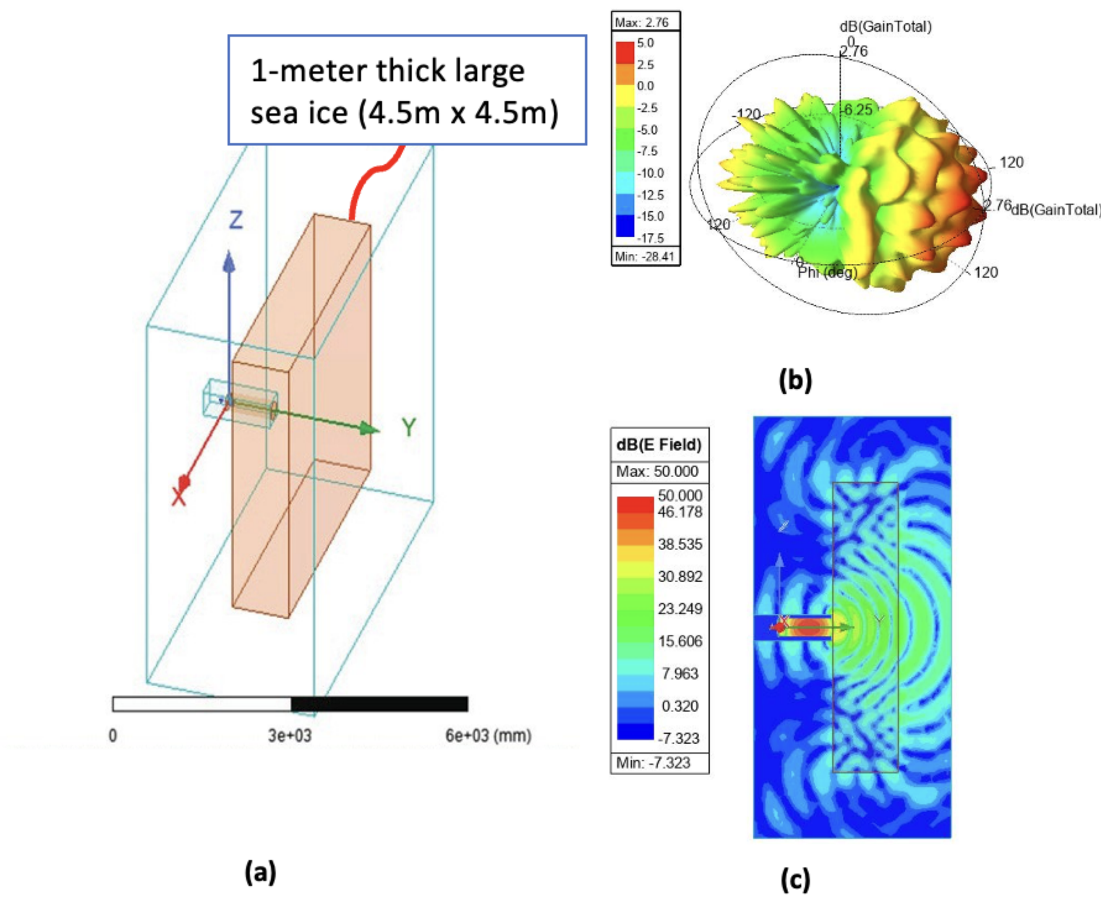

Figure 3.7: (a) Antenna transmit signal through a large sea ice. (b) 3D gain plot. (c) Electric field distribution.

experimental support for the feasibility of the proposed system architecture. The decision to operate the prototype at 290 MHz—rather than the 400 MHz target frequency used in simulations—is based on the integration of two related projects: one focused on undersea RF communication [47], and the other on through-ice signal transmission. By converging these efforts into a single modular test platform, we reduce experimental overhead while maintaining relevance to both application scenarios. In the next phase of experimentation, we plan to construct additional antennas, matching structures, and guiding tubes tailored to the 400 MHz band. These will be tested in a multi-layer environment representing the (seawater)–(sea ice) interface, allowing us to evaluate full-system performance under more realistic conditions. The integration of empirical validation with simulation and analytical modeling will provide comprehensive insight into the viability of this antenna system for satellite uplinks in extreme polar environments.

3.5 *Summary*

This study presents a novel RF antenna system specifically designed for through-ice communication in polar environments, aiming to bridge a critical technological gap in satellite connectivity for autonomous underwater vehicles (AUVs) operating beneath sea ice. The proposed system, composed of a high-dielectric-loaded circular waveguide antenna, an impedance-matching layer, and a silicone-oil-filled guiding tube, is engineered to address the unique electromagnetic propagation challenges posed by the heterogeneous interfaces between seawater, sea ice, and air. Through a series of full-wave simulations using Ansys HFSS, we demonstrated the viability of the antenna system at 400 MHz—compatible with the Argos satellite band—achieving efficient signal transmission with manageable reflection losses and a total power loss of approximately 10.2 dB through a 1-meter-thick sea ice layer. The simulations also confirmed that the designed components maintain good impedance matching and directional radiation patterns, even in complex multilayer environments.

Experimentally, an initial proof-of-concept antenna using a water-loaded waveguide was fabricated and tested, showing promising results at 290 MHz in terms of impedance matching (S11) and radiation characteristics. While this version was constructed from more accessible materials for rapid prototyping, future work will focus on constructing the full TiO_2-BaO_9Ti_4-silicone oil system and validating its performance in controlled seawater–sea ice scenarios. The modular nature

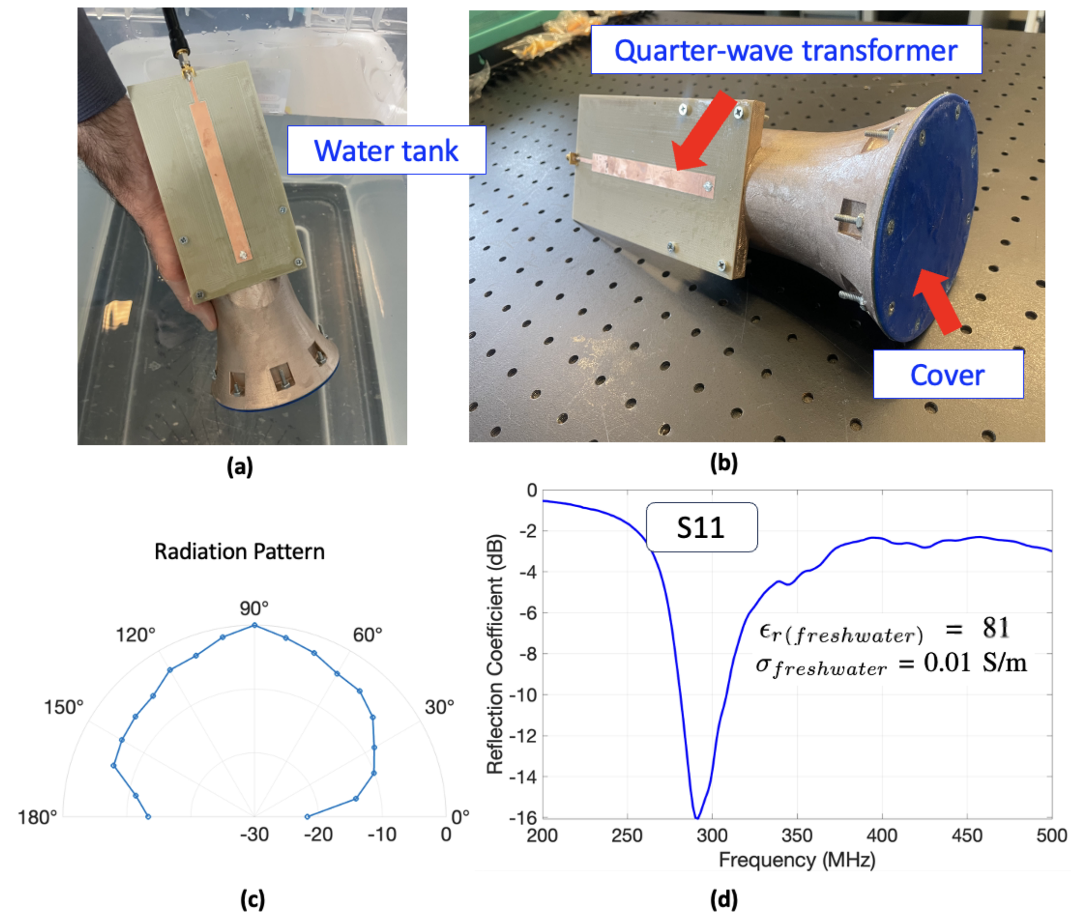

Figure 3.8: (a) Measurement setup. (b) Manufactured antenna. (c) Radiation pattern. (d) S_{11}.

of the design also allows for frequency reconfiguration by adjusting the physical dimensions of the antenna, matching layer, and guiding tube, thus extending its potential for integration with other satellite systems beyond Argos, including Iridium and future low-frequency platforms.

This research lays a foundation for reliable, compact, and power-efficient RF systems that can be deployed on AUVs for real-time data transmission under ice-covered oceans. By enabling persistent satellite communication links from beneath sea ice, the proposed technology holds the potential to significantly enhance ocean observation, improve global climate modeling, and enable a new class of scientific missions in extreme polar environments. Future developments will focus on extending the range of propagation, integrating the system into full-scale AUV platforms, and conducting field tests in Arctic or Antarctic deployments.

Chapter 4

MATERIAL CHARACTERIZATION AT THZ FREQUENCIES FOR THZ ANTENNA DESIGN

4.1 *Motivation*

As THz technology transitions from laboratory curiosity to practical deployment in high-speed wireless communications, medical imaging, security screening, and nondestructive evaluation, designers and engineers confront a persistent obstacle: the absence of a reliable, comprehensive dielectric-constant reference for materials in the THz band.

Chapter 4 addresses this challenge by constructing a unified THz dielectric constant database through two complementary experimental methodologies. First, we perform precision measurements using a Vector Network Analyzer (VNA) equipped with frequency extenders. Our developed algorithm processes the measured S-parameters to derive real and imaginary permittivity values over the 150–220 GHz range, establishing a reliable baseline. Second, we introduce a cost-effective alternative by adapting an FMCW radar system to characterize the same material specimens. The overall concept and initial tests for extracting the radiated spectrogram using the THz FMCW radar chip have been discussed. At this stage of the thesis, we have completed material characterization using the standard VNA method. In future work, we will apply our proposed FMCW radar approach to extract the same material dielectric constants, demonstrating the system's capability to accurately characterize material properties in the THz band with comparable resolution and precision but with a significantly simpler measurement setup.

The integration of these two approaches produces a robust catalog of dielectric constants for various materials at THz frequencies, while also delivering a scalable framework for future additions via low-cost setups. This database will accelerate THz component design, streamline simulation workflows, and lower the barrier to entry for emerging applications in the terahertz domain. The remainder of this chapter details our measurement procedures, algorithmic processing, equipment configurations, and the structure and accessibility of the resulting database.

4.2 *Introduction*

One of the emerging fields is antenna design for THz frequencies, with applications in 6G communication networks [80] and high-resolution imaging radar systems. One of the promising approaches to design complex and low-cost antennas is to use 3D printing technologies, and in order to design antennas using 3D printing material (PLA [86], ABS [87], resin [88]), we need to characterize their properties at THz. Unfortunately, there is limited information available in the literature about the permittivity and loss tangent of these materials. The goal of this research is to create a database for 3D printing materials at the THz band, which will support emerging applications.

THz frequency is situated between infrared radiation and microwave radiation in the electromagnetic spectrum, showcasing potential in various applications. The following paragraphs will discuss different applications that utilize THz frequencies, all of which could be potential customers for THz antenna designs operating at these frequencies.

As the demand for fast information exchange rapidly grows, wireless data rates have doubled approximately every eighteen months over the last three decades, and they are quickly nearing the capacity of wired communication systems [167]. 6G communications that enable higher data exchange rates are becoming increasingly in demand and THz frequencies are expected to meet the requirements for high-speed data exchange in 6G communications [66–68]. THz frequencies are essential for 6G applications due to their vast spectral resources, enabling terabit-per-second data rates [69]. They support energy-efficient beamforming and advanced techniques like Massive MIMO, crucial for overcoming high path losses [168]. THz waves also provide short-range, high-throughput connectivity, ideal for dense urban and indoor environments [70, 71]. Additionally, they facilitate complex modulation schemes, offering both high spectral and power efficiency, ensuring reliable data transmission even in challenging conditions [169].

THz images can be applied to examine the coating integrity and thickness of tablets in pharmaceutical procedures, such as cracks or chemical agglomeration within a core [72]. Compared with other candidates, such as atomic force microscopy, confocal laser microscopy, X-ray photoelectron spectroscopy, electron paramagnetic resonance, Fourier transform infrared spectroscopy, and laser-induced breakdown spectroscopy (LIBS) and scanning thermal microscopy, THz frequencies are not destructive to the tablets and can be implemented for measurements easily [73].

In addition, THz frequency applications hold great promise for noninvasive skin imaging due to their unique ability to probe molecular interactions such as vibrational and librational modes, providing both structural and chemical information [72]. In the cosmetic industry, quantifying the hydration level of the stratum corneum is essential for evaluating the effectiveness of moisturizers, as water content directly affects skin appearance and function [74]. In the medical field, particularly in diagnosing basal cell carcinoma (BCC)—the most common skin cancer in white populations—THz pulse imaging (TPI) offers a coherent, time-gated technique capable of capturing both amplitude and phase information to extract refractive index and absorption properties, and with lateral and axial resolutions of $350\,\mu$m and $40\,\mu$m at 1 THz, TPI can potentially assess tumor margins and depth with high precision, highlighting its value in both cosmetic and clinical applications [72]. In general cancer detection, THz frequency-based imaging also offers several advantages for cancer detection [75, 76, 170]. Its label-free, non-ionizing, and non-invasive technique can detect the form of cancer at an early stage. THz imaging generates contrast based on the higher refractive index, absorption coefficient, and dielectric properties of cancerous tissue compared to normal tissue, primarily due to increased water content and blood supply in cancer-affected areas [75]. THz frequency applications also hold a significant role in the oral health sector. It is hard to discover the tooth decay in the early stage when there are no visual features on the tooth surface by accepted methods such as X-rays [77]. While, THz frequency images can differentiate between various tissue types within a human tooth, detect early-stage caries in the enamel layers, and monitor the initial erosion of enamel at the tooth surface [72]. Furthermore, THz frequencies are more and more utilized in the security screening sector, such as airports. Compared with the traditional approaches, such as X-ray inspection, THz frequency application has several advantages [78, 79]: it enables two-dimensional imaging where materials like clothing and paper are transparent, while plastic and ceramics are difficult to detect in X-ray; high-resolution 3D imaging using femtosecond pulses allows for detailed analysis, such as resolving thin layers or individual pages inside an envelope; THz spectroscopy detects chemical signatures even when substances are sealed in packets or hidden in clothing; and its non-ionizing radiation can be used safely at low power levels, thanks to high-sensitivity coherent detection.

Currently, THz spectrometers on the market are bulky and expensive, making them unsuitable for clinical investigations and on-site measurements. In this chapter, we introduce the innovative approach of the THz FMCW Fourier-Transform Spectrometer (THz-FMCW-FTS) to develop portable spectrometers. With this new technology, we aim to create a compact, cost-effective, and high-specificity spectrometer that is an ideal candidate for clinical investigations and on-site measurements. However, to validate our results, we must first carefully examine the outcomes from traditional THz spectrometers, which are discussed here.

The traditional methods make use of Vector Network Analyzers (VNA) and lenses that focus the electromagnetic beam to the center of the sample. Resonant methods and Transmission/Reflection (T/R) methods [89, 90] are the two main categories utilized to extract the material properties, especially the dielectric constant, from the traditional setup.

The resonant methods have evolved over many years, and various algorithms have been successfully developed to characterize material properties in different scenarios. Resonant techniques can achieve highly accurate electromagnetic characterization, but they demand precise fabrication of both the test sample and the designed resonator [90]. In addition, this approach is often expensive to conduct. In contrast, unlike resonant methods, which perform single-frequency or multi-frequency measurements, T/R characterization is inherently wideband. The valid frequency range for characterization depends on the specific T/R device and the measurement equipment used [89].

The T/R methods have also evolved over many years, and various algorithms have been successfully developed to characterize material properties in different scenarios [89, 90]. The Nicholson–Ross–Weir Method (NRW) is the most popular and classic approach to extract the dielectric constants of materials and it is known for its simple analytic procedures based on the measured scattering parameters [91, 92]. However, this approach has some drawbacks. For instance, it doesn't work well for low-loss materials at certain frequencies—specifically when the sample length matches a half-wavelength or its multiples—because the results can become unstable or inaccurate [93]. To address these limitations, numerous enhanced T/R methods have been developed over the years to extract material properties under more specific and tailored conditions.

For example, reference [93] proposes a robust iterative procedure that remains stable across the full frequency range, including the problematic half-wavelength points, which allows for the use of samples of arbitrary length, which significantly improves the accuracy and sensitivity of the measurement for low-loss materials. Also, another paper [94] improves upon the NRW method by replacing the point-by-point solution with a nonlinear least-squares regression approach that fits the entire frequency range simultaneously. By incorporating causality and physical constraints into the model, it ensures more stable and physically meaningful results, especially for low-loss or high-permittivity materials. Unlike the NRW method, it also accounts for uncertainties in sample length and position, and is robust against higher-order mode effects and reference plane errors. Another work [95] improves the traditional Nicolson–Ross–Weir (NRW) method by introducing a stepwise extraction technique that avoids the need for branch selection at each frequency point. Instead of resolving the phase ambiguity caused by the periodicity of the phase factor at every step, the proposed method tracks phase differences between adjacent frequencies to maintain the correct solution branch throughout the frequency range. This makes it capable of handling electrically thick samples—beyond half a wavelength—where the classical NRW method typically fails.

In addition, different tailored approaches are developed to extract material properties in more specific scenarios. For example, reference [96] illustrates an approach to measure the impedance of thin conductive films accurately at microwave frequencies. Paper [97] proposed an approach to measure the dielectric constant and loss tangents of high dielectric materials, such as steatite, alumina, titania loaded polystyrene, and zirconium-tin-titanate, at THz frequencies. Another paper [171] developed a modified T/R method that successfully measures the dielectric constants of thin, flexible, high-loss materials.

Out of all the different approaches, free-space techniques for the measurement of electromagnetic properties of materials are gaining popularity. Free-space techniques offer several key advantages for material property measurements. They avoid the excitation of unwanted higher-order modes that often arise in hollow waveguides when testing inhomogeneous materials like ceramics and composites. These methods are also non-destructive and contactless, making them suitable for measurements under special conditions such as high temperatures. Unlike waveguide-based methods, free-space techniques do not require precise machining of samples, eliminating errors caused by air gaps. Additionally, their flexible setup, with adjustable antennas and a dedicated sample holder, minimizes boundary effects and supports various angles of wave incidence [90].

Our approach falls into the category of free-space technique, which is particularly suited for scenarios where traditional contact-based measurement methods may not be applicable or convenient. In this approach, we leverage a variety of advanced components to ensure high precision and reliability in the measurements. Specifically, we utilize a PNA-X Network Analyzer (N5242A),

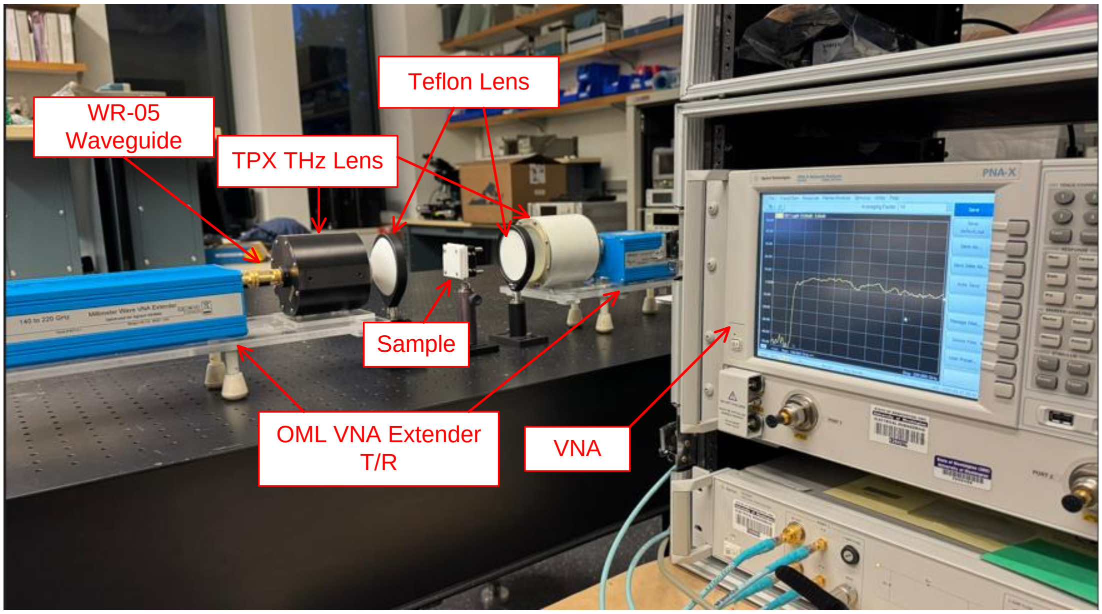

Figure 4.1: Conventional material characterization setup

a high-performance instrument renowned for its ability to measure complex S-parameters with exceptional accuracy and speed. To further extend the range of this setup, we incorporate an OML VNA Extender T/R, which enables the system to operate efficiently at sub-THz frequencies, crucial for our target applications.

Additionally, we employ TPX THz lens and Teflon lens designed to focus the beam precisely into the desired position, ensuring that the measurement is accurately captured at the intended point of interest. The configuration of these lenses is illustrated in Fig. 4.1, which shows the optimal alignment of all components to achieve the desired performance. The precise positioning and beam focusing are key to ensuring that the measurements remain within the expected range, especially in scenarios where precise alignment is critical. To ensure that the beam is accurately focused at the sample location, we used FEKO simulation software to identify the optimal position for the sample. As demonstrated in Fig. 4.2(a) and (b), the simulation revealed the focal point, which is the location where the Gaussian beam is formed with minimal divergence. This precise focus is crucial for the accuracy of algorithm development in the subsequent steps.

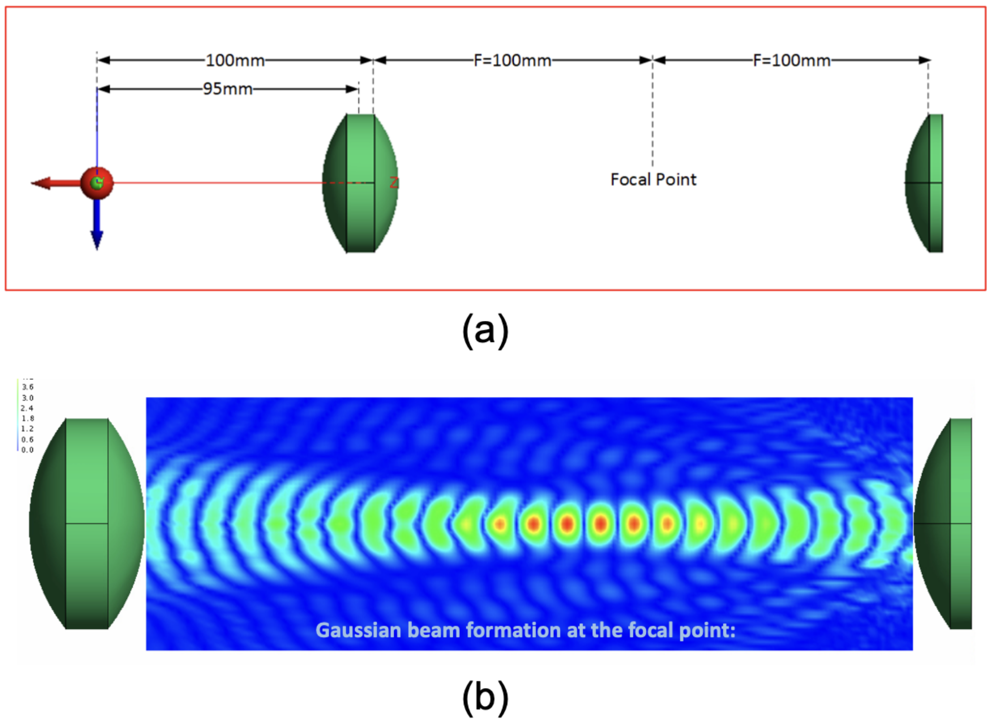

Figure 4.2: (a)The simulation to find the focal point (b)The simulation to show Gaussian beam formation at the focal point

An important aspect of our approach is the development of a novel algorithm tailored specifically for our experimental setup. This algorithm is designed to optimize the measurement process and is highly adaptable to the specific needs of our configuration. A key feature of this method is that it does not require a traditional calibration process, which is often time-consuming and prone to errors. Furthermore, it does not rely on the exact information about the distance between the signal transmitter and the sample, making the setup significantly more flexible and user-friendly. This is achieved by relying primarily on the complex transmission coefficients, which contain all the necessary information for accurate analysis. The details of this method, including the mathematical framework and implementation, will be discussed in greater depth in the following sections. This innovation represents a significant step forward in simplifying and streamlining the measurement process without sacrificing accuracy or reliability.

4.3 *Material Characterization Methods and Experimental Results with Conventional Measurement Setup*

In this algorithm, we aim to estimate the complex dielectric constant $\varepsilon_r = a - jb$ by analyzing the transmission coefficient data, specifically the S_{21} parameter, measured at various frequencies. Although it is theoretically possible to estimate the dielectric constant using a single sample, we use multiple thicknesses in this approach to enhance the accuracy of the results. By incorporating different thicknesses, the algorithm becomes more robust, accounting for the variations in real-world material behaviors, leading to a more reliable estimate of the dielectric constant.

The core of the algorithm involves loading experimental data for the S_{21} parameters, which are measured at various sample thicknesses. The data is preprocessed by removing any missing or incomplete values, ensuring that only valid measurements are used in the subsequent analysis. This step ensures the reliability of the data used for estimation. The S_{21} measurements for several sample thicknesses are then converted to complex form, with both magnitude (A_n) and phase (ϕ_n) information being used to obtain the full complex value of the transmission coefficient at each frequency:

$$S21_{\text{air}} = \mathrm{A}_0 \cdot e^{j \cdot \phi_0}$$

$$S21_n = \mathrm{A}_n \cdot e^{j \cdot \phi_n}, n = 1, 2, 3, ...$$

After preprocessing, the next task is to calculate the propagation constant and impedance for each material, as well as the reflection coefficients (Γ_1 and Γ_2) and transmission coefficients (T_1 and T_2), which are critical for modeling the transmission behavior of the material. The reflection coefficients (Γ_1 and Γ_2) describe how much of the wave is reflected at the sample-air interfaces, while the transmission coefficients (T_1 and T_2) model how much of the wave is transmitted to the sample. These coefficients are essential for understanding how the signal propagates through the medium.

The sample-under-test reflection (Γ) and transmission (T) coefficients are given by the following equations:

$$\Gamma_1 = \frac{Z_1 - Z_0}{Z_1 + Z_0}, \quad \Gamma_2 = \frac{Z_0 - Z_1}{Z_0 + Z_1}$$

$$T_1 = 1 + \Gamma_1, \quad T_2 = 1 + \Gamma_2$$

where, $Z_1 = 120\pi/\sqrt{\epsilon_r}$ is the characteristic impedance of the sample-under test, and $Z_0 = 120\pi$ is the free-space characteristic impedance. Next, the transmission coefficients $TT1$, $TT2$, and $TT3$ are calculated based on the experimental data for the different sample thicknesses. These coefficients adjust the measured S_{21} values for the propagation distances d_n ($n = 1, 2, 3, ...$), and they are used to model the transmission through the material. The experimental transmission coefficients for each sample thickness are given by:

$$\text{TT}n = \frac{S21_n}{S21_{\text{air}}} e^{-jk_0 d_n}, n = 1, 2, 3, ...$$

The next crucial step involves modeling the transmission behavior using a Fabry–Pérot formulation. This model incorporates the transmission coefficients and considers internal reflections and wave propagation through the material. The modeled S_{21} values are compared against the experimental data to compute the residuals, which represent the difference between the measured and modeled transmission coefficients. The modeled S_{21} values for each sample thickness are given by:

$$S21_{\text{model } n} = \frac{T_1 T_2 e^{-jk_0\sqrt{\varepsilon_r} d_n}}{1 - \Gamma_2^2 e^{-2jk_0\sqrt{\varepsilon_r} d_n}}, n = 1, 2, 3, ...$$

The residual function is defined to minimize the difference between the measured and modeled S_{21} values. The residuals are computed by subtracting the modeled values ($\text{S21}_{\text{model } n}$) from the experimental ones (TTn), and this difference is used to optimize the dielectric constant. The residual function F considers both the real and imaginary parts of the residuals for each sample thickness:

$$F = [\text{real}(r_1), \text{imag}(r_1), \text{real}(r_2), \text{imag}(r_2), \text{real}(r_3), \text{imag}(r_3), ...]$$

where r_1, r_2, and r_3 represent the residuals for the three different sample thicknesses. The algorithm uses a nonlinear optimization method in MATLAB (specifically the `fsolve` function) to minimize these residuals and find the best estimate for the dielectric constant $\varepsilon_r = a - jb$. The algorithm iterates through the optimization steps, updating the initial guess for the dielectric constant based on the current solution. If the residual norm is sufficiently small (e.g., `resnorm` < 0.1), the solution is accepted. Finally, the real part of the dielectric constant $\epsilon_r = a$ and the loss tangent $\tan\delta = \frac{b}{a}$ are computed. These values are essential for characterizing the material's electromagnetic properties, and they are plotted as a function of frequency to observe how the material behaves over the frequency range of interest.

While only one material is theoretically necessary to obtain analytical results for the dielectric constant, we can use multiple materials in this algorithm to improve the accuracy and robustness of the estimates. By incorporating different samples with varying thicknesses, we account for the real-world variations in material properties, leading to more accurate and reliable results.

Based on the methods described previously, we conducted comprehensive experiments to collect the dielectric constants of various materials in order to build a database for terahertz frequency applications. The first set of materials measured was Teflon as shown in Fig. 4.3a. The results in Fig. 4.4 indicate that the real part of the dielectric constant for Teflon is approximately 2.05 within the frequency range of 150 GHz to 220 GHz. This value is consistent with the dielectric constants of Teflon observed at lower frequencies [172]. The negative values recorded for the loss tangent of the dielectric constant are due to limitations of the algorithm, which is not well-suited for low-loss materials. Nonetheless, the overall loss tangent for Teflon remains close to 0, which is logical given its properties.

The second material measured is Acrylonitrile–Butadiene–Styrene (ABS), as shown in Fig. 4.3b. The results derived from the measurements are shown Fig. 4.5. The real part of the dielectric constant for ABS is approximately 2.5 within the frequency range of 150 GHz to 220 GHz, and the loss tangent is a very small positive value, close to zero. A similar material, Polylactic Acid (PLA) as shown in Fig. 4.3c, was also measured within the same frequency range. The real part of the dielectric constant and loss tangent for PLA, illustrated in Fig. 4.6, exhibit trends similar to those of ABS. The measured values of both materials align well with expected standards since in the lower frequencies, both materials have a dielectric constant from 2 to 3 and very small loss tangent [173].

The fourth material measured is epoxy resin composite, whose samples are shown in Fig. 4.3d. The results derived from the measurements are shown in Fig. 4.7. Compared with ABS and PLA, this material has a higher real part of the dielectric constant and a similar loss tangent. Although we expected a larger loss tangent for epoxy resin, as it is considered a more lossy material—this paper, for example, found a loss tangent of 0.06 for epoxy resin at 2.45 GHz [174]—the lower-than-expected loss tangent can be related to changes in the loss tangent at THz frequencies. It is important to note that epoxy resin is one of the most important materials for our database, since it can be used to manufacture antennas operating at terahertz frequencies with high precision (micrometer resolution).

The last material measured is a piece of Ribbon Coring Alumina Ceramic with a thickness of $40\ \mu m$. Unlike traditional ceramics, this material is flexible and can be very useful in antenna design at the sub-THz frequency range. The appearance of this material is shown in Fig. 4.3f. The measured real part of the dielectric constant and loss tangent are presented in Fig. 4.8. In addition to this thin alumina ceramic, we conducted a different test with a thicker alumina ceramic, which has a thickness of $3.84\ mm$, and the sample is shown in Fig. 4.3e. The measured results are shown in Fig. 4.9. It is observed that both tests show a real part around 10 and a small loss tangent. The larger loss tangent for the Ribbon ceramic can be attributed to the low thickness of the sample ($40\mu m$), which causes less interaction between the sample and the electromagnetic waves, eventually leading to errors in determining the loss tangent. However, the thicker alumina provides more reliable data for the loss tangent, as it involves multiple wavelengths of interaction between the wave and the material. The average loss tangent over the frequency range 150 GHz to 220 GHz is close to 0.

In conclusion, the conventional setup with the proposed algorithm is more effective for materials with higher loss tangents. For materials with higher dielectric constants, such as silicon ($\varepsilon = 10$), multilayer structures should be avoided due to the air gap, which introduces significant errors. While this method works well for materials with smaller dielectric constants and single-layer structures, it still faces certain challenges, particularly for low-loss materials, where achieving accurate loss tangent measurements remains difficult. The small negative values for the loss tangent in Fig. 4.4b and Fig. 4.9(b) are due to the general weakness of T/R-based methods for extracting low-loss material properties. For low-loss materials, the samples are often too thin to allow the waves to propagate a sufficient distance to effectively demonstrate loss. This also explains why the loss tangent pattern appears unstable in Fig. 4.4b for low-loss materials like Teflon. A resonant-based method is needed for this type of low-loss materials. The method is also generally not suitable for multilayer structures. Thin materials allow for easier approximation of the dielectric constant, even if the initial guess is not accurate. However, for thicker materials, the initial estimate plays a more crucial role, and when the initial guess is close, the accuracy of the results is better than that obtained from thin materials. Therefore, with a proper initial estimate, thicker materials typically yield better results.

4.4 *Material Characterization using THz FMCW Radars*

In recent years, THz and mm-wave systems have attracted many researchers because of the numerous promising applications they provide. Various theoretical and experimental efforts have been made to establish THz-frequency sensing as a new characterization tool for security screening, industrial quality control, and biological spectrometry applications. Due to the short wavelength of the THz band, on the order of micrometers, it possesses unique features that distinguish it from neighboring bands such as mm-wave and infrared (IR).

In this research, we introduce a THz FMCW Fourier-Transform Spectrometer (THz-FMCW-FTS) to demonstrate the capability of integrated circuits for spectroscopy and material characterization at the lower side of the THz band. Currently, THz spectrometers on the market are bulky and expensive, making them unsuitable for on-site measurements. With this new technology, we aim to develop a compact, cost-effective, and high-specificity spectrometer that is an ideal candidate for on-site measurements. The primary objective of this thesis is to measure the complex dielectric constant of solid materials in the THz band for the design of 3D-printed THz dielectric antennas; however, the same setup is applicable for liquid and gas samples for medical and pharmaceutical studies. The THz FMCW chips used for this part of the thesis are 190–257 GHz FMCW radars, as discussed in [51, 52].

Fourier-transform interferometry (FTS) is a suitable technique for resolving the frequency components of broadband signals. However, in conventional Fourier-transform spectrometers, the signal path difference required for a $10kHz$ resolution is $30km$, which is impractical. In our proposed structure, we mix FMCW radar with a Fourier-transform spectrometer to decrease this range to a couple of centimeters with the same frequency resolution. In Fig. 4.10, we have shown the comparison between a conventional FTS and the proposed FMCW-FTS. All of the fix components in the conventional system are embedded inside a single FMCW radar chip, which makes the system compact.

Figure 4.11 shows the preliminary setup for the THz-FMCW-FTS. In this setup, an FMCW radar chip compares the radiated signal with a reference signal, which is a sample of the VCO signal. By repeating this measurement twice—once with and once without the presence of the sample—we can extract the material properties placed in the path of the radiated signal. At the sample location in Fig. 4.11, the electric fields are focused by two back-to-back Teflon lenses. This focused beam reduces the size of the sample under test, which is a critical feature in medical and pharmaceutical applications where the sample volume is limited.

The measurement procedure is the same as conventional FTS. However, in our proposed method, instead of generating a 1-D signal like the standard method, we make a 2-D signal, which remarkably decreases the size of motion of the reflector from km to cm with the same frequency resolution. In each reflector position, we store the IF signal of FMCW radar and then move the reflector to the next step with 10 μm distance. This procedure repeats for the length of $5cm$ (5000 measurements). With locating the IF signals side-by-side as shown in Fig. 4.12a, for each fixed time, we take a Fourier-transform from the data. As a result, which is presented in Fig. 4.12b, we achieve a spectrogram which shows the frequency content of the radiated signal. By repeating this measurement with and without a sample and comparing the spectrograms, we can extract the material characteristics, which could be complex permittivity for solids and liquids, and specific resonance frequencies for gas samples.

During this measurement, we have been able to measure the radiated frequency of FMCW radars. Now, if we put a material in front of the radar, and repeat the THz-FMCW-FTS, we can measure the material properties of the sample. The amplitude of the received signal can have information about the dielectric loss of the material, and the phase of the received signal is proportional to the permittivity of the sample. In the next phase of the research, we will develop the theory to extract the material characteristics from the output signal of the radar.

4.5 *Summary*

Chapter 4 establishes a comprehensive framework for constructing a reliable terahertz-range dielectric constant database using two measurement pathways. The transmission-based dielectric constant measurements performed with a VNA and frequency extenders are processed via a custom algorithm to yield real and imaginary permittivity values over $150\text{–}220$ GHz for different materials. In parallel, a cost-effective FMCW radar has been introduced to conduct the same measurements with much lower cost and complexity. The integration of these methods delivers not only a robust catalog of THz dielectric properties but also a scalable methodology for future database expansion. This database will streamline terahertz component design, enhance simulation fidelity, and lower barriers for emerging applications in high-speed communications, imaging, and sensing at THz frequencies.

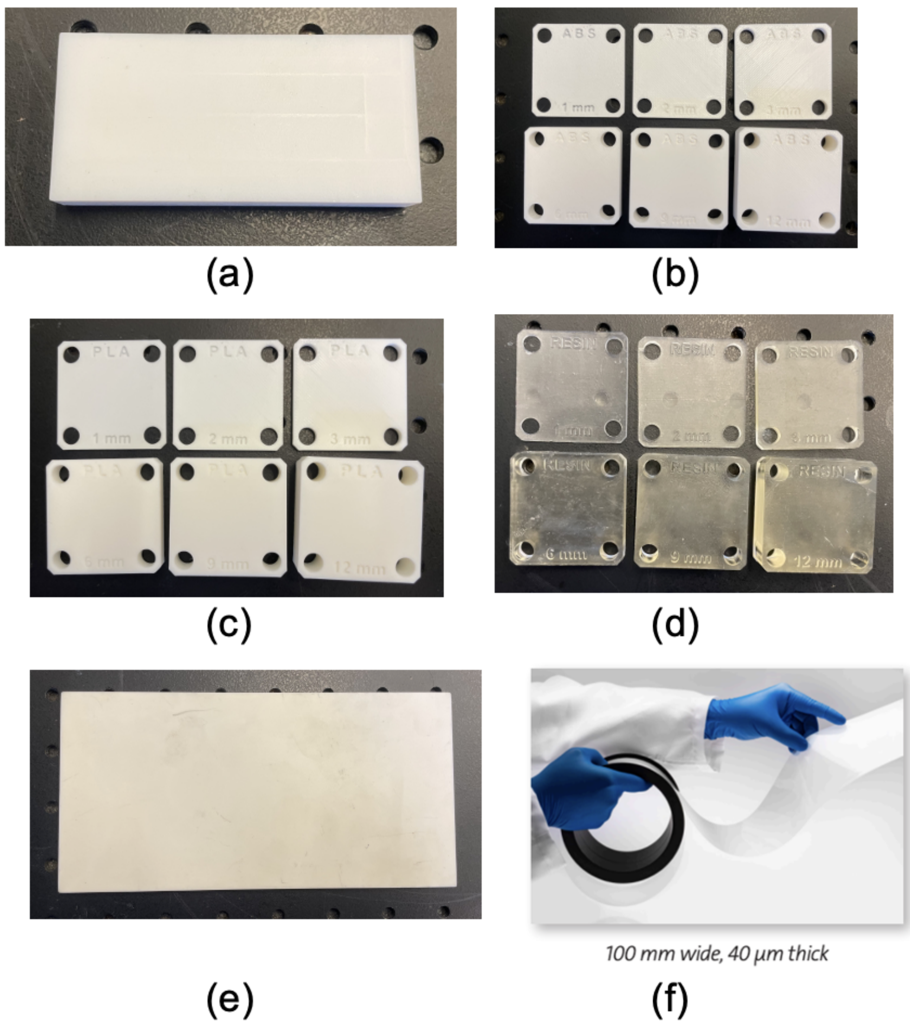

Figure 4.3: (a) Teflon, (b) ABS, (c) PLA, (d) Resin, (e) Alumina, (f) Coring Ribbon Alumina Ceramic.

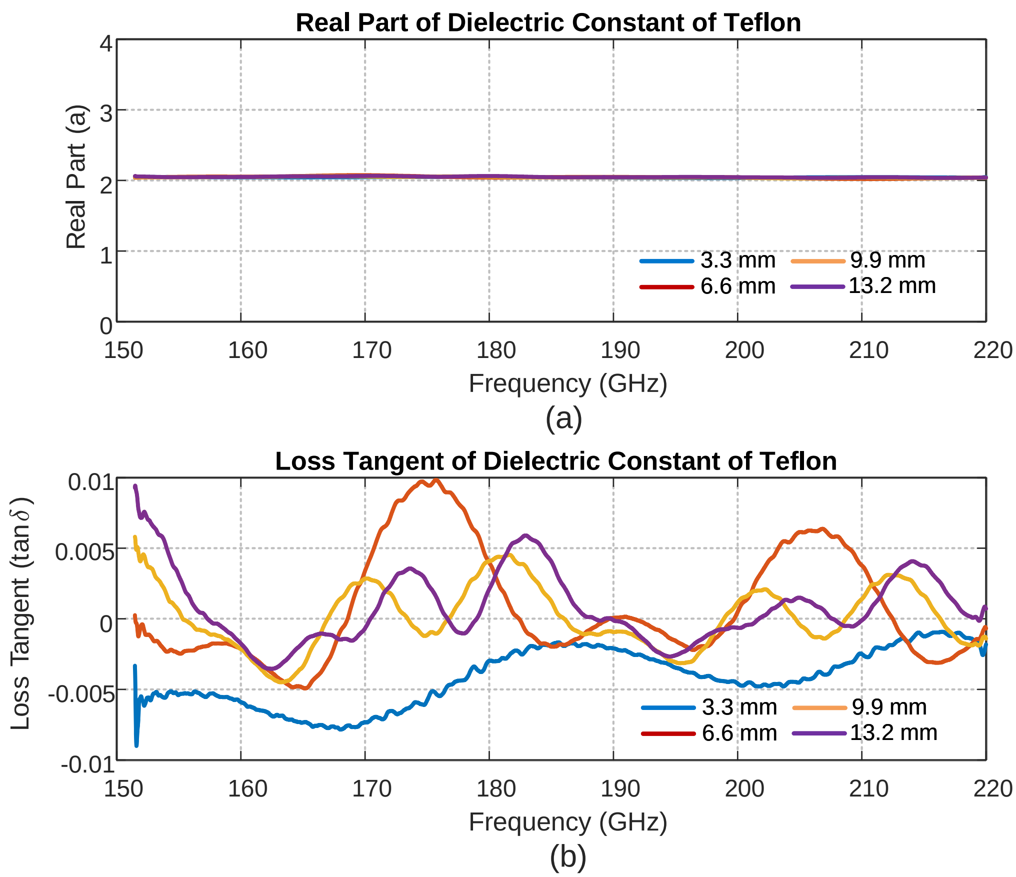

Figure 4.4: Dielectric constants of Teflon measured by conventional setup

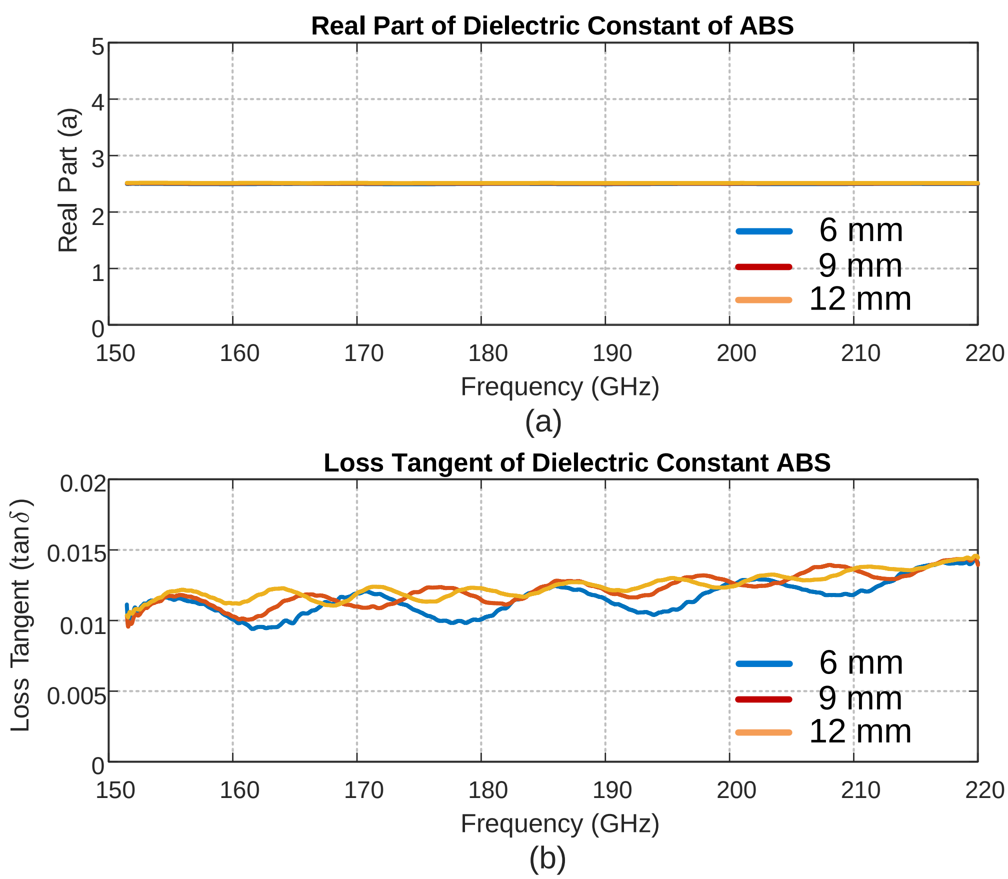

Figure 4.5: Dielectric constants of ABS measured by conventional setup

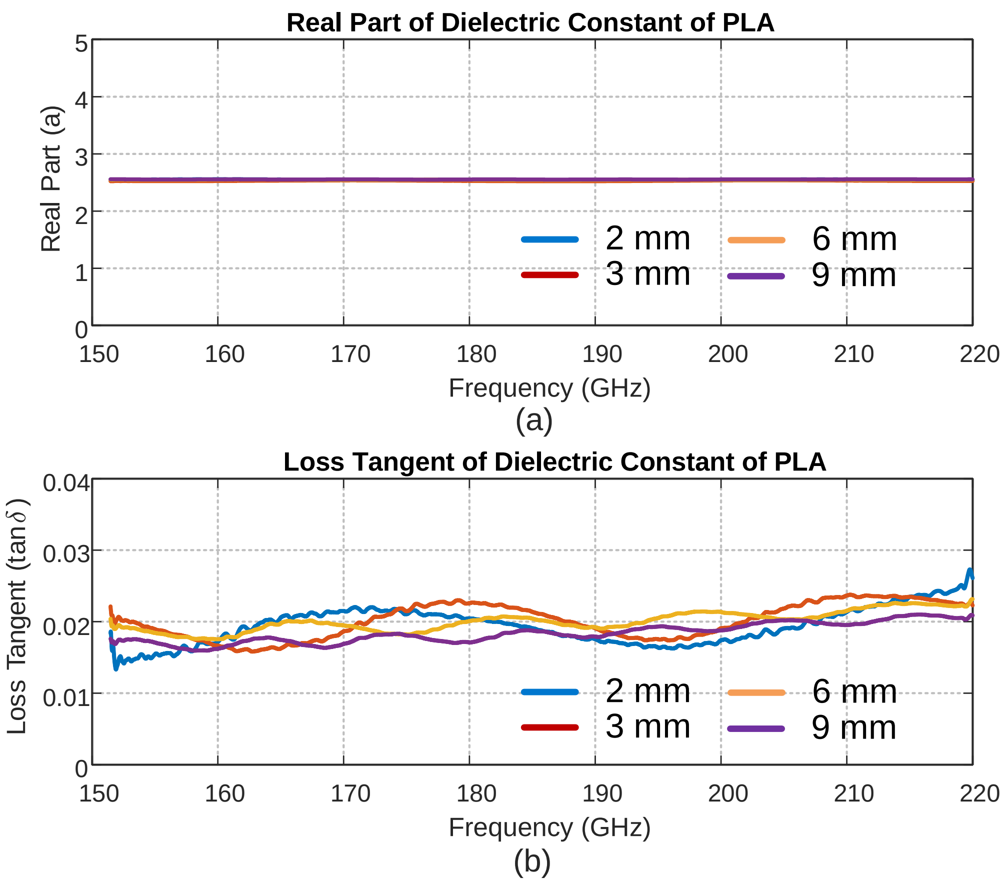

Figure 4.6: Dielectric constants of PLA measured by conventional setup

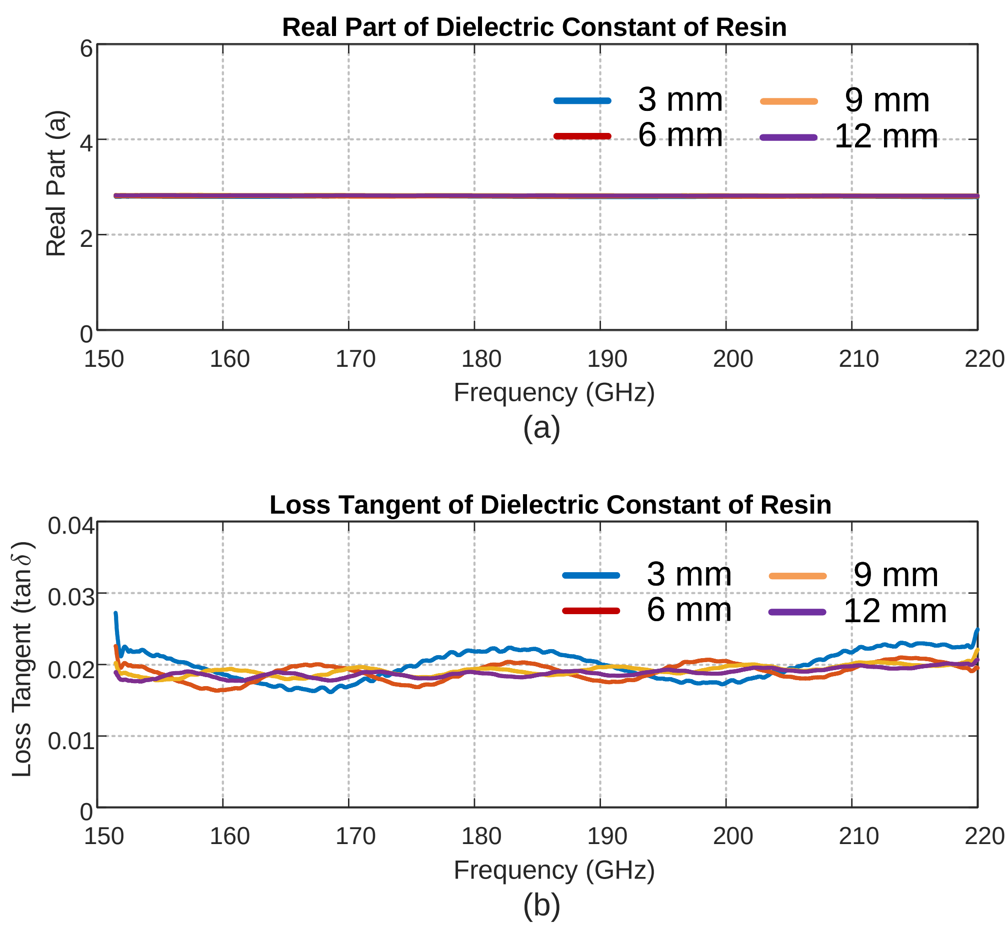

Figure 4.7: Dielectric constants of Resin measured by conventional setup

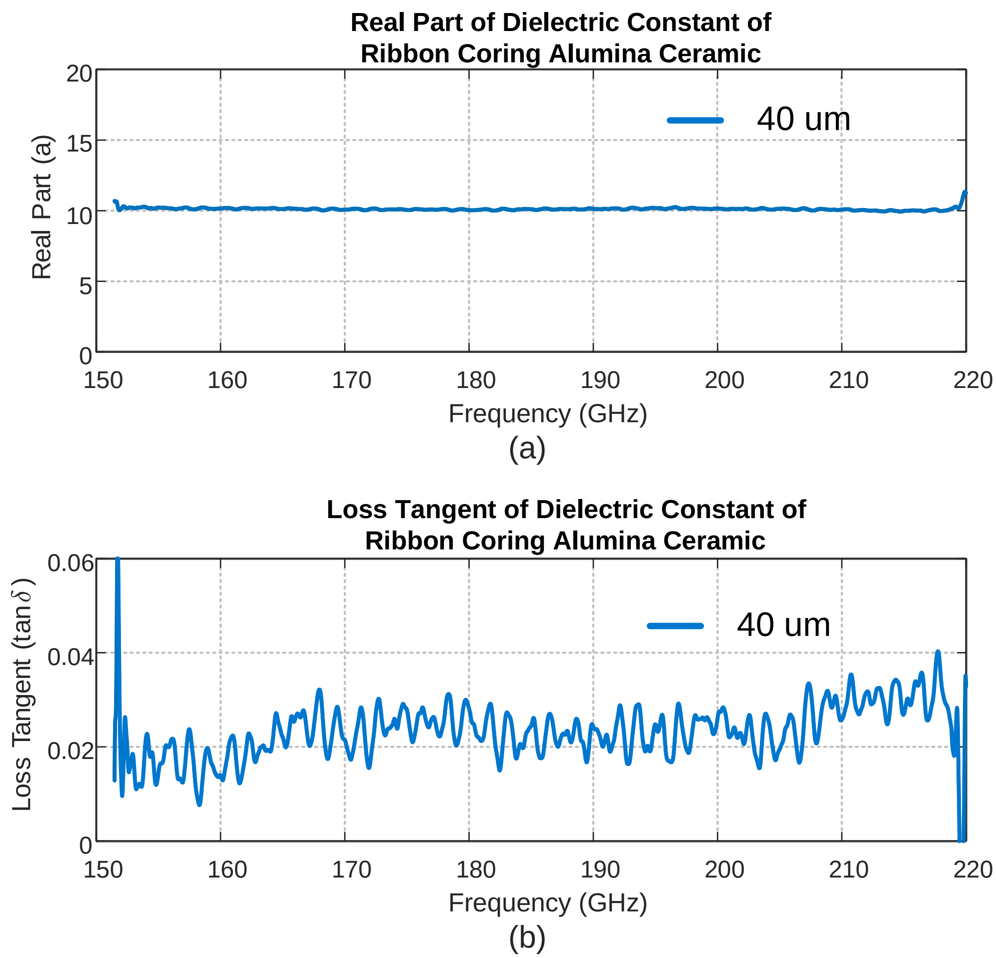

Figure 4.8: Dielectric constants of Ribbon Coring Alumina Ceramic measured by conventional setup

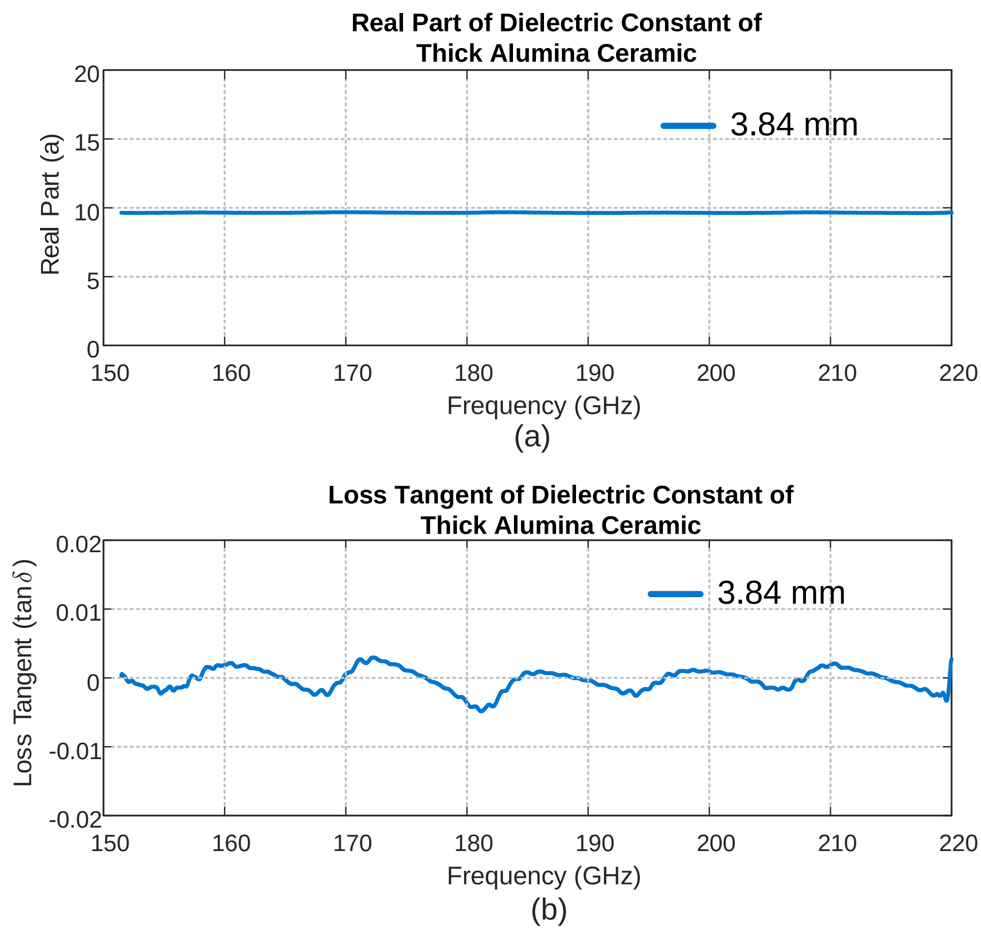

Figure 4.9: Dielectric constants of Thick Alumina Ceramic measured by conventional setup

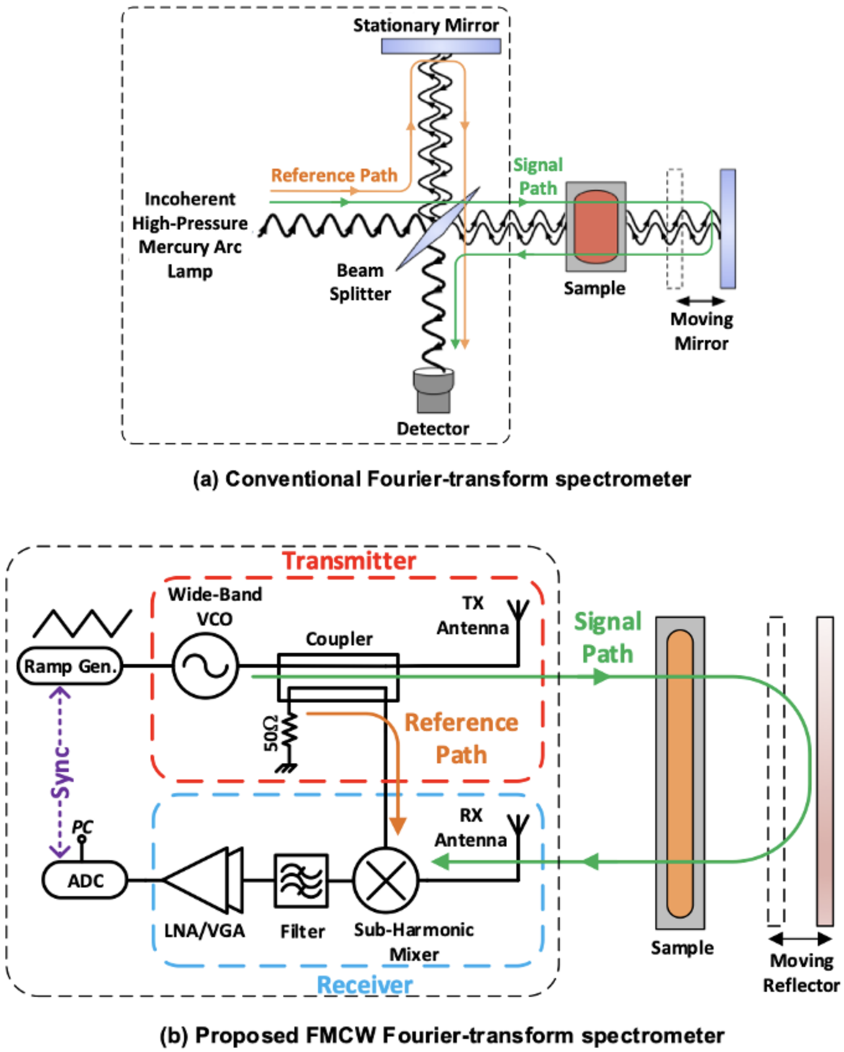

Figure 4.10: (a) Conventional Fourier-transform spectrometer (b) Proposed FMCW Fourier-transform spectrometer

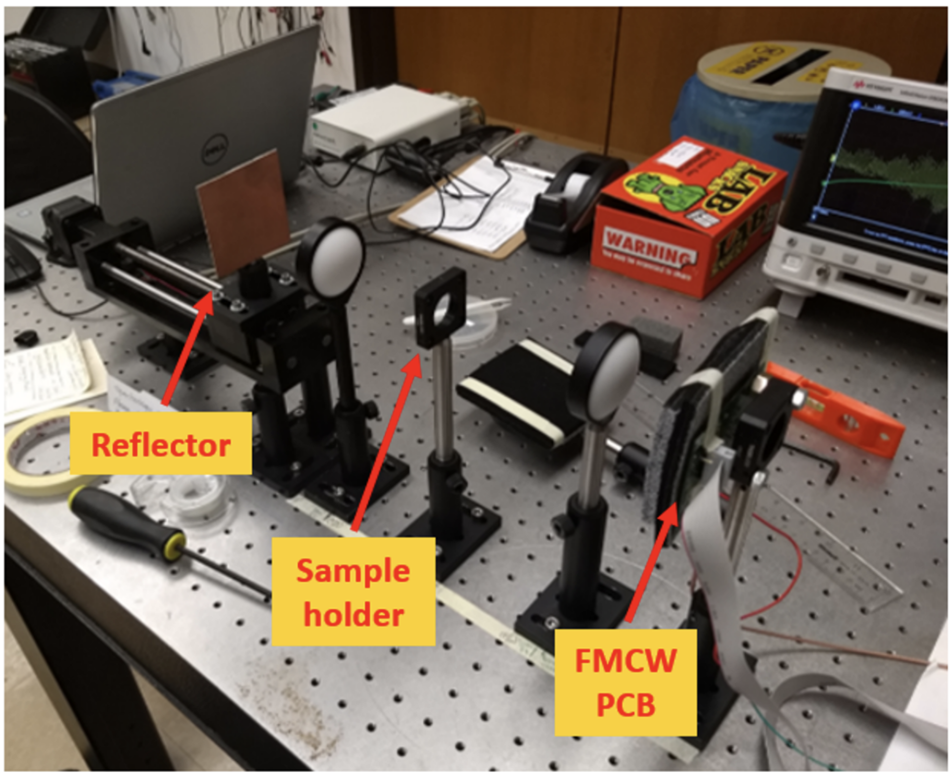

Figure 4.11: Setup of THz-FMCW-FTS

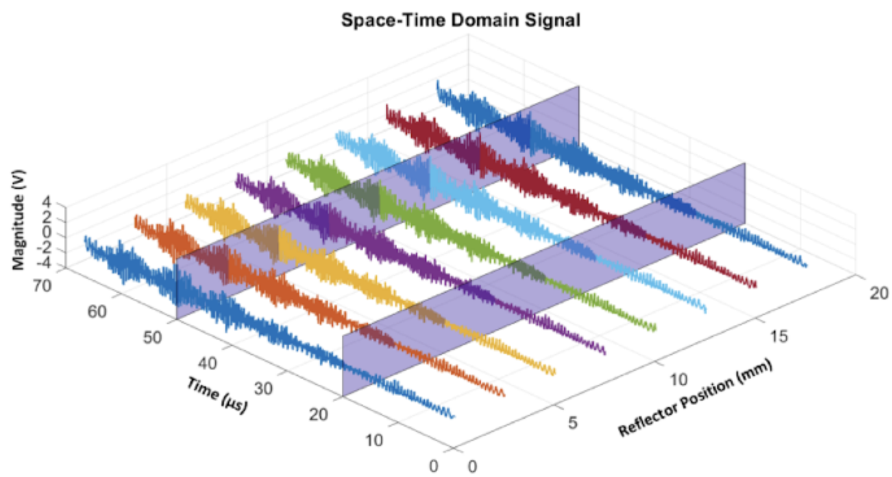

(a) 2D signal of the spectrometer

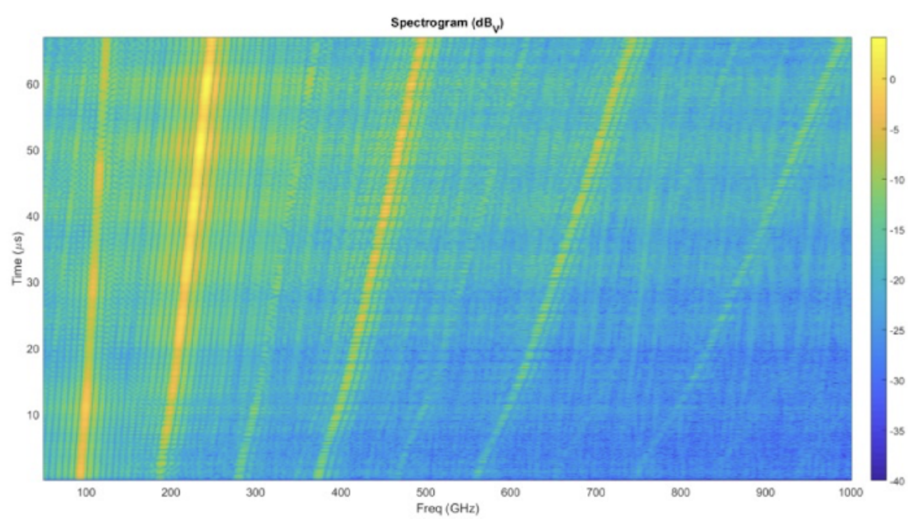

(b) Spectrogram

Figure 4.12: (a) 2-D output signal (b) spectrogram of the FMCW-FTS system.

BIBLIOGRAPHY

[1] University of Washington, "Deep Profiler Moorings," 2023, accessed: 2025-03-28. [Online]. Available: https://interactiveoceans.washington.edu/technology/deep-profiler-moorings/

[2] E. Sala, J. Mayorga, D. Bradley, R. B. Cabral, T. B. Atwood, A. Auber, W. Cheung, C. Costello, F. Ferretti, A. M. Friedlander *et al.*, "Protecting the global ocean for biodiversity, food and climate," *Nature*, vol. 592, no. 7854, pp. 397–402, 2021.

[3] M. Deacon, *Scientists and the sea, 1650–1900: a study of marine science*. Routledge, 2018.

[4] M. F. Ali, D. N. K. Jayakody, Y. A. Chursin, S. Affes, and S. Dmitry, "Recent advances and future directions on underwater wireless communications," *Archives of Computational Methods in Engineering*, vol. 27, pp. 1379–1412, 2020.

[5] H. Hu, W. Xue, P. Jiang, and Y. Li, "Bibliometric analysis for ocean renewable energy: An comprehensive review for hotspots, frontiers, and emerging trends," *Renewable and Sustainable Energy Reviews*, vol. 167, p. 112739, 2022.

[6] M. Z. A. Khan, H. A. Khan, and M. Aziz, "Harvesting energy from ocean: Technologies and perspectives," *Energies*, vol. 15, no. 9, p. 3456, 2022.

[7] P. C. Reid, A. C. Fischer, E. Lewis-Brown, M. P. Meredith, M. Sparrow, A. J. Andersson, A. Antia, N. R. Bates, U. Bathmann, G. Beaugrand *et al.*, "Impacts of the oceans on climate change," *Advances in marine biology*, vol. 56, pp. 1–150, 2009.

[8] J. P. Abraham, M. Baringer, N. L. Bindoff, T. Boyer, L. Cheng, J. A. Church, J. L. Conroy, C. M. Domingues, J. T. Fasullo, J. Gilson *et al.*, "A review of global ocean temperature observations: Implications for ocean heat content estimates and climate change," *Reviews of Geophysics*, vol. 51, no. 3, pp. 450–483, 2013.

[9] G. R. Bigg, T. D. Jickells, P. S. Liss, and T. J. Osborn, "The role of the oceans in climate," *International Journal of Climatology: A journal of the Royal Meteorological Society*, vol. 23, no. 10, pp. 1127–1159, 2003.

[10] K. L. Nash, I. Van Putten, K. A. Alexander, S. Bettiol, C. Cvitanovic, A. K. Farmery, E. J. Flies, S. Ison, R. Kelly, M. Mackay *et al.*, "Oceans and society: feedbacks between ocean and human health," *Reviews in Fish Biology and Fisheries*, pp. 1–27, 2022.

[11] B. Neumann, A. T. Vafeidis, J. Zimmermann, and R. J. Nicholls, “Future coastal population growth and exposure to sea-level rise and coastal flooding-a global assessment,” *PloS one*, vol. 10, no. 3, p. e0118571, 2015.

[12] K. C. Seto, “Exploring the dynamics of migration to mega-delta cities in Asia and Africa: Contemporary drivers and future scenarios,” *Global Environmental Change*, vol. 21, pp. S94–S107, 2011.

[13] J.-L. Merkens, L. Reimann, J. Hinkel, and A. T. Vafeidis, “Gridded population projections for the coastal zone under the Shared Socioeconomic Pathways,” *Global and Planetary Change*, vol. 145, pp. 57–66, 2016.

[14] W. Steffen, W. Broadgate, L. Deutsch, O. Gaffney, and C. Ludwig, “The trajectory of the Anthropocene: the great acceleration,” *The anthropocene review*, vol. 2, no. 1, pp. 81–98, 2015.

[15] L. A. Levin, B. J. Bett, A. R. Gates, P. Heimbach, B. M. Howe, F. Janssen, A. McCurdy, H. A. Ruhl, P. Snelgrove, K. I. Stocks *et al.*, “Global observing needs in the deep ocean,” *Frontiers in Marine Science*, vol. 6, p. 241, 2019.

[16] A. Quazi and W. Konrad, “Underwater acoustic communications,” *IEEE Communications Magazine*, vol. 20, no. 2, pp. 24–30, 1982.

[17] D. Park, K. Kwak, W. K. Chung, and J. Kim, “Development of underwater short-range sensor using electromagnetic wave attenuation,” *IEEE Journal of Oceanic Engineering*, vol. 41, no. 2, pp. 318–325, 2015.

[18] M. J. McPhaden, “The tropical atmosphere ocean array is completed,” *Bulletin of the American Meteorological Society*, vol. 76, no. 5, pp. 739–741, 1995.

[19] G. C. Johnson, S. Hosoda, S. R. Jayne, P. R. Oke, S. C. Riser, D. Roemmich, T. Suga, V. Thierry, S. E. Wijffels, and J. Xu, “Argo—Two decades: Global oceanography, revolutionized,” *Annual review of marine science*, vol. 14, no. 1, pp. 379–403, 2022.

[20] T. C. Malone, “The coastal module of the Global Ocean Observing System (GOOS): an assessment of current capabilities to detect change,” *Marine Policy*, vol. 27, no. 4, pp. 295–302, 2003.

[21] T. Podder, M. Sibenac, and J. Bellingham, “AUV docking system for sustainable science missions,” in *IEEE International Conference on Robotics and Automation, 2004. Proceedings. ICRA’04. 2004*, vol. 5. IEEE, 2004, pp. 4478–4484.

[22] N. Palomeras, G. Vallicrosa, A. Mallios, J. Bosch, E. Vidal, N. Hurtos, M. Carreras, and P. Ridao, “AUV homing and docking for remote operations,” *Ocean Engineering*, vol. 154, pp. 106–120, 2018.

[23] P. King, R. Lewis, D. Mouland, and D. Walker, “CATCHY an AUV ice dock,” in *OCEANS 2009*. IEEE, 2009, pp. 1–6.

[24] J. Zhou, H. Huang, S. Huang, Y. Si, K. Shi, X. Quan, C. Guo, C.-W. Chen, Z. Wang, Y. Wang *et al.*, “AUH, a new technology for ocean exploration,” *Engineering*, vol. 25, pp. 21–27, 2023.

[25] T. Xie, Y. Li, Y. Jiang, S. Pang, and X. Xu, “Three-dimensional mobile docking control method of an underactuated autonomous underwater vehicle,” *Ocean Engineering*, vol. 265, p. 112634, 2022.

[26] Y. Liu, C. Zhang, Y. Kuga, N. Michel-Hart, T. McGinnis, and C. Siani, “2.4 GHz Antenna for Deep Sea Communication,” in *2022 IEEE International Symposium on Antennas and Propagation and USNC-URSI Radio Science Meeting (AP-S/URSI)*. IEEE, 2022, pp. 1020–1021.

[27] T. McGinnis, G. Cram, and E. Boget, “Oceanographic Mooring Inductive Power Mooring Lines for OOI’s Shallow and Deep Profilers,” *SEA TECHNOLOGY*, vol. 61, no. 4, pp. 14–18, 2020.

[28] N. A. Cruz, A. C. Matos, R. M. Almeida, and B. M. Ferreira, “A lightweight docking station for a hovering AUV,” in *2017 IEEE Underwater Technology (UT)*. IEEE, 2017, pp. 1–7.

[29] J. G. Bellingham, “Autonomous underwater vehicle docking,” *Springer Handbook of Ocean Engineering*, pp. 387–406, 2016.

[30] X. Yang, K. G. Ong, W. R. Dreschel, K. Zeng, C. S. Mungle, and C. A. Grimes, “Design of a wireless sensor network for long-term, in-situ monitoring of an aqueous environment,” *Sensors*, vol. 2, no. 11, pp. 455–472, 2002.

[31] M. M. Hunt, W. M. Marquet, D. A. Moller, K. K. Peal, W. K. Smith, R. C. Spindel *et al.*, “An acoustic navigation system,” 1974.

[32] J. Yuh, G. Marani, and D. R. Blidberg, “Applications of marine robotic vehicles,” *Intelligent service robotics*, vol. 4, pp. 221–231, 2011.

[33] M. A. B. Yusof and S. Kabir, “An overview of sonar and electromagnetic waves for underwater communication,” *IETE Technical Review*, vol. 29, no. 4, pp. 307–317, 2012.

[34] A. I. Al-Shamma’a, A. Shaw, and S. Saman, “Propagation of electromagnetic waves at MHz frequencies through seawater,” *IEEE Transactions on antennas and propagation*, vol. 52, no. 11, pp. 2843–2849, 2004.

[35] A. Shaw, A. Al-Shamma’a, S. Wylie, and D. Toal, “Experimental investigations of electromagnetic wave propagation in seawater,” in *2006 european microwave conference*. IEEE, 2006, pp. 572–575.

[36] H. F. G. Mendez, F. Le Pennec, C. Gac, and C. Person, "Deep underwater compatible Wi-Fi antenna development," in *2011 The 14th International Symposium on Wireless Personal Multimedia Communications (WPMC)*. IEEE, 2011, pp. 1–5.

[37] Y. Du, Y. Xu, J. Wu, J. Qiao, Z. Wang, Z. Hu, Z. Jiang, and M. Liu, "Very-low-frequency magnetoelectric antennas for portable underwater communication: Theory and experiment," *IEEE Transactions on Antennas and Propagation*, vol. 71, no. 3, pp. 2167–2181, 2023.

[38] W. Honglei, Y. Kunde, and Z. Kun, "Performance of dipole antenna in underwater wireless sensor communication," *IEEE Sensors Journal*, vol. 15, no. 11, pp. 6354–6359, 2015.

[39] E. A. Karagianni, "Electromagnetic waves under sea: bow-tie antennas design for Wi-Fi underwater communications," *Progress In Electromagnetics Research M*, vol. 41, pp. 189–198, 2015.

[40] C. S. Gonçalves, B. M. Ferreira, and A. C. Matos, "Design and development of SHAD-a small hovering AUV with differential actuation," in *OCEANS 2016 MTS/IEEE Monterey*. IEEE, 2016, pp. 1–4.

[41] G. C. Smith, R. Allard, M. Babin, L. Bertino, M. Chevallier, G. Corlett, J. Crout, F. Davidson, B. Delille, S. T. Gille *et al.*, "Polar ocean observations: A critical gap in the observing system and its effect on environmental predictions from hours to a season," *Frontiers in Marine Science*, vol. 6, p. 429, 2019.

[42] J. Calder, A. Proshutinsky, E. Carmack, I. Ashik, H. Loeng, J. Key, M. McCammon, H. Melling, D. Perovich, H. Eicken *et al.*, "An integrated international approach to Arctic Ocean observations for society (A legacy of the International Polar Year)," *Proceedings of OceanObs*, vol. 9, 2010.

[43] D. Roemmich, G. C. Johnson, S. Riser, R. Davis, J. Gilson, W. B. Owens, S. L. Garzoli, C. Schmid, and M. Ignaszewski, "The Argo Program: Observing the global ocean with profiling floats," *Oceanography*, vol. 22, no. 2, pp. 34–43, 2009.

[44] E. Skinner, S. Kirn, and M. Hinders, "Development of underwater beacon for Arctic through-ice communication via satellite," *Cold Regions Science and Technology*, vol. 160, pp. 58–79, 2019.

[45] V. Badescu and K. Zacny, *Outer Solar System: Prospective Energy and Material Resources*. Springer, 2018.

[46] A. S. Ghazy, H. S. Khallaf, S. Hranilovic, and M.-A. Khalighi, "Under-sea ice diffusing optical communications," *IEEE Access*, vol. 9, pp. 159 652–159 671, 2021.

[47] Y. Liu, H. Naghavi, Y. Kuga, and J. M. Mower, “Loaded Waveguide Antenna for Undersea Communications,” in *2024 IEEE International Symposium on Antennas and Propagation and INC/USNC-URSI Radio Science Meeting (AP-S/INC-USNC-URSI)*, 2024, pp. 463–464.

[48] S. H. Naghavi, M. T. Taba, R. Han, M. A. Aseeri, A. Cathelin, and E. Afshari, “Filling the Gap With Sand: When CMOS Reaches THz,” *IEEE Solid-State Circuits Magazine*, vol. 11, no. 3, pp. 33–42, 2019.

[49] H. Aghasi, S. M. H. Naghavi, M. Tavakoli Taba, M. A. Aseeri, A. Cathelin, and E. Afshari, “Terahertz electronics: Application of wave propagation and nonlinear processes,” *Applied Physics Reviews*, vol. 7, no. 2, p. 021302, 04 2020.

[50] M. Tavakoli Taba, Z. Khalifa, S. H. Naghavi, and E. Afshari, “Progress Towards Fully On-Chip Frequency-Stabilization for Sub-Terahertz Sources,” in *2020 IEEE 20th Topical Meeting on Silicon Monolithic Integrated Circuits in RF Systems (SiRF)*, 2020, pp. 30–34.

[51] A. Mostajeran, S. M. Naghavi, M. Emadi, S. Samala, B. P. Ginsburg, M. Aseeri, and E. Afshari, “A High-Resolution 220-GHz Ultra-Wideband Fully Integrated ISAR Imaging System,” *IEEE Transactions on Microwave Theory and Techniques*, vol. 67, no. 1, pp. 429–442, 2019.

[52] S. M. Hossein Naghavi, S. Seyedabbaszadehesfahlani, F. Khoeini, A. Cathelin, and E. Afshari, “22.4 A 250GHz Autodyne FMCW Radar in 55nm BiCMOS with Micrometer Range Resolution,” in *2021 IEEE International Solid-State Circuits Conference (ISSCC)*, vol. 64, 2021, pp. 320–322.

[53] A. Mostajeran, H. Aghasi, S. M. H. Naghavi, and E. Afshari, “Fully Integrated Solutions for High Resolution Terahertz Imaging (Invited),” in *2019 IEEE Custom Integrated Circuits Conference (CICC)*, 2019, pp. 1–8.

[54] M. Tavakoli Taba, S. M. Hossein Naghavi, M. Fayazi, A. Sadeghi, A. Cathelin, and E. Afshari, “A Compact CMOS 363 GHz Autodyne FMCW Radar with 57 GHz Bandwidth for Dental Imaging,” in *2023 IEEE Custom Integrated Circuits Conference (CICC)*, 2023, pp. 1–2.

[55] S. M. H. Naghavi, M. T. Taba, B. Yektakhah, M. Aseeri, A. Cathelin, and E. Afshari, “Broadband Sub-THz Chirp Linearization Using Particle Swarm Optimization for Precision Metrology Applications,” in *2021 IEEE MTT-S International Microwave Symposium (IMS)*, 2021, pp. 752–755.

[56] B. Hadidian, F. Khoeini, S. M. Hossein Naghavi, A. Cathelin, K. Sarabandi, and E. Afshari, “A 194-238GHz Fully On-Chip Self-Referenced Frequency Stabilized Radiator for High Range Resolution Imaging,” in *2023 IEEE Custom Integrated Circuits Conference (CICC)*, 2023, pp. 1–2.

[57] M. Tavakoli Taba, S. M. H. Naghavi, M. Fayazi, A. Cathelin, and E. Afshari, "A 360 GHz Wideband CMOS Autodyne FMCW Radar: Theory and Implementation," *IEEE Transactions on Microwave Theory and Techniques*, pp. 1–0, 2025.

[58] B. Hadidian, F. Khoeini, S. M. H. Naghavi, A. Cathelin, and E. Afshari, "A 220-GHz Energy-Efficient High-Data-Rate Wireless ASK Transmitter Array," *IEEE Journal of Solid-State Circuits*, vol. 57, no. 6, pp. 1623–1634, 2022.

[59] B. Hadidian, F. Khoeini, S. Hossein Naghavi, A. Cathelin, and E. Afshari, "An Energy Efficient Fully Integrated 20Gbps OOK Wireless Transmitter at 220GHz," in *2021 IEEE Custom Integrated Circuits Conference (CICC)*, 2021, pp. 1–2.

[60] M. Tavakoli Taba, S. M. Hossein Naghavi, and E. Afshari, "A Review on the State-of-the-Art THz FMCW Radars Implemented on Silicon: Invited," in *ESSCIRC 2022- IEEE 48th European Solid State Circuits Conference (ESSCIRC)*, 2022, pp. 533–537.

[61] M. TavakoliTaba, S. H. Naghavi, M. Aseeri, and E. Afshari, "A 100 GHz Fully Integrated FMCW Imaging Radar in 110 nm CMOS with Fundamental Oscillation Above fmax/2 for Drywall Inspection," in *2022 IEEE/MTT-S International Microwave Symposium - IMS 2022*, 2022, pp. 549–552.

[62] S. M. Hossein Naghavi, M. T. Taba, A. Tabatabavakili, A. Mostajeran, M. Aseeri, A. Cathelin, and E. Afshari, "24.4 Sub-THz Ruler: Spectral Bistability in a 235GHz Self-Injection-Locked Oscillator for Agile and Unambiguous Ranging," in *2024 IEEE International Solid-State Circuits Conference (ISSCC)*, vol. 67, 2024, pp. 418–420.

[63] S. M. H. Naghavi, M. T. Taba, M. Aseeri, and E. Afshari, "An Integrated 100-GHz FMCW Imaging Radar for Low-Cost Drywall Inspection," *IEEE Transactions on Microwave Theory and Techniques*, vol. 72, no. 2, pp. 1070–1084, 2024.

[64] A. Tabatabavakili, J. Gruber, and E. Afshari, "A Review on Sub-THz FMCW Radars," in *2023 Asia-Pacific Microwave Conference (APMC)*, 2023, pp. 787–789.

[65] A. Sadeghi, S. M. H. Naghavi, M. Mozafari, and E. Afshari, "Nanoscale biomaterials for terahertz imaging: A non-invasive approach for early cancer detection," *Translational Oncology*, vol. 27, p. 101565, 2023.

[66] T. S. Rappaport, Y. Xing, O. Kanhere, S. Ju, A. Madanayake, S. Mandal, A. Alkhateeb, and G. C. Trichopoulos, "Wireless communications and applications above 100 GHz: Opportunities and challenges for 6G and beyond," *IEEE access*, vol. 7, pp. 78 729–78 757, 2019.

[67] P. Heydari, H. Wang, H. Mohammadnezhad, and P. Nazari, "Energy efficient 100+ GHz transceivers enabling beyond-5G wireless communications," *IEEE Wireless Communications*, vol. 28, no. 1, pp. 144–151, 2021.

[68] S. Dang, O. Amin, B. Shihada, and M.-S. Alouini, "What should 6G be?" *Nature Electronics*, vol. 3, no. 1, pp. 20–29, 2020.

[69] M. H. Alsharif, M. A. Albreem, A. A. A. Solyman, and S. Kim, "Toward 6G communication networks: Terahertz frequency challenges and open research issues," *Computers, Materials & Continua*, 2021.

[70] W. Jiang, Q. Zhou, J. He, M. A. Habibi, S. Melnyk, M. El-Absi, B. Han, M. Di Renzo, H. D. Schotten, F.-L. Luo *et al.*, "Terahertz communications and sensing for 6G and beyond: A comprehensive review," *IEEE Communications Surveys & Tutorials*, 2024.

[71] M. A. Jamshed, A. Nauman, M. A. B. Abbasi, and S. W. Kim, "Antenna selection and designing for THz applications: suitability and performance evaluation: a survey," *IEEE Access*, vol. 8, pp. 113 246–113 261, 2020.

[72] A. Y. Pawar, D. D. Sonawane, K. B. Erande, and D. V. Derle, "Terahertz technology and its applications," *Drug invention today*, vol. 5, no. 2, pp. 157–163, 2013.

[73] Y. Roggo, N. Jent, A. Edmond, P. Chalus, and M. Ulmschneider, "Characterizing process effects on pharmaceutical solid forms using near-infrared spectroscopy and infrared imaging," *European Journal of Pharmaceutics and Biopharmaceutics*, vol. 61, no. 1-2, pp. 100–110, 2005.

[74] R. M. Woodward, V. P. Wallace, R. J. Pye, B. E. Cole, D. D. Arnone, E. H. Linfield, and M. Pepper, "Terahertz pulse imaging of ex vivo basal cell carcinoma," *Journal of Investigative Dermatology*, vol. 120, no. 1, pp. 72–78, 2003.

[75] M. Gezimati and G. Singh, "Advances in terahertz technology for cancer detection applications," *Optical and Quantum Electronics*, vol. 55, no. 2, p. 151, 2023.

[76] S. Nourinovin, M. M. Rahman, M. P. Philpott, Q. H. Abbasi, and A. Alomainy, "Terahertz characterization of ordinary and aggressive types of oral squamous cell carcinoma as a function of cancer stage and treatment efficiency," *IEEE Transactions on Instrumentation and Measurement*, vol. 72, pp. 1–9, 2023.

[77] A. D. Bounds and J. M. Girkin, "Early stage dental caries detection using near infrared spatial frequency domain imaging," *Scientific Reports*, vol. 11, no. 1, p. 2433, 2021.

[78] M. C. Kemp, P. Taday, B. E. Cole, J. Cluff, A. J. Fitzgerald, and W. R. Tribe, "Security applications of terahertz technology," in *Terahertz for military and security applications*, vol. 5070. SPIE, 2003, pp. 44–52.

[79] R. Li, C. Li, H. Li, S. Wu, and G. Fang, "Study of automatic detection of concealed targets in passive terahertz images for intelligent security screening," *IEEE Transactions on Terahertz Science and Technology*, vol. 9, no. 2, pp. 165–176, 2018.

[80] W. K. Alsaedi, H. Ahmadi, Z. Khan, and D. Grace, "Spectrum options and allocations for 6G: A regulatory and standardization review," *IEEE Open Journal of the Communications Society*, vol. 4, pp. 1787–1812, 2023.

[81] A. V. Muppala and K. Sarabandi, "Low-Cost 3-D Millimeter-Wave Concealed Weapons Detection Using Single Transceiver Affine Synthetic Arrays," *IEEE Transactions on Microwave Theory and Techniques*, vol. 71, no. 12, pp. 5445–5456, 2023.

[82] A. V. Muppala, A. Alburadi, A. Y. Nashashibi, H. N. Shaman, and K. Sarabandi, "A 223-GHz FMCW Imaging Radar With 360° FoV and 0.3° Azimuthal Resolution Enabled by a Rotationally Stable Fan-Beam Reflector," *IEEE Transactions on Geoscience and Remote Sensing*, vol. 61, pp. 1–9, 2023.

[83] A. V. Muppala, M. T. Taba, B. Yektakhah, J. Gruber, H. Alotaibi, K. Sarabandi, and E. Afshari, "A 242-267 GHz Bistatic Superheterodyne Radar System for Precision Terahertz Sensing and Imaging in 65-nm CMOS," *IEEE Transactions on Microwave Theory and Techniques*, pp. 1–13, 2025.

[84] A. V. Muppala and K. Sarabandi, "A Near-Field 3-D Imaging Radar Using a Sparse Spotlight MIMO Array for Weapons Detection," in *2023 IEEE International Symposium on Antennas and Propagation and USNC-URSI Radio Science Meeting (USNC-URSI)*, 2023, pp. 739–740.

[85] A. V. Muppala, A. Alburadi, and K. Sarabandi, "A J-band Fan-Beam 3-D Printed Reflector Antenna with Optimal Moment of Inertia for High Speed Scanning," in *2023 IEEE International Symposium on Antennas and Propagation and USNC-URSI Radio Science Meeting (USNC-URSI)*, 2023, pp. 955–956.

[86] A. J. Arockiam, K. Subramanian, R. Padmanabhan, R. Selvaraj, D. K. Bagal, and S. Rajesh, "A review on PLA with different fillers used as a filament in 3D printing," *Materials Today: Proceedings*, vol. 50, pp. 2057–2064, 2022.

[87] J. Griffey, "Types of Filaments for FDM printing," *Library Technology Reports*, vol. 53, no. 15, pp. 12–16, 2017.

[88] M. A. Rahman, M. Z. Islam, L. Gibbon, C. A. Ulven, and J. J. La Scala, "3D printing of continuous carbon fiber reinforced thermoset composites using UV curable resin," *Polymer Composites*, vol. 42, no. 11, pp. 5859–5868, 2021.

[89] F. Costa, M. Borgese, M. Degiorgi, and A. Monorchio, "Electromagnetic characterisation of materials by using transmission/reflection (T/R) devices," *Electronics*, vol. 6, no. 4, p. 95, 2017.

[90] L.-F. Chen, C. K. Ong, C. Neo, V. V. Varadan, and V. K. Varadan, *Microwave electronics: measurement and materials characterization*. John Wiley & Sons, 2004.

[91] A. Nicolson and G. Ross, "Measurement of the intrinsic properties of materials by time-domain techniques," *IEEE Transactions on instrumentation and measurement*, vol. 19, no. 4, pp. 377–382, 1970.

[92] W. B. Weir, "Automatic measurement of complex dielectric constant and permeability at microwave frequencies," *Proceedings of the IEEE*, vol. 62, no. 1, pp. 33–36, 1974.

[93] J. Baker-Jarvis, E. J. Vanzura, and W. A. Kissick, "Improved technique for determining complex permittivity with the transmission/reflection method," *IEEE Transactions on microwave theory and techniques*, vol. 38, no. 8, pp. 1096–1103, 1990.

[94] J. Baker-Jarvis, R. G. Geyer, and P. D. Domich, "A nonlinear least-squares solution with causality constraints applied to transmission line permittivity and permeability determination," *IEEE Transactions on Instrumentation and Measurement*, vol. 41, no. 5, pp. 646–652, 1992.

[95] O. Luukkonen, S. I. Maslovski, and S. A. Tretyakov, "A stepwise Nicolson–Ross–Weir-based material parameter extraction method," *IEEE antennas and wireless propagation letters*, vol. 10, pp. 1295–1298, 2011.

[96] X.-C. Wang, A. Díaz-Rubio, and S. A. Tretyakov, "An accurate method for measuring the sheet impedance of thin conductive films at microwave and millimeter-wave frequencies," *IEEE Transactions on Microwave Theory and Techniques*, vol. 65, no. 12, pp. 5009–5018, 2017.

[97] P. H. Bolivar, M. Brucherseifer, J. G. Rivas, R. Gonzalo, I. Ederra, A. L. Reynolds, M. Holker, and P. De Maagt, "Measurement of the dielectric constant and loss tangent of high dielectric-constant materials at terahertz frequencies," *IEEE Transactions on Microwave Theory and Techniques*, vol. 51, no. 4, pp. 1062–1066, 2003.

[98] Y. Liu, H. Naghavi, Y. Kuga, and J. M. Mower, "Loaded waveguide antenna for undersea communications," in *2024 IEEE International Symposium on Antennas and Propagation and INC/USNC-URSI Radio Science Meeting (AP-S/INC-USNC-URSI)*, 2024, pp. 463–464.

[99] Y. Liu, Y. Kuga, H. Naghavi, and J. M. Mower, "RF Systems for Through-Ice Communication in Polar Regions," in *2025 IEEE International Symposium on Antennas and Propagation and URSI Radio Science Meeting (AP-S/URSI)*, Jul. 2025, accepted for presentation.

[100] Y. Liu, J. Mower, K. Yan, C. Peng, A. Manu, Y. Kuga, and H. Naghavi, "Antenna Systems for Reliable Docking of Autonomous Underwater Vehicles," *IEEE Transactions on Antennas and Propagation*, 2025, submitted for publication.

[101] Y. Liu and H. Naghavi, "Terahertz Frequency-Modulated Continuous-Wave Dispersive Fourier-Transform Spectroscopy," *IEEE Transactions on Microwave Theory and Techniques*, 2025, under preparation; to be submitted 2025.

[102] S. Hallegatte, J. Rogelj, M. Allen, L. Clarke, O. Edenhofer, C. B. Field, P. Friedlingstein, L. Van Kesteren, R. Knutti, K. J. Mach *et al.*, "Mapping the climate change challenge," *Nature Climate Change*, vol. 6, no. 7, pp. 663–668, 2016.

[103] J. A. Patz, H. Frumkin, T. Holloway, D. J. Vimont, and A. Haines, "Climate change: challenges and opportunities for global health," *Jama*, vol. 312, no. 15, pp. 1565–1580, 2014.

[104] J. Wang and W. Azam, "Natural resource scarcity, fossil fuel energy consumption, and total greenhouse gas emissions in top emitting countries," *Geoscience frontiers*, vol. 15, no. 2, p. 101757, 2024.

[105] B. J. Cardinale, J. E. Duffy, A. Gonzalez, D. U. Hooper, C. Perrings, P. Venail, A. Narwani, G. M. Mace, D. Tilman, D. A. Wardle *et al.*, "Biodiversity loss and its impact on humanity," *Nature*, vol. 486, no. 7401, pp. 59–67, 2012.

[106] B. Cardinale, "Impacts of biodiversity loss," *Science*, vol. 336, no. 6081, pp. 552–553, 2012.

[107] M. Lin and C. Yang, "Ocean observation technologies: A review," *Chinese Journal of Mechanical Engineering*, vol. 33, pp. 1–18, 2020.

[108] R. E. Davis, "Drifter observations of coastal surface currents during CODE: The method and descriptive view," *Journal of Geophysical Research: Oceans*, vol. 90, no. C3, pp. 4741–4755, 1985.

[109] M. Bibuli, M. Caccia, L. Lapierre, and G. Bruzzone, "Guidance of unmanned surface vehicles: Experiments in vehicle following," *IEEE Robotics & Automation Magazine*, vol. 19, no. 3, pp. 92–102, 2012.

[110] R.-j. Yan, S. Pang, H.-b. Sun, and Y.-j. Pang, "Development and missions of unmanned surface vehicle," *Journal of Marine Science and Application*, vol. 9, pp. 451–457, 2010.

[111] J. Jin, J. Zhang, F. Shao, Z. Lyu, and D. Wang, "A novel ocean bathymetry technology based on an unmanned surface vehicle," *Acta Oceanologica Sinica*, vol. 37, pp. 99–106, 2018.

[112] S. C. Riser, H. J. Freeland, D. Roemmich, S. Wijffels, A. Troisi, M. Belbéoch, D. Gilbert, J. Xu, S. Pouliquen, A. Thresher *et al.*, "Fifteen years of ocean observations with the global Argo array," *Nature Climate Change*, vol. 6, no. 2, pp. 145–153, 2016.

[113] E. B. Clark, A. Branch, S. Chien, F. Mirza, J. D. Farrara, Y. Chao, D. Fratantoni, D. Aragon, O. Schofield, M. M. Flexas *et al.*, "Station-keeping underwater gliders using a predictive ocean circulation model and applications to SWOT calibration and validation," *IEEE Journal of Oceanic Engineering*, vol. 45, no. 2, pp. 371–384, 2019.

[114] P. Zhou, C. Yang, S. Wu, and Y. Zhu, “Designated area persistent monitoring strategies for hybrid underwater profilers,” *IEEE Journal of Oceanic Engineering*, vol. 45, no. 4, pp. 1322–1336, 2019.

[115] C. Kunz, C. Murphy, R. Camilli, H. Singh, J. Bailey, R. Eustice, M. Jakuba, K.-i. Nakamura, C. Roman, T. Sato *et al.*, “Deep sea underwater robotic exploration in the ice-covered arctic ocean with AUVs,” in *2008 IEEE/RSJ International Conference on Intelligent Robots and Systems*. IEEE, 2008, pp. 3654–3660.

[116] A.-R. Diercks, M. Woolsey, R. Jarnagin, V. Asper, C. Dike, M. D’Emidio, S. Tidwell, and A. Conti, “Site reconnaissance surveys for oil spill research using deep-sea AUVs,” in *2013 OCEANS-San Diego*. IEEE, 2013, pp. 1–5.

[117] P. Xia, F. Xu, Z. Song, S. Li, and J. Du, “Sensory augmentation for subsea robot teleoperation,” *Computers in Industry*, vol. 145, p. 103836, 2023.

[118] N. Palomeras, P. Ridao, D. Ribas, and G. Vallicrosa, “Autonomous I-AUV docking for fixed-base manipulation,” *IFAC Proceedings Volumes*, vol. 47, no. 3, pp. 12 160–12 165, 2014.

[119] D. B. Kilfoyle and A. B. Baggeroer, “The state of the art in underwater acoustic telemetry,” *IEEE Journal of oceanic engineering*, vol. 25, no. 1, pp. 4–27, 2000.

[120] M. Stojanovic and P.-P. J. Beaujean, “Acoustic communication,” *Springer Handbook of Ocean Engineering*, pp. 359–386, 2016.

[121] J. A. Simpson, B. L. Hughes, and J. F. Muth, “Smart transmitters and receivers for underwater free-space optical communication,” *IEEE Journal on selected areas in communications*, vol. 30, no. 5, pp. 964–974, 2012.

[122] H. Zhao, M. Xu, M. Shu, J. An, W. Ding, X. Liu, S. Wang, C. Zhao, H. Yu, H. Wang *et al.*, “Underwater wireless communication via TENG-generated Maxwell’s displacement current,” *Nature Communications*, vol. 13, no. 1, p. 3325, 2022.

[123] X. Sun, B. Deng, J. Zhang, M. Kelly, R. Alam, and S. Makiharju, “Reimagining autonomous underwater vehicle charging stations with wave energy,” *Berkeley Scientific Journal*, vol. 25, no. 2, 2021.

[124] R. Lin, D. Li, T. Zhang, and M. Lin, “A non-contact docking system for charging and recovering autonomous underwater vehicle,” *Journal of Marine Science and Technology*, vol. 24, pp. 902–916, 2019.

[125] J. Liu, F. Yu, B. He, and C. G. Soares, “A review of underwater docking and charging technology for autonomous vehicles,” *Ocean Engineering*, vol. 297, p. 117154, 2024.

[126] B. Pierre-Jean, F. Philippe, T. Beatrice, A. Yves, A. Yassine, F. Gilles, D. Maëlle, and S. Pauline, "Contactless data transfer for autonomous underwater vehicle docking station," in *OCEANS 2021: San Diego–Porto*. IEEE, 2021, pp. 1–5.

[127] J. Trowbridge, R. Weller, D. Kelley, E. Dever, A. Plueddemann, J. A. Barth, and O. Kawka, "The ocean observatories initiative," *Frontiers in Marine Science*, vol. 6, p. 74, 2019.

[128] O. Aboderin, L. M. Pessoa, and H. Salgado, "Wideband dipole antennas with parasitic elements for underwater communications," in *Oceans 2017-Aberdeen*. IEEE, 2017, pp. 1–6.

[129] ——, "Analysis of loop antenna with ground plane for underwater communications," in *Oceans 2017-Aberdeen*. IEEE, 2017, pp. 1–6.

[130] A. N. Jaafar, H. Ja'afar, Y. Yamada, F. Sadeghikia, I. P. Ibrahim, and M. K. A. Mahmood, "Design of an axial mode helical antenna with buffer layer for underwater applications," *International Journal of Electrical and Computer Engineering (IJECE)*, vol. 13, no. 1, pp. 473–482, 2023.

[131] S. Ryecroft, A. Shaw, P. Fergus, P. Kot, K. Hashim, A. Moody, and L. Conway, "A first implementation of underwater communications in raw water using the 433 MHz frequency combined with a bowtie antenna," *Sensors*, vol. 19, no. 8, p. 1813, 2019.

[132] I. Pasya, H. Zali, M. Saat, M. Ali, and T. Kobayashi, "Buffer layer configuration for wideband microstrip patch antenna for underwater applications," in *2016 Loughborough Antennas & Propagation Conference (LAPC)*. IEEE, 2016, pp. 1–5.

[133] Z. Hao, G. Dawei, Z. Guoping, and T. A. Gulliver, "The impact of antenna design and frequency on underwater wireless communications," in *Proceedings of 2011 IEEE Pacific Rim Conference on Communications, Computers and Signal Processing*. IEEE, 2011, pp. 868–872.

[134] A. Underwood and C. Murphy, "Design of a micro-AUV for autonomy development and multi-vehicle systems," in *OCEANS 2017-Aberdeen*. IEEE, 2017, pp. 1–6.

[135] K. Alam, T. Ray, and S. G. Anavatti, "Design and construction of an autonomous underwater vehicle," *Neurocomputing*, vol. 142, pp. 16–29, 2014.

[136] C. A. Balanis, *Antenna theory: analysis and design*. John wiley & sons, 2015.

[137] F. T. Ulaby, R. K. Moore, and A. K. Fung, *Microwave remote sensing: Active and passive. volume 1-microwave remote sensing fundamentals and radiometry*. Artech House, 1981.

[138] M. Yasuhara and R. Danovaro, "Temperature impacts on deep-sea biodiversity," *Biological Reviews*, vol. 91, no. 2, pp. 275–287, 2016.

[139] Y. Huo, X. Dong, and S. Beatty, “Cellular communications in ocean waves for maritime Internet of Things,” *IEEE Internet of Things Journal*, vol. 7, no. 10, pp. 9965–9979, 2020.

[140] D. M. Pozar, *Microwave engineering: theory and techniques*. John wiley & sons, 2021.

[141] G. Gonzalez, *Microwave transistor amplifiers (2nd ed.): analysis and design*. USA: Prentice-Hall, Inc., 1996.

[142] D. K. Barnes and G. A. Tarling, “Polar oceans in a changing climate,” *Current Biology*, vol. 27, no. 11, pp. R454–R460, 2017.

[143] O. A. Anisimov, D. G. Vaughan, T. V. Callaghan, C. Furgal, H. Marchant, T. D. Prowse, H. Vilhjálmsson, and J. E. Walsh, “Polar regions (arctic and antarctic),” *Climate change*, vol. 15, pp. 653–685, 2007.

[144] R. B. Alley, P. U. Clark, P. Huybrechts, and I. Joughin, “Ice-sheet and sea-level changes,” *science*, vol. 310, no. 5747, pp. 456–460, 2005.

[145] J. E. Box, A. Hubbard, D. B. Bahr, W. T. Colgan, X. Fettweis, K. D. Mankoff, A. Wehrlé, B. Noël, M. R. Van Den Broeke, B. Wouters *et al.*, “Greenland ice sheet climate disequilibrium and committed sea-level rise,” *Nature Climate Change*, vol. 12, no. 9, pp. 808–813, 2022.

[146] A. Aschwanden, M. A. Fahnestock, M. Truffer, D. J. Brinkerhoff, R. Hock, C. Khroulev, R. Mottram, and S. A. Khan, “Contribution of the Greenland Ice Sheet to sea level over the next millennium,” *Science advances*, vol. 5, no. 6, p. eaav9396, 2019.

[147] E. Cavan, N. Mackay, S. Hill, A. Atkinson, A. Belcher, and A. Visser, “Antarctic krill sequester similar amounts of carbon to key coastal blue carbon habitats,” *Nature Communications*, vol. 15, no. 1, p. 7842, 2024.

[148] S. J. Vavrus, “The influence of Arctic amplification on mid-latitude weather and climate,” *Current Climate Change Reports*, vol. 4, pp. 238–249, 2018.

[149] G. Heinemann, “The polar regions: a natural laboratory for boundary layer meteorology-a review,” *Meteorologische Zeitschrift*, vol. 17, no. 5, p. 589, 2008.

[150] X. Li, H. Guo, G. Cheng, X. Song, Y. Ran, M. Feng, T. Che, X. Li, L. Wang, A. Duan *et al.*, “Polar regions are critical in achieving global sustainable development goals,” *Nature Communications*, vol. 16, no. 1, p. 3879, 2025.

[151] M. J. Doble, A. L. Forrest, P. Wadhams, and B. E. Laval, “Through-ice AUV deployment: Operational and technical experience from two seasons of Arctic fieldwork,” *Cold Regions Science and Technology*, vol. 56, no. 2-3, pp. 90–97, 2009.

[152] A. Kukulya, A. Plueddemann, T. Austin, R. Stokey, M. Purcell, B. Allen, R. Littlefield, L. Freitag, P. Koski, E. Gallimore *et al.*, "Under-ice operations with a REMUS-100 AUV in the Arctic," in *2010 IEEE/OES Autonomous Underwater Vehicles*. IEEE, 2010, pp. 1–8.

[153] W. Stone, B. Hogan, C. Flesher, S. Gulati, K. Richmond, A. Murarka, G. Kuhlman, M. Sridharan, V. Siegel, R. Price *et al.*, "Design and deployment of a four-degrees-of-freedom hovering autonomous underwater vehicle for sub-ice exploration and mapping," *Proceedings of the Institution of Mechanical Engineers, Part M: Journal of Engineering for the Maritime Environment*, vol. 224, no. 4, pp. 341–361, 2010.

[154] W. Stone, K. Richmond, C. Flesher, B. Hogan, and V. Siegel, "Sub-ice autonomous underwater vehicle architectures for ocean world exploration and life search," *Outer Solar System: Prospective Energy and Material Resources*, pp. 429–541, 2018.

[155] A. Spears, M. West, M. Meister, J. Buffo, C. Walker, T. R. Collins, A. Howard, and B. Schmidt, "Under ice in antarctica: The icefin unmanned underwater vehicle development and deployment," *IEEE Robotics & Automation Magazine*, vol. 23, no. 4, pp. 30–41, 2016.

[156] O. Pradhan, S. Sandeep, A. J. Gasiewski, and W. Stone, "Design of a forward looking synthetic aperture radar for an autonomous cryobot for subsurface exploration of Europa," in *2017 IEEE International Geoscience and Remote Sensing Symposium (IGARSS)*. IEEE, 2017, pp. 1012–1015.

[157] C. Smeets, W. Boot, A. Hubbard, R. Pettersson, F. Wilhelms, M. R. Van Den Broeke, and R. S. Van De Wal, "A wireless subglacial probe for deep ice applications," *Journal of glaciology*, vol. 58, no. 211, pp. 841–848, 2012.

[158] K. Martinez, R. Ong, and J. Hart, "Glacsweb: a sensor network for hostile environments," in *2004 First Annual IEEE Communications Society Conference on Sensor and Ad Hoc Communications and Networks, 2004. IEEE SECON 2004*. IEEE, 2004, pp. 81–87.

[159] M. R. Prior-Jones, E. A. Bagshaw, J. Lees, L. Clare, S. Burrow, M. A. Werder, N. B. Karlsson, D. Dahl-Jensen, T. R. Chudley, P. Christoffersen *et al.*, "Cryoegg: development and field trials of a wireless subglacial probe for deep, fast-moving ice," *Journal of Glaciology*, vol. 67, no. 264, pp. 627–640, 2021.

[160] J. Dowdeswell, J. Evans, R. Mugford, G. Griffiths, S. McPhail, N. Millard, P. Stevenson, M. Brandon, C. Banks, K. Heywood *et al.*, "Autonomous underwater vehicles (AUVs) and investigations of the ice–ocean interface in Antarctic and Arctic waters," *Journal of Glaciology*, vol. 54, no. 187, pp. 661–672, 2008.

[161] A. Plueddemann, A. Kukulya, R. Stokey, and L. Freitag, "Autonomous underwater vehicle operations beneath coastal sea ice," *IEEE/ASME transactions on mechatronics*, vol. 17, no. 1, pp. 54–64, 2011.

[162] Y. Lan, S. Men, X. Xu, and K. Lu, “Experimental study of dielectric constant influence on electrorheological effect,” *Journal of Physics D: Applied Physics*, vol. 33, no. 10, p. 1239, 2000.

[163] Y. Haba, J. P. Gabriel, E. Thoms, and R. Richert, “Silicone materials for electrical insulation: A dielectric study of oil versus gel,” *IEEE Transactions on Dielectrics and Electrical Insulation*, vol. 29, no. 2, pp. 501–505, 2022.

[164] F. T. Ulaby, “Microwave remote sensing,” *Active and passive*, pp. Chap–7, 1986.

[165] V. P. Shah, “Design considerations for engineering autonomous underwater vehicles,” Ph.D. dissertation, Massachusetts Institute of Technology, 2007.

[166] J. Crowell, “Design challenges of a next generation small AUV,” in *2013 OCEANS-San Diego*. IEEE, 2013, pp. 1–5.

[167] I. F. Akyildiz and J. M. Jornet, “Electromagnetic wireless nanosensor networks,” *Nano Communication Networks*, vol. 1, no. 1, pp. 3–19, 2010.

[168] B. Ning, Z. Tian, W. Mei, Z. Chen, C. Han, S. Li, J. Yuan, and R. Zhang, “Beamforming technologies for ultra-massive MIMO in terahertz communications,” *IEEE Open Journal of the Communications Society*, vol. 4, pp. 614–658, 2023.

[169] H.-J. Song and N. Lee, “Terahertz communications: Challenges in the next decade,” *IEEE Transactions on Terahertz Science and Technology*, vol. 12, no. 2, pp. 105–117, 2021.

[170] Y. Peng, C. Shi, X. Wu, Y. Zhu, and S. Zhuang, “Terahertz imaging and spectroscopy in cancer diagnostics: a technical review,” *BME frontiers*, vol. 2020, p. 2547609, 2020.

[171] T. C. Williams, M. A. Stuchly, and P. Saville, “Modified transmission-reflection method for measuring constitutive parameters of thin flexible high-loss materials,” *IEEE transactions on microwave theory and techniques*, vol. 51, no. 5, pp. 1560–1566, 2003.

[172] D. K. Ghodgaonkar, V. V. Varadan, and V. K. Varadan, “A free-space method for measurement of dielectric constants and loss tangents at microwave frequencies,” *IEEE Transactions on Instrumentation and measurement*, vol. 38, no. 3, pp. 789–793, 2002.

[173] I. Kuzmanić, I. Vujović, M. Petković, and J. Šoda, “Influence of 3D printing properties on relative dielectric constant in PLA and ABS materials,” *Progress in additive manufacturing*, vol. 8, no. 4, pp. 703–710, 2023.

[174] M. Akhtar, L. Feher, and M. Thumm, “Measurement of dielectric constant and loss tangent of epoxy resins using a waveguide approach,” in *2006 IEEE Antennas and Propagation Society International Symposium*. IEEE, 2006, pp. 3179–3182.